Search for Prompt Neutrinos with AMANDA-II

Dissertation zur Erlangung des Grades
„Doktor der Naturwissenschaften"
am Fachbereich Physik
der Johannes Gutenberg-Universität Mainz

Sara Rebecca Gozzini

geboren in Ceva CN, Italien

Mainz, 11. September 2008

Abstract

The investigation performed in this work aims to identify and disentangle the signal of prompt neutrinos from the inclusive atmospheric spectrum. We have analysed data recorded in the years 2000-2003 by the AMANDA-II detector at the geographical South Pole. After a tight event selection, our sample is composed of about $4 \cdot 10^3$ atmospheric neutrinos.

Prompt neutrinos are decay products of heavy quark hadrons, which are produced in the collision of a cosmic ray particle with a nucleon in the atmosphere. The technique used to recognise prompt neutrinos is based on a simulated information of their energy spectrum, which appears harder than that of the conventional component from light quarks. Models accounting for different hadron production and decay schemes have been included in a Monte Carlo simulation and convoluted with the detector response, in order to reproduce the different spectra.

The background of conventional events has been described with the Bartol 2006 tables. The energy spectrum of our data has been reconstructed through a numerical unfolding algorithm. The reconstruction is based on a Monte Carlo simulation and uses as an input three parameters of the neutrino track which are correlated with the energy of the event. Numerical regularisation is introduced to achieve a result free of unphysical oscillations, typical unfortunate feature of unfolding. The reconstructed data spectrum has been compared with different predictions using the model rejection factor technique. The prompt neutrino models differ in the choice of the hadron interaction model, the set of parton distribution functions and the numerical parameterisation of the fragmentation functions describing the transition from quark to hadrons.

Here we considered mainly three classes of models, known in the literature as the *Recombination Quark Parton Model*, the *Quark Gluon String Model* and the *Perturbative QCD model*. Upper limits have been set on the expected flux predictions, based on our observations. The quark gluon string model seems to be disfavoured at 90% confidence level. Theoretical uncertainties strongly affect the predictions, as the deep inelastic QCD scattering process contains quantities that cannot measured at high Q^2 and small x. Systematics affecting the measurements are partly ascribed to the ice structure and partly to the detector efficiency. For the former, we use a reference description of the optical properties of the South Pole glacier. As for the latter, the acceptance of the photomultipliers has been estimated in this work with a geometrical method based on the probability of detecting photon at a given distance.

Chances to improve upon the current limits are assigned to the future large neutrino telescopes, which will allow to increase the sensitivity to both prompt and extraterrestrial neutrinos.

this thesis is dedicated to the two girls who won't be here to read it
...thank you mum, thank you nan

Contents

Introduction

Neutrino astrophysics offers an endeavouring possibility of accessing information on extra-galactic objects through the observation of high energy particles. The flux of neutrinos of atmospheric origin creates an important background for neutrino telescopes, in that it limits their sensitivity to astrophysical signals. Energies above 1 TeV are critical; in this region prompt neutrinos originating from decays of heavy quark hadrons give a considerable rise to the atmospheric flux. This work focuses on the possibility of identifying the signal of prompt neutrinos using data recorded by the AMANDA-II detector. Besides the need to describe the high energy atmospheric background, the search for prompt neutrinos is motivated by the fact that an observation, or failure to observe them, might impose constraints on the charm production cross sections at high energy. Prompt neutrinos have not been yet observed. The chance to identify them lies with very large telescopes, which could compensate for their low expected flux, together with a refined analysis strategy to isolate the prompt signal from the atmospheric background.

The principles of neutrino detection are illustrated in chapter 1. In the same chapter, some general aspects of neutrino physics are summarised. The purpose of this introductory part is to outline, with reference to the literature, how neutrinos are elusive particles to detect, and consequently how critical a goal is to draw physical conclusions in the presence of such a weak signal.

The AMANDA-II detector, described in chapter 2 together with its data acquisition system, is a Cherenkov telescope operating at the geographical South Pole. The data used in this work are atmospheric neutrino events, reconstructed from their charged current interaction products, recorded in the years 2000-2003.

A Monte Carlo simulation is used to refine the selection techniques. In chapter 3 the AMANDA simulation chain is described. The production, propagation and detection of a neutrino is reproduced in different steps, and convoluted with a simulation of the detector response.

Chapter 4 illustrates the algorithms developed by the AMANDA Collaboration to identify neutrino-induced events in the ice, and reconstruct their tracks. The background is represented by a very large amount of leptons directly produced in cosmic ray showers; besides this, electronic artefacts can originate unphysical events. The rejection of these events is achieved through

dedicated filters, which are described in the same chapter.

The selection of events suitable for this analysis is described in chapter 5. Some track parameters are considered as indicators of good events with which to build the final sample of data. The rejection of background is based on a comparison with a simulated sample, and optimal filter conditions are established to ensure minimal signal suppression. After selection, about $4 \cdot 10^3$ atmospheric neutrino events compose our data sample. The reconstructed tracks are obtained with a likelihood based reconstruction algorithm and hence are of high quality.

In chapter 6 a brief description of a method to determine the detector acceptance is presented; the result achieved in this chapter is included in the systematic uncertainties affecting the result.

The identification of prompt neutrinos is based on the difference of their spectral shape from that of conventional particles, showing more events in the high energy region. A numerical unfolding algorithm has been applied to our data to reconstruct the neutrino energy spectrum, with input from variables correlated with the neutrino energy; a Monte Carlo simulation provides the basis for the procedure. The unfolding problem is illustrated in chapter 7, together with the details of the code.

In chapter 8, the results obtained with this work are presented. The atmospheric neutrino spectrum has been investigated with specific focus on those processes leading to the production of heavy quarks from a cosmic ray collision in the atmosphere. The question of whether or not we see a signal of prompt neutrinos strongly depends on the accuracy of the predicted flux, which is not absolutely known, but modelled on a certain number of assumptions. Several models for prompt hadron production have been taken into account in this work, included in simulated samples and convoluted with the AMANDA detector response. The different spectra obtained have been compared with the unfolded data spectrum using the model rejection factor technique. Systematic and theoretical uncertainties have been considered. Theoretical errors largely affect the description of heavy quark production from cosmic ray collisions. The deep inelastic QCD process needs input from non-perturbative physics for the determination of the parton distribution functions and fragmentation of quarks into hadrons. Fits on the data are used to extend our current information to the high energy region, where no data from colliders are available. Systematics mostly originate from our understanding of the ice properties, for which we quote the specific literature. Regarding the detector response, the acceptance of the AMANDA photomultipliers has been evaluated in chapter 6.

We conclude with a summary of the achieved results and a short outlook on the future, where possible improvements of the current analysis are presented. We point out with particular emphasis the importance of investigating cosmic ray neutrinos for the opportunity offered to access the high energy region.

Chapter 1

Neutrinos

"Wie der Überbringer dieser Zeilen, den ich huldvollst anzuhören bitte, Ihnen des näheren auseinandersetzen wird, bin ich angesichts der falschen Statistik der N- und Li 6-Kerne, sowie des kontinuierlichen ß-Spektrums auf einen verzweifelten Ausweg verfallen, um den Wechselsatz der Statistik und den Energiesatz zu retten. Nämlich die Möglichkeit, es könnten elektrisch neutrale Teilchen, die ich Neutronen nennen will, in den Kernen existieren, welche den Spin 1/2 haben und das Ausschließungsprinzip befolgen und sich von Lichtquanten außerdem noch dadurch unterscheiden, daß sie nicht mit Lichtgeschwindigkeit laufen. [...]" [1].

1.1 Theory and Discovery of Neutrinos

The history of neutrinos begins in Zurich, on December 4th 1930.

During the last century, it has often happened that contradictory observations have led theorists to invent a new particle which has kept the community busy in finding a way to detect it[1]. When Wolfgang Pauli, at the end of 1930, suggested the existence of the neutrino, he was probably sceptical himself about the possibility of proving its existence.

The idea is typewritten in an open letter sent to a physics meeting gathered at Tübingen, although Pauli did not dare publishing his hypothesis until the Solvay conference which took place in Brussels in 1933. It took another 23 years for the academic community to find proof of the existence of the particle proposed by Pauli.

The theorisation of a neutral fermion follows from the observation of the continuum beta decay spectrum, which is is characteristic for a three-body decay, but in contrast with the observation of just two products in the final state. The spectrum is consistent with the postulation of the emission of an additional undetected fermion. Basing himself on Pauli's idea, Enrico Fermi

[1]Examples are the Z^0 boson at LEP, the antiproton, the top quark and the yet undetected Higgs boson.

Figure 1.1: The 7th Solvay Conference, Brussels, 1933.

developed his theory of beta decay. He named "neutrino" the neutral fermion predicted by Pauli. The name "neutron" assigned in the original Tübingen letter had been given to the neutral particle observed in the nucleus in 1932, whose mass was too large to identify it with Pauli's conjecture.

It was immediately recognised that the neutrino would have been an elusive particle to detect, due to its extraordinarily weak coupling to matter. As Pauli claims in his letter,

"[I] trustfully turn first to you, dear radioactive people, with the question of how likely it is to find experimental evidence for such a neutron [...]"

The discovery was made in 1956 when Cowan and Reines detected anti-neutrinos emitted from a nuclear reactor at Savannah River in South Carolina, USA. Twenty-three years had passed since the Solvay conference. The claim for evidence awarded Reines the Nobel Prize in 1995.
The Savannah River Neutrino Detector consisted of two large, flat plastic tanks filled with water. Protons in water provided the target for the inverse beta decay. Those two tanks were deployed between three scintillator detectors, each equipped with 110 photomultiplier tubes to collect light and convert it to an electric signal; the setup is sketched in figure 1.2.

On June 14, 1956, a telegram was sent to CERN announcing "we are happy to inform you that we have definitely detected neutrinos from fission fragments by observing inverse beta decay of protons" [2]. History tells us that Pauli celebrated the discovery with a case of champagne.

In 1963, the experiment of Lederman, Schwartz and Steinberg proved that a second neutrino was associated with the muon in the way the known electron neutrino was associated with the electron [3]. The discovery was awarded the Nobel Prize in 1988 and provided the first hint of a second gen-

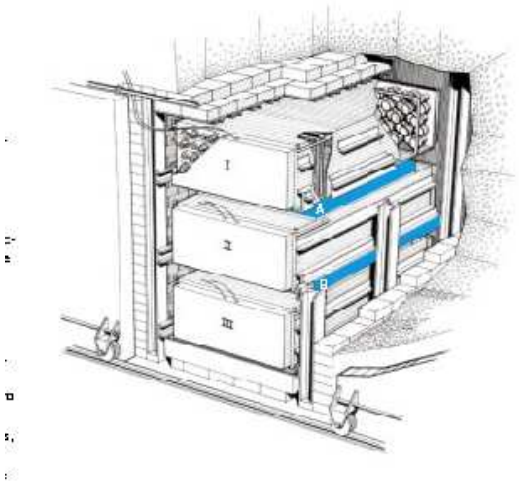

Figure 1.2: The Savannah River experimental setting. A neutrino-induced event in one of the two water tanks would create two pairs of proton pulses in the two neighbouring detectors, the first from positron annihilation and the second from neutron capture. No signal would be detected in the third scintillator detector which could not be reached by such a low energy event.

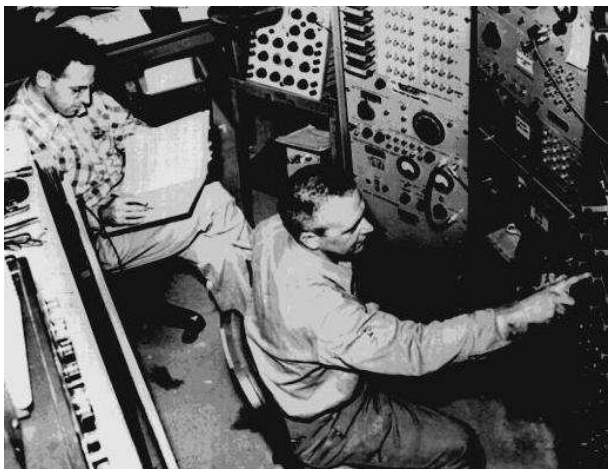

Figure 1.3: Reines and Cowan at the site of the Savannah River detector, where after 23 years from its theorisation, the first neutrino event was detected.

Figure 1.4: Left - Frederick Reines. Right - Leon Lederman.

eration of neutrinos.
Finally, in 1975, the third lepton flavour discovery awarded the Nobel Prize to Martin Perl (1995). To complete the puzzle, in the year 2000 the DONUT collaboration claimed the observation of the tau neutrino, up to now the last particle of the Standard Model of particle physics to be detected.

1.2 Neutrinos and the Standard Model

The Standard Model of particle physics is a gauge theory which summarises almost one century of elementary particle investigation. Currently, it is the best description of the nature of matter and interaction, built on the gauge group $SU(3) \otimes SU(2) \otimes U(1)$ with spontaneous symmetry breaking. On this structure the classification of particles in matter (fermions) and gauge (bosons) is based. Only gravity is at the current time not yet framed in a quantum field theory interpretation.

Neutrinos are fermions of spin $\frac{1}{2}$ and belong to three different generations of flavour, an experimental observation based on the fact that they appear to be related to the three elementary fermions e, μ and τ. The total number of neutrino families is confirmed by the results at LEP in 1989 [106]. Neutrinos take part only in weak processes. They are probably the most elusive elementary particles to detect and the most problematic to fit in the standard model framework.

Elementary particles are arranged in multiplets according to the representations[2] of the gauge group. To the group $SU(2)$ is associated an operator I whose square I^2 diagonalises simultaneously with its third component I_3, with the two quantum numbers of total isospin and third component as eigenvalues. Total isospin identifies a multiplet, and the values of its third component identify the position of the particle inside the multiplet[3]. One of

[2]Representation theory is a mathematical tool to describe particles and symmetries in a gauge theory.

[3]The description of neutrino interactions require the electroweak standard model $SU(2) \otimes$

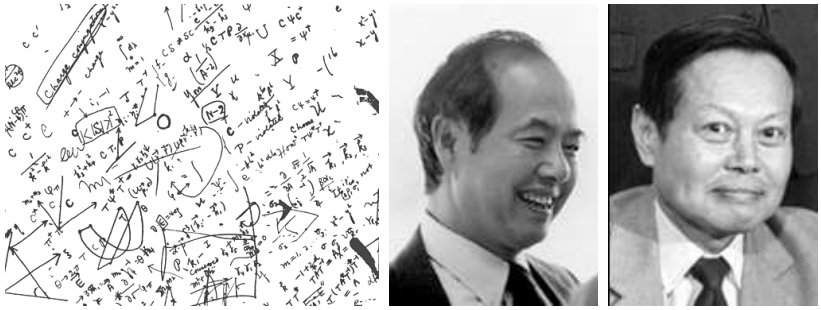

Figure 1.5: Left: the pad showing the idea of T.D.Lee and C.N.Yang, 1956. Right: T.D.Lee and C.N.Yang.

the eccentric properties of neutrino interactions is the violation of parity[4]. An interaction, or physical event, symmetric under parity is an event reproducing itself under the exchange of its spacial coordinates. In words it means that given a mirror, we are incapable of distinguishing the reality from its specular image. Until January 1957, it had been natural to think of it as a natural symmetry of physical interactions. The unexpected downfall of parity was first observed in β decays[7, 6]. Neutrinos maximally violate it, as they exist in a left-handed state only. It is an odd property: physics welcomes symmetric systems. As Lederman writes [4], "Parity was useful.[...] It also saves work. [...] by studying the half that you do see, you can pretty much know what is behind the screen". The two theorists of parity violation are T.D.Lee and C.N.Yang. In the Summer of 1956, in visit to Brookhaven, they attempted to interpret a puzzling result of the Cosmotron accelerator, question usually known as "$\theta - \tau$" puzzle. The matter was the observation of a particle which decays into two pions, named θ, very similar to the τ, observed in cosmic rays by Powell in 1949, which decays into three pions. All the quantum numbers, masses and lifetimes of those particles appeared to be identical. The two seem to be distinguishable only when looking at their decay channels. Pions have parity -1. If parity is conserved, a particle which decays to an odd number of pions cannot coincide with a particle whose decay results in an even number. Their theory of β decays and parity violation is proposed in their paper "Question of parity conservation in weak interactions" [5], and won them the Nobel Prize in 1957.

In Dirac's theory, a fermion is represented by a spinor ψ of 4 components, which can be decomposed into its two chirality eigenstates.

$$\psi = \psi_R \oplus \psi_L. \tag{1.1}$$

The observation of parity violation implies that the spinor of a neutrino field is

$U(1)$ only, that can be factorised as no mixing occurs between it and the $SU(3)$ component.

[4]Parity is the discrete symmetry mirror-reflecting the space coordinates $P(\vec{x}) = -\vec{x}$.

composed by its left-handed component only[5]. The γ^5 in the neutrino-lepton-W vertex projects the particles interacting with a neutrino on helicity eigenstates, restricting them to take part in the interaction with their left-handed component only. Interacting particles, i.e. those arranged in a doublet, are left-handed spinors only. The right-handed components transform as singlets; the action of the group leaves them unchanged. As a consequence, left- and right-handed particles are represented by different multiplets

$$\begin{pmatrix} \nu_e \\ e \end{pmatrix}_L, \begin{pmatrix} \nu_\mu \\ \mu \end{pmatrix}_L, \begin{pmatrix} \nu_\tau \\ \tau \end{pmatrix}_L \begin{pmatrix} e \end{pmatrix}_R \begin{pmatrix} \mu \end{pmatrix}_R \begin{pmatrix} \tau \end{pmatrix}_R \tag{1.2}$$

A $SU(2)$ vertex allows for the transition between upper and lower components of a doublet, conserving the lepton number for each flavour. This phenomenological rule suggested by observations is violated by the hypothesis of oscillations, that introduce flavour transitions. The Standard Model does not include any vertex in the Standard Model for this process.

1.3 What does not Match the Standard Model

It is accepted that the Standard Model, if not the ultimate theory of particle physics, is at least the most satisfactory one restricted to the the high energy range reached at present. However, if there are reasons to suspect the need to write a theory beyond the Standard Model, neutrinos are for sure responsible of many of them. Last detected particles, neutrinos showed a remarkable amount of sides that were not in accord with the predictions.

The first question arises about masses: neutrinos are massless according to the standard model, but recent observations, i.e. oscillation analyses [9], state the contrary. However, they only make a statement on the mass differences. The upper limit on the absolute neutrino mass has been obtained by tritium decay data [11][6]. If neutrinos have a mass, a right-handed component should be present. The first and minimal extension of the standard model including massive neutrinos predicts a right-handed component in a $SU(2)$ singlet, which does not originate any vertex. The mass term for neutrinos is introduced with a coupling of the type $m\,\overline{\nu}_L\nu_R$. No new processes originate from this extension, so that the non-observation of such a right-handed neutrinos is respected. A larger extension can be realised with the introduction of a right-handed neutrino in a $SU(2)$ doublet. This would be achieved with the addition of a heavy lepton to the model, which is however not observed.

Besides this, if mass eigenstates do not coincide with flavour eigenstates, the system can oscillate. Flavour number seems to be violated by oscillations,

[5]The left- and right-handed projectors are defined as $P_{R/L} = \frac{1\pm\gamma^5}{2}$ with action $P_{R/L}\psi = \psi_{R/L}$

[6]The Mainz neutrino experiment sets an upper limit of $m(\nu_e) \leq 2.3$ eV/c^2 at 95% confidence level

which are at the current moment the preferred theory to explain neutrino disappearance from the Sun and from reactors.

To go further, in the field of speculative physics, neutrinos might prove violation of Lorentz invariance [37], extra-dimensions [36], the discrete structure of the space-time, quantum decoherence and CPT violation under the Planck scale [37, 38, 39, 40]. At the present moment, all those effects have very uncertain possibilities to be proved; however, they would support with a further proof the need of writing an extension of the Standard Model.

1.4 Neutrino Detector and Telescopes

Currently, several neutrino experiments take data with the purpose of detecting atmospheric, solar and reactor neutrinos. The majority of such detectors work on the principle of Cherenkov effect, although lately new techniques as acoustic and radio have been developed. The setup of a neutrino telescope requires a considerable technical effort, because the the low reaction cross section of neutrino interactions requires a very large instrumented volume. Experiments as Super-Kamiokande [13], SNO [14], ANTARES [15], Bajkal [16], NEMO [17], NESTOR [18], AMANDA and IceCube are all based on a large volume of a scintillator medium (water or ice) instrumented with photomultipliers, of different design. Another series of detectors is associated with nuclear reactors with the aim of investigating the typical neutrino appearance and disappearance phenomena basing on a known production rate, like in the case of Double CHOOZ [19]. Neutrino beam experiments are similar, with a neutrino factory represented by either a reactor or an accelerator ring, and a far detection location placed at an interesting distance for the purpose of detecting oscillations, like MINOS [20], associated with the Tevatron, OPERA [21], associated with the CERN, and T2K [22]. Also observatories designed for cosmic ray detection, as AUGER [25], recently elaborated techniques to detect and identify neutrino events. Another class of detectors is designed for neutrino detection from double beta decay, as GERDA [29], COBRA [30] and the setup of the Heidelberg-Moscow Collaboration [31]. Finally, other detection methods than Cherenkov light are used in the radio experiments RICE [27] and AURA [26] and in the acoustic set-up SPATS [28] at South Pole.

1.5 Mixing and Oscillations

Oscillations are a typical quantum mechanics phenomenon appearing when describing a system whose states are not eigenstates of the Hamiltonian. Neutrinos oscillate because the Hamiltonian eigenstates evolve according to different eigenvalues represented by the masses of the neutrino states. When after a certain time t the initial state is re-composed from its components, it turns out to be rotated in the flavour space (figure 1.6 illustrates the situation). In

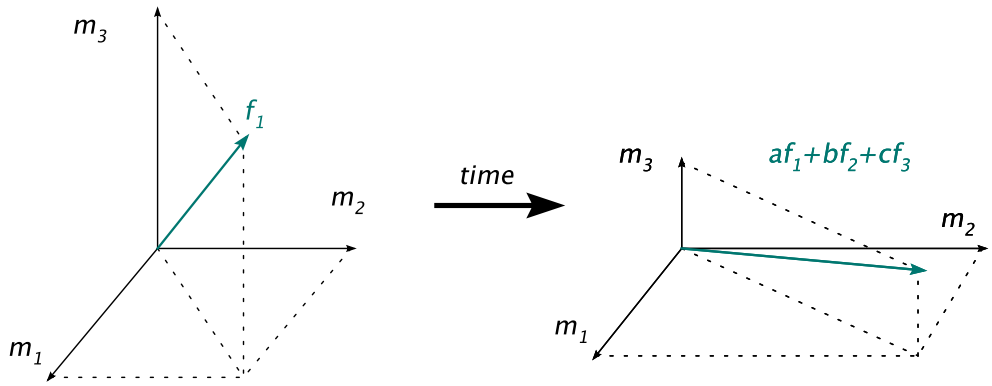

Figure 1.6: Time evolution in quantum mechanics. The states of defined mass (energy) are eigenstates of the Hamiltonian: hence they are contracted or dilated by their eigenvalues and maintain their direction. A state of defined flavour, after time t, is rotated in the flavour space.

quantum mechanics, a measurement determines the choice of a basis of physical states, formed by the eigenstates of the measured operator. Different bases associated to different operators can be connected by a linear transformation. Any state, if expanded on a basis, can be seen as a mixing of the various eigenstates. A particle produced in a certain flavour state originates from a weak interaction process described by an Hamiltonian H_f. On the nature of flavour states, a remark should be done to clarify their definition. The canonical brackets for the operators a, a^+ are not conserved between the mass and flavour basis, due to the mass term [8]. Neutrino weak eigenstates can only be defined in the approximation

$$\frac{m_i}{2E_i} \to 0, \tag{1.3}$$

in which case it is possible to correctly define a Fock space of states. Additionally, the description of neutrinos as plane waves is based on the ideal assumption of free particles propagating without interruptions, with no sources and no ending points. In reality, neutrinos do have sources. They are produced and detected in processes involving reactions with other particles; hence they are better described by the wave packets formalism [35]. The typical size of a wave packet determines the coherence length, or overlapping length of the two packets. Wave packet effects are weak when neutrinos are highly relativistic. If this approximation is not valid, when the separation between wave packets is large, neutrinos do not interfere and no oscillations occur.

An initial state of a neutrino of flavour l is written in the Schroedinger representation as $|\psi(0)\rangle = |\nu_l\rangle$. This state obeys the equation

$$i\frac{\partial|\psi(t)\rangle}{\partial t} = H|\psi(t)\rangle \tag{1.4}$$

As time evolves, particles propagate as described by an Hamiltonian H_m. A flavour state at time 0 can be expanded on the mass basis in

$$|\nu_\alpha(0)\rangle = \sum_j U_{\alpha j}|\nu_j(0)\rangle \tag{1.5}$$

in the Schroedinger representation, as time evolution is given for defined mass (four-momentum) states[7]:

$$|\psi(t)\rangle = e^{-iH_0 t}|\psi(0)\rangle. \tag{1.6}$$

In the vacuum, hence in absence of potential, the eigenvalues of H are

$$E_i = p + \frac{m_i^2}{2p} \qquad \text{given by} \qquad H|i\rangle = E_i|i\rangle. \tag{1.7}$$

The initial state of neutrino of flavour l recomposed after a time t on the initial basis is

$$|\nu_l(t)\rangle = \sum_{i=1}^{3} |\nu_i\rangle e^{-iE_i t} U_{li}^*. \tag{1.8}$$

According to the rules of quantum mechanics, if at $t = 0$ a neutrino of flavour l is produced, at $t > 0$ the state turns into a superposition of stationary states, with phases due to the different masses of the mass states. Finally the neutrino is detected via a charged current or neutral current process $\nu_l + N \to l + X$.. The matrix element leading to the cross section for this event is

$$\langle l' X|S|\nu_{l'} N\rangle = -i\frac{G_f}{\sqrt{2}} N 2\bar{u}_L(p')\gamma_\alpha u_L(p)\langle X|J^\alpha(0)|N\rangle(2\pi)^4\delta(P' - P). \tag{1.9}$$

The time evolution equation, with $E_i = p + \frac{m_i^2}{2p}$, yields the standard oscillation formula[8]

$$P(\nu_l \to \nu_{l'}) = \langle \nu_{l'}(t)|\nu_l(t)\rangle = \left|\delta_{l'l} + \sum_i U_{l'i}\, e^{\frac{\delta m^2}{2E} L - 1}\, U_{li}^*\right|^2, \tag{1.10}$$

where L is the distance travelled by neutrinos between production and detection, for the relativistic case $L \simeq t$.

All those theoretical issues turned out to be interesting when, in 1964, John Bahcall and Raymod Davis Jr. uncovered the so-called problem of the missing neutrinos from the Sun. They were investigating the conversion of protons to

[7]Note, the unitarity of time evolution, or equivalently the hermicity of H, does not hold for unstable particles.

[8]The unitarity of the U matrix ensures the normalisation of probabilities.

$$U^\dagger U = 1 \Rightarrow \sum_l P(\nu_l \to \nu_{l'}) = 1.$$

Figure 1.7: Raymond David Jr. (left) and John Bahcall about a mile underground in the Homestake Gold Mine in Lead, South Dakota, USA.

Helium, proposed at the beginning of the century as the source of sunlight, happening in the Sun through the reaction

$$4\mathrm{p} \rightarrow^{4} \mathrm{He} + 2\mathrm{e}^{+} + 2\nu_e. \tag{1.11}$$

The first results were announced in 1968. They detected only about one third as many radioactive argon atoms as were predicted to be produced by solar neutrinos, discrepancy which could not be ascribed at the solar model. This observation suggested that the idea proposed by Pontecorvo [12] of neutrinos oscillating between flavour eigenstates might be the correct way to describe the results. This was the year 1969, and the possibility of detecting the neutrino oscillations effect was still far to come.

A first proposal to investigate neutrino oscillations was made in 1989 by the Kamiokande collaboration. Their setup consisted of a large underground water detector with which to detect the rate at which electrons in the water scattered the highest-energy neutrinos emitted from the Sun. Despite the Kamiokande detector confirming that the number of neutrino events that were observed were less than that predicted by the theoretical model of the Sun, the discrepancy in the water detector was less stringent than Davis's limit. A larger version of the detector followed, named Super-Kamiokande and whose purpose was to improve upon the Kamiokande results. On June 5 1998 the Super-Kamiokande collaboration announced the discovery of evidence for neutrino mass during the Neutrino '98 conference, and their result was published in the paper, "Measurement of the flux and zenith angle distribution of upward going muons by Super-Kamiokande" [9].
In June 2001 another milestone in the missing neutrino mystery was posed by the Canadian detector SNO in the Sudbury mine, Ontario. The SNO collaboration looked at high energy solar electron neutrinos using heavy water D_2O Cherenkov detection. They observed approximately one third of the predicted electron neutrinos expected from the Solar standard model predictions. This

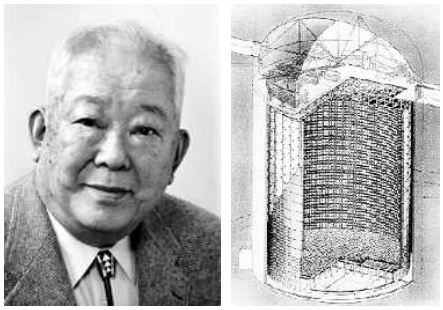

Figure 1.8: Left: Masatoshi Koshiba, leader of the pioneering Kamiokande collaboration. Right: A view of the Kamiokande detector.

result is independently proved by the Kamland collaboration, which report a deficit in the detected number of anti-neutrinos emitted by nuclear power reactors [10].

1.6 Neutrinos in Cosmology and Astrophysics

Cosmology is the branch of physics investigating the history of the first seconds of the universe. Neutrinos are often indicated as the ideal cosmic messenger in space and time as they can travel large distances through extra-galactic electric and magnetic fields without bending, and minimally interacting with matter. However, no extra-galactic neutrinos have ever been detected on Earth, and only one case of extra-terrestrial neutrinos has been observed from the supernova 1987A [23], if we exclude solar neutrinos. The nature of objects as supernovae, gamma ray bursts and active galactic nuclei could be investigated through neutrinos emitted from those sources. The identification of a neutrino abundance from a certain direction in the sky would indicate the possible presence of a source, either optically visible, in which case listed in a catalogue, or new. Similar observation are currently giving the first results with gamma rays [24] and cosmic radiation [81], opening a new window of possibilities for astronomy through particle physics. The search for cosmic neutrinos is additionally interesting as they could be messengers announcing the explosion of a supernova [47]. A prompt identification of neutrino abundance at low energy might allow for the real-time detection of a supernova explosion, a very promising tool to understand the dynamic of such rare process in our galaxy. Theories predicting the existence of micro black holes [36] see in neutrinos a possible source of information; the predicted effect should realise through loss of quantum numbers over long paths and hence decoherence effects in oscillations. An open question is the cosmic neutrino background [32], an up to now undetected sign of relic neutrinos released soon after the big bang.

1.7 Dark Matter?

Dark matter is supposed to be non-luminous and non-absorbing matter whose evidence is inferred from gravitational effects on cosmic objects such as stars, gas clouds and galaxies. This theorised, yet undetected matter does not interact in any of the known ways (strong, weak or electromagnetic) with visible matter. Despite this, evidence for dark matter is suggested by many effects, as the observation of galactic rotation curves and gravitational lensing [33]. With the current assumptions on neutrino mass limits, the contribution of neutrinos to dark matter density has strong constraints [34]. It has been argued that the most dark matter should be "cold", i.e. non-relativistic. In great unification theories new particles are predicted as possible dark matter candidates and decay channels of such particles into standard model particles have been investigated. This has suggested the neutrino search from neutralino annihilation; the AMANDA Collaboration has been investigating this topic [49, 50].

1.8 Neutrinos and the Nature of Space Time

Recently developed theories, as loop quantum gravity, suggest that the space-time might not have a continuous structure, but rather be in a form of a lattice or foam[9]. One of the many aspects predicted by such theories is the violation of Lorentz invariance. It is well accepted that every transformation belonging to the Lorentz group is a symmetry of a physical system or equation. Invariance is broken by the introduction of a fundamental scale (the length of the lattice) or preferred reference frame (the one respect to which the lattice is at rest). This conflicts with the general equivalence principle stating the independence of physics from the choice of coordinates, in a general inertial or not inertial reference frame. Mathematically, Lorentz invariance violation can be realised as a perturbation by adding to the Lagrangian of a physical system one violating term, whose value can be conveniently chosen to guarantee that the invariance is preserved at energies far under the Planck scale. Extremely relativistic particles as neutrinos ($m/E \to 0$) could prove Lorentz invariance effects in alternative oscillation models [41]. Related to this topic is the idea of CPT violation due to quantum decoherence effects [37]. This is realised through the loss of quantum numbers in objects as topological defects or micro black holes whose typical dimension is smaller than the minimum resolvable length, defined as the lattice scale. With the current limits reached at colliders, all experiments aiming to investigate physics beyond the Planck scale must turn to astronomical environments, where the largest distances and higher energies are available.

[9] A foam is a random, not regular lattice

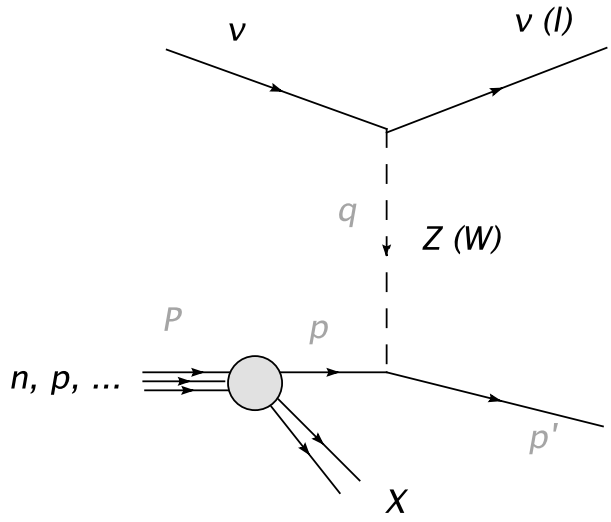

Figure 1.9: Neutral current (charged current in brackets) deep inelastic scattering process for neutrino-nucleon scattering.

1.9 High Energy Neutrino-Nucleon Interactions

We focus in this section on the neutrino scattering process which is related to neutrino detection in AMANDA, as further explained in the next chapter, section 2.1. The charged current scattering of a neutrino on a nucleon in ice is described as a neutrino-parton process with two kinematic variables [10] x and Q^2. All Cherenkov telescopes work on the principle that charged leptons emitted from a neutrino interaction can be identified and used for indirect observation of the neutrino itself. The cross section for the inclusive process $\nu + N \rightarrow \nu(l) + X$, calculated in the framework of effective theory, is

$$\frac{d^2\sigma(\nu N)}{dxdy} = \frac{2G_F^2 M E_\nu}{\pi}\left(\frac{M_W^2}{Q^2+M_W^2}\right)^2\left[xq(x,Q^2)+x\bar{q}(x,Q^2)(1-y)^2\right], \tag{1.12}$$

where M is the mass of the nucleon, M_W the W mass, $G_F = 1.16632 \times 10^{-5}\text{GeV}^{-2}$ the Fermi constant and y is the fraction of energy loss which has the expression

$$y = \frac{E_\nu - E_\mu}{E_\nu}, \tag{1.13}$$

[10] Those variable are typical to describe a deep inelastic scattering process. They are defined as the momentum fraction of the proton carried by the parton and the negative of the square four-momentum transfer (see figure 1.9)

$$\begin{aligned} Q^2 &= -q^2 \\ x &= \tfrac{Q^2}{2p\cdot q}. \end{aligned}$$

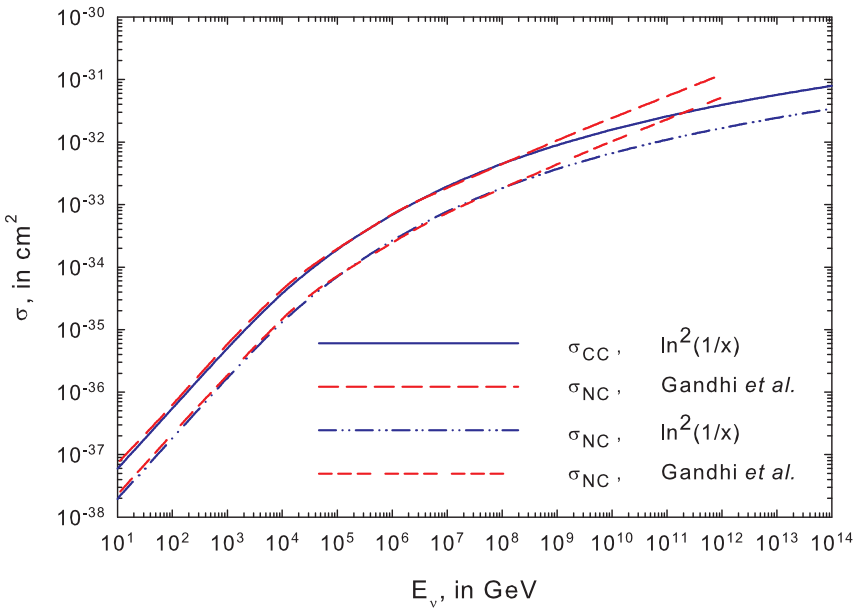

Figure 1.10: High-energy neutrino-nucleon cross section [109].

where $E_\nu - E_\mu$ is the energy loss in the rest reference frame. In equation (1.12), q and $\bar{q}$ are the quark and anti-quark distributions, labelled V for valence and S for sea. These distributions are composed as:

$$\begin{aligned} q(x,Q^2) &= \frac{u_V(x,Q^2)+d_V(x,Q^2)}{2} + \frac{u_S(x,Q^2)+d_S(x,Q^2)}{2} \\ &+ s_S(x,Q^2)+b_s(x,Q^2) \\ \bar{q}(x,Q^2) &= \frac{u_S(x,Q^2)+d_S(x,Q^2)}{2} + c_S(x,Q^2)+t_S(x,Q^2) \end{aligned} \quad (1.14)$$

The total neutrino cross section is obtained integrating the double differential $\frac{d^2\sigma}{dxdy}$ on the kinematic variables. The cross section given in terms of the structure functions F_2,F_3 and F_L is

$$\sigma(\nu N) = \left(Y_+ F_2^\nu(x,Q^2) - y^2 F_L^\nu(x,Q^2) + Y_- x F_3^\nu(x,Q^2)\right) \quad (1.15)$$

The results published by the ZEUS collaboration [107] provide a range of values for F_2. The total cross sections are shown in figure 1.10, for both charge and neutral current scattering. At the region around the TeV the neutrino and antineutrino cross sections differ, due to the valence contribution to F_3, becoming significant at high x.

Chapter 2

The AMANDA Neutrino Detector

AMANDA is a Cherenkov detector at the geographical South Pole. It consists of a lattice of photomultipliers deployed in the ice and connected via cables to the surface. The Antarctic ice provides a transparent Cherenkov medium for light production. The detector was built in several stages, and we refer in this analysis to its last configuration named AMANDA-II. Neutrinos are detected through their charged interaction products. When a neutrino-induced lepton traverses the ice, Cherenkov photons illuminate the several photomultipliers. A high multiplicity in such light signals triggers the data acquisition system which records the event in a specific ASCII format called F2K. Time and location of each hit are stored on tape and later transfered North. The challenging geographical environment in which the detector is built makes it necessary to control the most of the operations remotely. A monitoring software samples some quantities from the data to check on their quality and transfers this information North in real time. A correct understanding of the ice optical properties has been achieved during deployment with the use of a standard candle and reproduced with a simulation; its structure is determinant to interpret the systematic uncertainties affecting our measurements.

2.1 Neutrino Detection and Cherenkov Effect

Neutrinos are the only particles in the Standard Model which just interact weakly. This makes their direct observation technically impossible with the current detectors, and suggests an indirect detection through particles resulting as a product of neutrino interactions. Neutrinos are detected in AMANDA by the Cherenkov light produced by their charged interaction products. A detectable event is a charged lepton of family l produced out of a neutrino ν_l in a charged current scattering process happening on a nucleon in ice (see figure 2.2). The charged current cross section for the process $\nu_l N \rightarrow l^{\pm} X$ lowers the

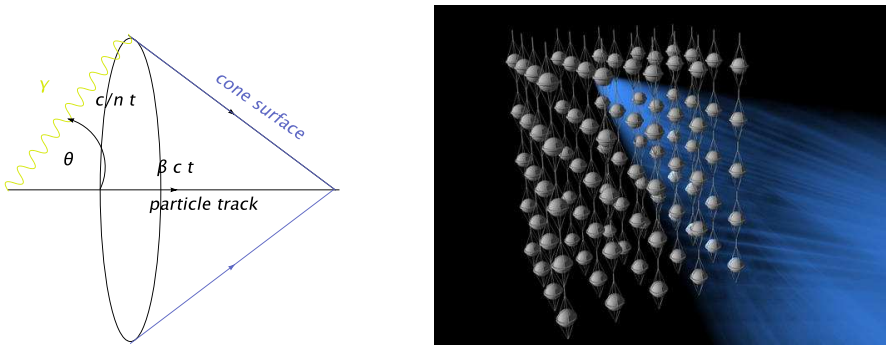

Figure 2.1: Left: Cherenkov cone. The phase refraction index of ice is $n_p = 1.32$, meaning for highly relativistic muons an angle $\theta = 41\,^\circ$. Right: the appearance of Cherenkov light in the detector

rate of detectable neutrino events, making it necessary to compensate for it with very large instrumented volumes.
The emission of light by Cherenkov effect occurs when a charged particle traverses a transparent medium faster than the velocity of light in that medium. Light propagates in a medium of group refraction index n_g with velocity

$$c_{\text{medium}} = \frac{c}{n_g}. \tag{2.1}$$

When a charged particle propagates with a velocity bigger than this value, photons emitted remain constrained in a cone whose opening angle depends on the refraction index of the medium ($\cos\theta_C = 1/n_p$), as illustrated in figure 2.1. In the specific case of ice, however, the distinction bewteen group and phase indices can be neglected [65]. Cherenkov effect appears for

$$v_{\text{particle}} > \frac{c}{n} \Leftrightarrow \beta_{\text{particle}} > \frac{1}{n}. \tag{2.2}$$

Cherenkov light in ice extends to visible wavelength and appears light blue. It is the most commonly used detection technique for neutrinos; recently, radio and acoustic detection have been developed, but they remain at the current time in an experimental phase. Photomultiplier tubes convert a light signal into a pulse that can be transmitted to the surface. A charged lepton which enters the instrumented volume originates a high multiplicity of such light signals, which trigger the data acquisition system. We will describe later in this chapter which quantities are recorded. The basic concept is that the set of pulses (or hits) recorded by the detector allows for a later reconstruction of the lepton track. Muons produce a linear signature traversing the ice. Relating the direction of the detected lepton to its parent particle is straight-forward, as the angle between the two has been estimated in [70] as

$$\theta_{\nu\mu} \approx \frac{0,7\,^\circ}{(E_\nu/\text{TeV})^{0.7}}. \tag{2.3}$$

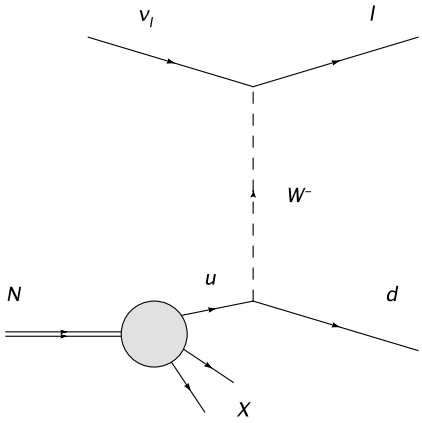

Figure 2.2: Charged current neutrino-nucleon scattering. If such a process happens on a proton or neutron in ice, in the vicinity of the instrumented volume of the detector, the outcoming lepton track is revealed via Cherenkov light.

At the energy range of atmospheric neutrinos, the two particles are almost collinear. Not all leptons derive from a neutrino interaction; they can also be directly produced from cosmic rays. We refer as 'background' to the leptons which do not derive from a neutrino, and 'signal' for those who do. To filter out this kind of background, most of the neutrino telescopes use the Earth itself as a screening medium. The choice is due to the fact that neutrinos can travel almost undisturbed across rock, iron and heavy matter while all charged leptons are stopped because of their shorter interaction lengths. Only lepton tracks coming from across the Earth are considered, i.e. those from the opposite hemisphere with respect to the geographical position of the detector.

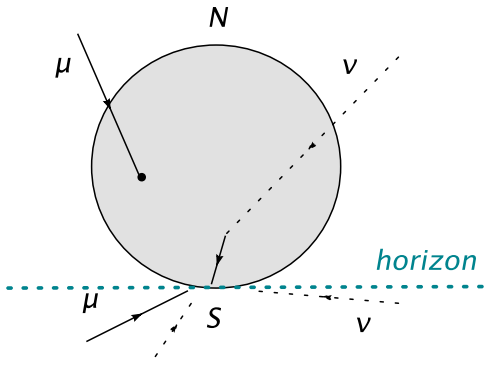

Figure 2.3: The filter provided by the Earth: neutrinos are the only particles able to travel across it.

2.2 Short Profile of the South Pole Glacier

Antarctica is entirely covered by a glacier of very ancient formation whose depth rises to a few kilometers in the central part of the continent. Ice layers originate from continuous hoarfrosts, although of moderate proportion due to the extremely low precipitable water vapour in the atmosphere [42]. In this cold and dry climate, snow crystals grow in a simple form, different from the common snow, as the exagonal prisms shown in figure 2.4. The fact that the Antarctic glacier moves very slowly implies that the ice we observe at the current days is rather old. The inner part of the Antarctic continent is a dry and cold desert at high altitude. The complete lack of external light pollution and the stability for seasonal changes indicate it as an optimal location for astronomical observations of several types. Antarctic ice is a good medium for Cherenkov neutrino detection because of the low concentration of radioactive isotopes which increase background rates. Its optical properties, fundamental for photon detection, strongly depend on some dust layers deposited as the glacier grew. A different chemical composition characterises the different geological eras in which every layer originated. In particular, four main beds of unclean ice are interposed between clear ice. From about 1000 metres depth, the ice is compact and contains no air bubbles, hence optimal for photon detection. The measurements have been performed with a "dust logger", profiting from the occasion of having holes drilled in the ice before deployment of the strings. Such a device is equipped with a light source and is deployed together with the string. During its descent in ice, it emits and records photons of known wavelength allowing for reconstruction of the ice scattering properties. The ice structure is illustrated in the next chapter, figure 3.1, with the sketch of the light propagation simulation code.

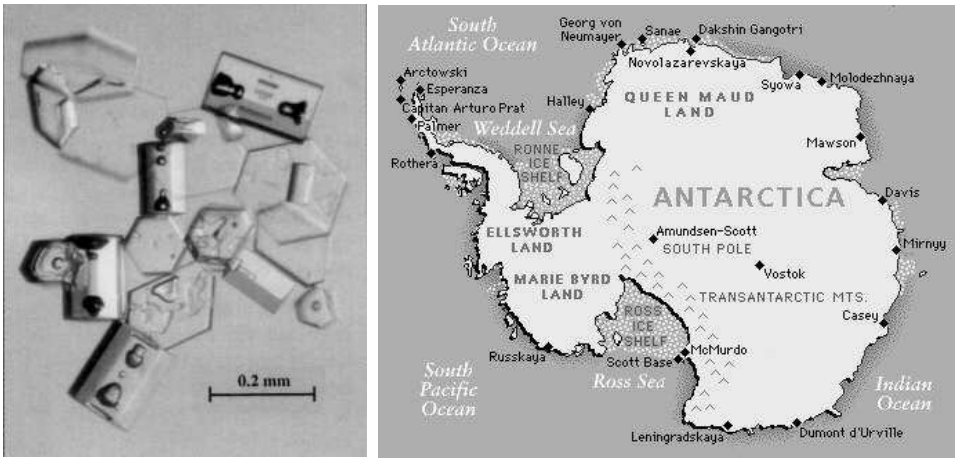

Figure 2.4: Left: the shape of snow crystals in the Antarctic ice is rather simple, due to their very slow growth [43]. Right: the Antarctic continent.

2.3 Flavour Identification - ν_e, ν_μ, ν_τ

The data collected in this analysis consist of muon neutrinos and antineutrinos; however, light signatures produced by the different neutrino flavours can be identified by their topology in the detector.
Electron neutrinos produce electromagnetic showers, originating a localised event contained in the detector volume and characterised by a few channels and a spherical shape. The short free path of the electron is a consequence of bremsstrahlung. Because of the low amount of light produced, to detect an electron neutrino event a charge current reaction must happen inside the detector. This considerably lowers the flux of such events. Such events hardly fulfill the trigger condition (see section 2.5.3) due to the limited number of hits of which they are composed, unless very energetic. The search for electromagnetic cascades in AMANDA has not yet found evidence of events [45].

Muons produce a linear track which traverses the detector, as shown in figure 2.5. The Cherenkov photons are emitted along the path originating a cone which propagates with the particle, enclosing the Cherenkov light. The typical signature for a muon event is a set of hit photomultipliers clustering along a line, and ordered according to an increasing time.

Tau neutrinos may show a typical "double bang" event topology due to the short lifetime of the tau lepton, that once created tends to decay inside short distance originating another tau neutrino. Such events, if contained in the detector, are characterised by a double vertex.

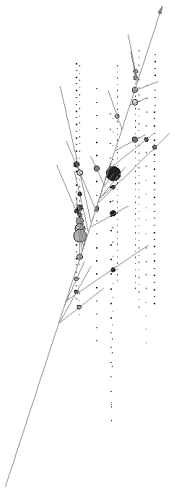

Figure 2.5: Signature produced by a muon crossing the detector. The track is reconstructed from the position and time records of the optical modules detecting light.

2.4 The AMANDA Setup in Ice

AMANDA is composed of a lattice of 677 photomultipliers embedded in the Antarctic ice at the geographical South Pole. The photomultipliers (or optical modules) are organised in a set of 19 strings which occupy a cylindrical volume of about 1.8×10^7 m^3. With the exception of string 17, which was subject to a deploying problem, all optical modules lie at a depth of 1500 - 2000 metres from the surface. The strings are distributed in three concentric cylinders of diameter 70, 120 and 200 meters. AMANDA had several con-

Figure 2.6: Left: the South Pole Station, with the AMANDA site on the right. Right: a schematic view of the AMANDA detector

struction stages starting from 1995 (as summarised in table 2.1). In its final configuration it has been taking data since the Antarctic summer 1999/2000, under the name of AMANDA-II. The deployment of the strings took place in consequent Antarctic Summers. To hole the ice a hot water drill is used[1], and the string is deployed in its final position while the ice is melt. In around 24 hours the position of the string is stabilised and the ice starts re-freezing from the top to the bottom. The complete freezing process can last years, but in general after a couple of months the string is sufficiently fixed. The disadvantage of having such a setting is that in case a module fails, it is not possible to recover it for external repair. On the other side, the resulting lattice is stable compared to similar detectors deployed in sea water. Modules are tested at cold temperatures before being shipped to the South Pole station and again once on the camp, before being connected to the string. The signal is transmitted through a cable passing in the inner part of the string. Between the years 1997 and 1998 the transmission medium has been changed from electrical to optical cable. A schematic view of the detector is illustrated in figure 2.7.

[1]The same drilling procedure is used for the current deployment of the IceCube optical modules, undergoing since 2005 up to now at the South Pole.

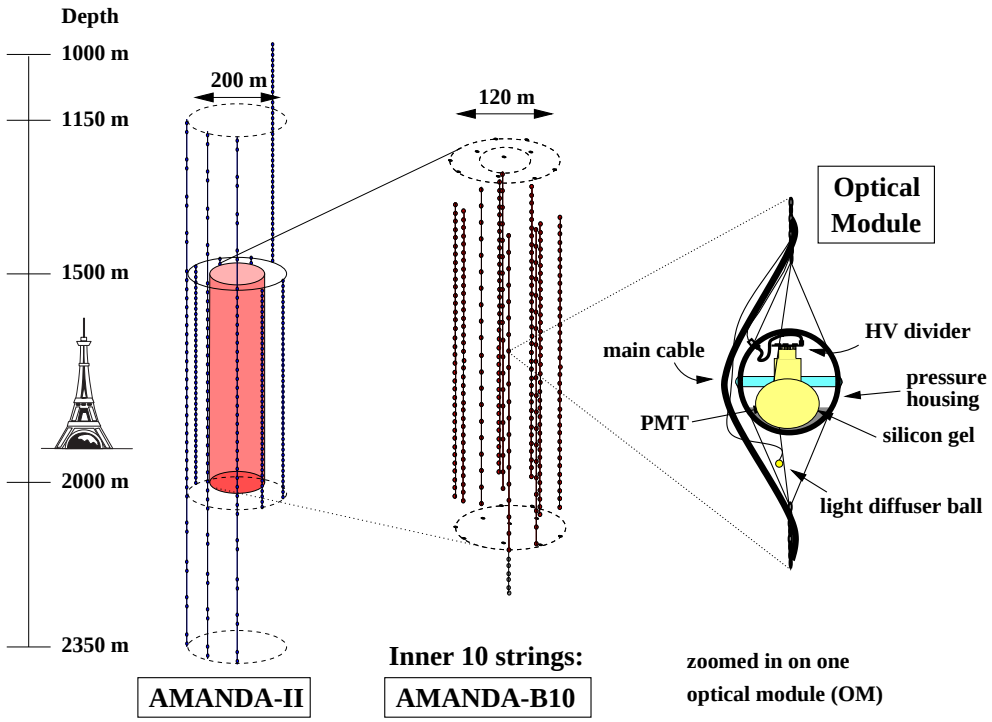

Figure 2.7: A sketch of the AMANDA detector in its components: AMANDA-B10, embedded in AMANDA-II, and a detail showing the optical module. On the left, a scale indicates the depth in the ice.

2.5 Data Acquisition

All photomultipliers are connected to the surface via coaxial, twisted pair or optical cables. On the surface, at roughly 500 meters from the geographical South pole, all cables converge to the Martin A. Pomeranz Observatory (shown in figure 2.8), where the electronics are stored. Communication with institutions in the North is achieved via satellite connection. A subset of preselected data that needs to be available soon after acquisition can be transferred via satellite; this includes monitoring and calibration data (see section 2.8) and supernova trigger warnings (see section 2.5.4).

	Season	*No. of strings*	*No. of OM*	*Transmission*
AMANDA-B4	1995/96	4	86	electrical (coaxial)
AMANDA-B10	1996/97	10	302	electrical (twisted)
AMANDA-B13	1998/99	13	428	optical
AMANDA-II	1999/00	19	677	optical

Table 2.1: The subsequent AMANDA construction phases and configurations.

Figure 2.8: Left: the Martin A. Pomeranz Observatory (MAPO), hosting the AMANDA data acquisition system. Right: AMANDA string n. 10, in front of the MAPO door

2.5.1 The AMANDA Optical Module

The detector unit of AMANDA is a photomultiplier enclosed in a thick glass shell; the set of the two is often called optical module, or OM. The photomultiplier is placed in the lower half-sphere, embedded in silicon gel. All AMANDA modules look downwards, as the detector is optimised for the detection of neutrinos coming from the Northern hemisphere. Many optical modules are equipped with an artificial light source used as calibrating signal. This source emits light at different frequencies and calibration is repeated every year. The photomultiplier used in AMANDA is an Hamamatsu R5912-02. The gain factor of such a device reaches 10^9, while the nominal value given for the noise rate is about 6000 Hz, which is strongly reduced in ice at $-40\,^{\circ}\mathrm{C}$. The first optical modules to be deployed had an electrical connection to the surface, whilst mixed optical and electrical cables were used for the following stages. The length of the connecting cables can reach values of about 2 km, which brings up the problem of signal dispersion along the way. For this issue the high gain factor of the photomultiplier is fundamental. The optical transmission does not suffer from this problem.

2.5.2 The Data Acquisition System

On the ice surface all cables gather in the counting house (MAPO). The electrical signal is amplified[2]; signals coming from optical cables are collected in the optical receiver board. The complete DAQ is sketched in figure 2.10. The analog signal coming either from the amplifiers or from the optical receiver board is turned into a rectangular pulse by a discriminator. The leading and trailing edges of the pulse are measured in time-to-digital converters (TDC).

[2]The amplifiers are named SWAMPs, produced by the Swedish part of the AMANDA Collaboration

Figure 2.9: Left: AMANDA optical modules, composed by a photomultiplier enclosed in a glass sphere. Right: Deployment of a string in ice seen from the surface.

In parallel, both signals are sent to the trigger system. When an event is triggered, the TDCs are read out by the data acquisition system. The TDC capacity allows the storage of up to 16 edges per OM in 32 μs, distributed as $[-22\,\mu s, +10\,\mu s]$ around the triggered time. The TDCs have a resolution of 1 ns. Simultaneously, an analog to digital converter (ADC) converts and records the maximum value of the pulse in a 10 μs window. In case a photomultiplier gives more than one pulse, the highest value is recorded. TDC, ADC and the whole trigger logic are hosted by crates as shown in figure 2.13. The whole system is synchronised on a GPS clock. Information coming from both the TDC and ADC are collected and sent to the DAQ. The muon DAQ takes about 2.5 ms to record an event, during which no data acquisition is possible.

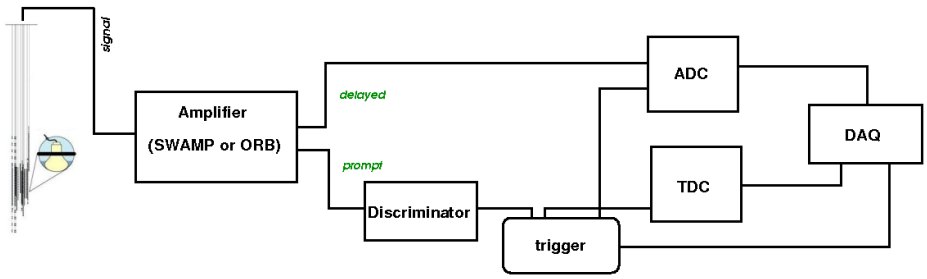

Figure 2.10: A schematic representation of the AMANDA DAQ. The signal coming either from the amplifiers or from the optical receiver board is sent in parallel to the trigger and to the TDCs. If the trigger condition is fulfilled, the DAQ is started.

2.5.3 Trigger

The trigger logic has the function of collecting pulses from the different optical modules and deciding within a short time if they form a signal. When the trigger condition is fulfilled, the event is recorded by the data acquisition system.

Multiplicity Trigger

A neutrino-induced muon traversing the ice originates photons along its track. A certain amount of light is deposited in the detector inside a short time interval. The multiplicity trigger looks for coincident signals inside a time window of 2500 ns. It is implemented with an adder, which sums up all the pulses inside this time and checks whether the result reaches a threshold. The required minimum number is $N = 24$ pulses for an event to pass the trigger; this value has been set and remains constant since year 2000.

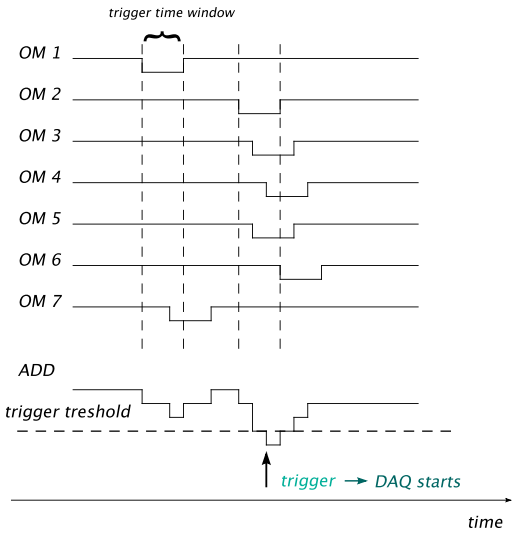

Figure 2.11: Scheme of the adder providing the multiplicity trigger. When N pulses are recorded within a time window od 2,5 μs the event triggers the detector DAQ.

String Trigger

It is reasonable to assume that out of the set of light signals produced by a track, several should belong to the same string. On the other hand, isolated signals without close neighbours are likely to be due to electronic defects rather than to a lepton event. The string trigger condition requires a combination of n modules out of m on the same string (the value of n varies according to the years). It has been working in addition to the multiplicity trigger since 2001.

External Trigger

An additional trigger condition is established by considering other detectors which work in coincidence with AMANDA, as the surface array SPASE2 (South Pole Air Shower Array), which helps to identify tracks entering the detector from the upper surface (south direction). Coincident events can be identified and rejected as background.

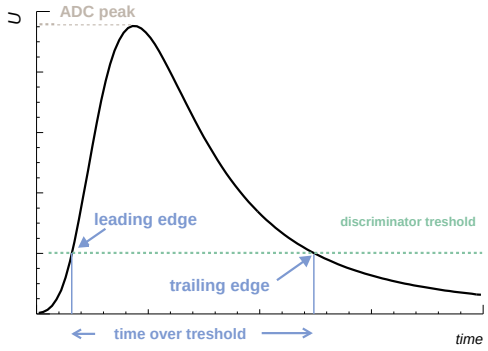

Figure 2.12: The shape of the ADC pulse recorded by the muon DAQ. The quantities recorded, leading edge, trailing edge, time over threshold and ADC peak, are the basis for the reconstruction of a neutrino-induced lepton track.

After the event has passed the trigger conditions, it is recorded by DAQ. Each light signal is recorded as a pulse with three basic pieces of information: the starting time or *leading edge*, the *time over threshold*, which is the time interval during which the voltage remains higher than the normal noise rate, and the *ADC*, which is the voltage peak. In addition to the standard muon DAQ, the transient waveform recorder (TWR) data acquisition system was installed at the Pole in the Antarctic summer 2001/2002. The TWR modules read out the signal from either the amplifiers or the optical receiver board and keep a record of the whole pulse with its functional form. The TWR DAQ records events at a frequency of about 150 Hz and has a much smaller dead time between two events, so that the trigger condition can be lowered at $N = 18$ events. The values recorded are sketched in figure 2.12

2.5.4 The Supernova DAQ

The supernova data acquisition system runs parallel to the muon and TWR DAQ. It is optimised for neutrino searches at very low energy as expected in the case of a supernova explosion [47]. This data acquisition system, in contrast to the muon DAQ, has no trigger threshold because low energy events do not emit enough Cherenkov photons to pass the condition. For each optical module, the deviation from the average rate is recorded. If the rate exceeds a certain threshold value, a program switches the binning to a finer value

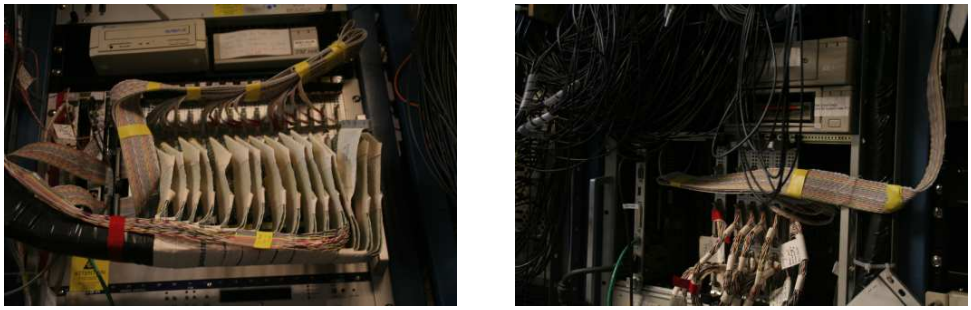

Figure 2.13: Some components of the muon DAQ. Left: one of the AMANDA crates - right: the DMADs, discriminator and adders which compose the trigger logic. Both are located in the Martin A. Pomeranz building.

and maintains this setting for 10 minutes. Triggers from the superova DAQ need to be transferred North in almost real time, as in case of a supernova explosion neutrinos precede the event by about two hours, and would allow for a prompt alert to optical telescopes which could be pointed directly at the object. AMANDA and IceCube take part in the Supernova Early Warning System network together with other neutrino detectors and telescopes, with the aim is to take note of neutrino excess and communicate it in real time to other detectors to check the coincident observations.

2.6 Data Storage

Data are recorded in an ASCII format named F2K and stored in packages of about 50 MByte each. The F2K format has been developed to offer good user readability and the interface to different applications, as filtering, reconstruction, calibration, analysis software, with different programming languages. A F2K file contains all the information about a triggered event: GPS time, number and position of each optical module contributing to the signal, time over threshold and ADC of each channel. A few first level reconstructed quantities (direction of the track, neutrino flavour) are as well recorded. An example is illustrated in figure 2.14. Later we will illustrate the several steps of the reconstruction chain. The typical size of a F2K file (200 MByte) covers about 8 minutes of detector time. For practical purposes F2K files are organised in runs of variable length. At this first stage of the data acquisition, a huge number of events (around 8×10^6 per day) is recorded, as they still include atmospheric muons which constitute the background for the most of the analyses.

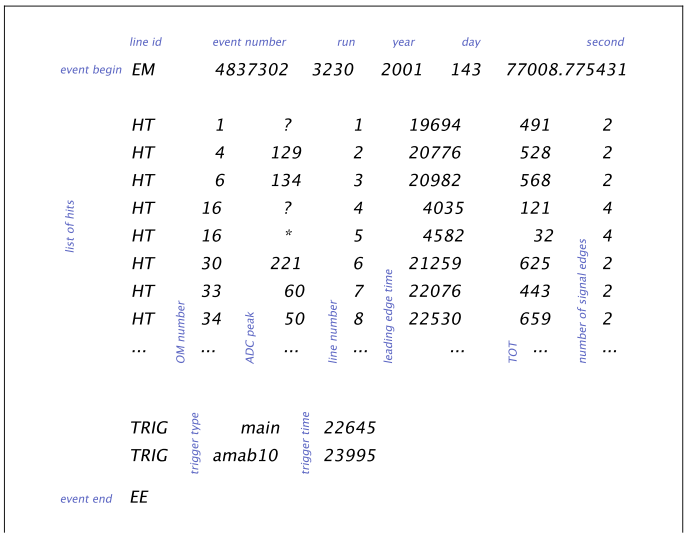

Figure 2.14: Values recorded in a F2K file. The header contains general event information. Time over threshold and leading edge time are in nanoseconds. The ADC peak is in millivolt. A question mark indicates the module has no ADC entry. Trigger time and type are in the end.

2.7 Data Transfer

The South Pole Station is connected to the rest of the World via satellite. Once recorded from the muon, TWR or Supernova DAQ, the data need to be transferred North. Normally three satellites are operating, covering a time interval of almost 20 hours per day. Standard satellites in orbit on the Equator plane cannot reach the station. In figure 2.15 a picture of the satellite coverage of the station at a certain time of the day is shown. An additional satellite communication system named *iridium* ensures a 24 hour coverage allowing data transfer and e-mail and phone contact. The satellite band width does not allow all data to be transfered in real time; only the SNEWS triggered events and the monitoring data follow this way. The complete data set is recorded to tape and shipped via airplane at the end of each season.

2.8 Data Monitoring

A monitoring software, consisting of a set of scripts installed at the Pole, checks the status of the data acquisition system and the data quality. It is fundamental to have automatic control supervising the data taking and allowing for remote operation on the electronics, as few people from the AMANDA/IceCube Collaboration remain at the South Pole station over the Antarctic winter. The monitoring system observes several values recorded by the detector. It works

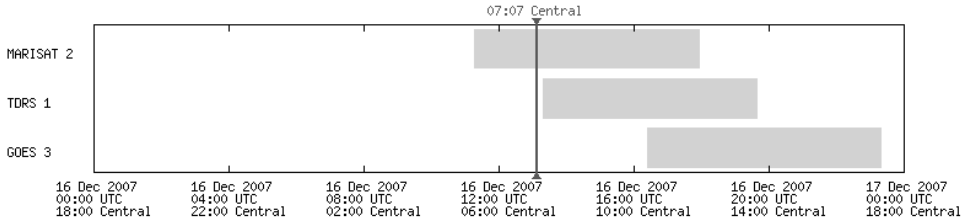

Satellite	Rise	Set	Azimuth Elevation	Other Info
MARISAT 2	11:18	17:55	325.47 - 3.82	
TDRS 1	13:21	19:38	310.15 -0.58	Currently below the horizon
GOES 3	16:24	23:18	251.66 -11.28	Currently below the horizon

Figure 2.15: The satellite covering of the South Pole Station. All times are expressed in UTC (Coordinate Universal Time). This picture refers to Central European Time 14:07.

on-line, and the most of the values are histogrammed and stored into root files at the Pole. After they are transferred to the main data warehouse in Madison, each collaborating institution contributes to the monitoring checking on the recorded values. The system is organised in runs, and recorded values are compared with the previous runs to establish whether they are within a reasonable interval from the average. In each file, global histogram are stored, which include the monitored quantities for the whole detector. The values recorded by the monitoring system at the Pole are

- ADC rates, ADC peak position, ADC peak-to-valley ratios (over a short and long period of time: values are recorded per F2K file inside a run, and per run over a larger time window, and for each channel)
- exclusive, inclusive and total trigger rates (referred to the run or longer time window). Both the single optical modules and the total detector are monitored.
- distribution of peak of trigger time per channel
- flary events fraction and flare indicator to be used as a filter flag [63]
- dark noise rates per F2K file (8 minutes) and per run (8 hours)
- dead-time fraction per channel

2.9 Detector Calibration

The strictly necessary information to reconstruct a track are the leading and trailing edge of the pulse (sketched in figure(2.12)), the amplitude peak ADC

and the location of the optical modules which gave a signal. Those quantities require a calibration of the time, amplitude and geometry of the detector. The arrival time of a photon at the photomultiplier depends on the leading edge time as

$$t = t_{LE} - t_0 - \frac{\alpha}{\sqrt{V_{ADC}}}. \tag{2.4}$$

Delays related to the signal propagation along all the cables and the electronics are included in t_0. The second term is a correction for the time delay between the pulse start and the threshold crossing, depending on the dispersion of the cable. The square root is due to the parabolic approximation of the curve shape at the beginning of the pulse.

Those two calibration constants are measured by flashing artificial light signals, produced with a laser and transmitted with optical fibres, and checking the detector response for each optical module. Amplitude calibration is related to the number of detected photoelectrons. This number depends on the photomultiplier gain, amplification factor of the SWAMPs/ORB and attenuation in cables and electronics. Down-going muon data (muons from the Southern hemisphere) are used to calibrate the amplitude of the pulse.

Finally, the geometry calibration is necessary considering that the Antarctic glacier is not fixed and small changes in the positions of modules can occur. At deployment stage, the x-y position of each string is determined by geographical triangulation and the z coordinate is accurately measured with the pressure. After the string is deployed, the positions of modules can be verified with the use of standard flashers.

2.10 The Successor of AMANDA: IceCube

From a publication of Antarctic Astronomy 1994 [51]:

"During the 1991/2 Austral Summer, a small neutrino experiment was established at the South Pole. [...] This modest telescope system is an excellent first stage in the development of a large neutrino telescope for the Antarctic Plateau. If the technique proves to be as successful as expected then a large system could be constructed [...]"

In the Antarctic season 2008/09, the AMANDA neutrino detector is going to be decommissioned while its larger successor IceCube will take over the task of neutrino detection at South Pole. A considerable effort has been made over the last years to provide the synchronisation of AMANDA and IceCube, ensuring a common data taking period for the years 2006 up to now.
IceCube will cover an instrumented volume of 1 km^3 and will result as a less dense lattice of photomultipliers optimised for the high energy neutrino detection [52]. At the moment of writing this thesis, half of the detector has been completed with 40 strings deployed in ice. Additionally, to ensure efficiency of such a telescope in the low energy region, an additional component of the detector has recently been approved and will serve to all the neutrino searches

at $\mathcal{O}$(GeV), including τ physics, search for neutrinos from supernovae and dark matter neutralino annihilation. It will be realised as a dense smaller unit placed at the bottom of the detector (IceCube deep core).
In its final configuration, IceCube will be composed of 80 strings of 60 photomultipliers each. The completed detector will reach an effective area about 30 times larger than AMANDA-II; a rate of events of roughly 5000 atmospheric neutrinos per year is expected. Besides this, the experience accumulated in more than 10 years of neutrino detection in the Antarctic ice allowed for a considerable improvement of the electronics, ensuring a loss smaller than 2% in the deployed equipment. The detector will be associated with the surface array IceTop, composed of two Cherenkov water tanks in correspondence of each string. This sub-detector will serve as a veto for cosmic ray events, allowing for neutrino detection over a 4π region. Seen the modular composition of the detector, the IceCube data acquisition system is already running at pole since 2006, providing the first data samples. Analyses achieved with the first 22 strings have already being published [48].

Chapter 3

Event Simulation

Neutrino-induced events have been simulated with a Monte Carlo method and convoluted with a simulation of the detector response. Event simulation is a useful tool to investigate the features of our measured data sample, based on the knowledge of neutrino interactions and flux. In this chapter the complete simulation chain is described, from the production of a very large statistics sample of neutrino events to the detector response simulation. The atmospheric background is reproduced as well, to improve the study of the signal to background separation. Technical details about the software implementation of the simulation are omitted, but can be found in the references.

3.1 Step 1 - Neutrino Production

Neutrino events are generated with a random starting point in the atmosphere, distributed isotropically around the Earth. Propagation to the detector location occurs without any energy loss, as the Earth is transparent to neutrinos below 1 PeV. Neutrino interactions are simulated with the NUSIM package [53]. A weighting factor accounts for the probability for each neutrino event to interact along the propagation path. The initial neutrino spectrum is simulated with a user-defined power law that can be altered with an appropriate weight. Events that can be detected in AMANDA induce a charge current scattering interaction in the vicinity of the detector producing a charged lepton. In NUSIM, the angle between the incoming neutrino and the outgoing lepton is set equal to 0 for the sake of simplicity; we mentioned in section 2.1, equation (2.3) that this angle has been estimated to be negligible at energies below 10 TeV. Another simplification in NUSIM consists of the fact that only flavour μ has been included. For the purpose of this analysis, this assumption will not bring any changes, as our data selection only includes ν_μ and $\overline{\nu}_\mu$. The initial spectrum is simulated with the power law

$$\frac{d\Phi(E)}{dE} \propto E^{-1} \tag{3.1}$$

where $\Phi(E)$ is the neutrino flux in dependence of the neutrino energy E. A re-weighting has been consequently applied to fit the energy spectrum to the actual atmospheric spectrum model [8], i.e.

$$\frac{d\Phi}{dE} \propto E^{-3.7}. \tag{3.2}$$

3.2 Step 2 - Muon Propagation

Muons propagate from the production point, represented by the vertex of the charge-current neutrino-nucleon scattering, and traverse the ice across the detector. The propagation simulation has to take all possible sources of energy loss along the path into account; the package used to simulate muon propagation in ice is MMC [54]. The calculation approximates the muon energy loss as continuous, although it is actually ascribed to discrete events (interaction, ionisation, bremsstrahlung) that occur along the particle free propagation path. This package is suitable for several neutrino experiments, hence the propagation medium can be chosen from among ice, snow, air or standard rock.

3.3 Step 3 - Photon Propagation

Muons emit Cherenkov photons which remain confined in a cone of opening angle θ_C and propagate to the optical modules[1].

The distribution of the dust in the Antarctic glacier is grouped in layers (as shown in figure (3.1)), hence photons scatter unisotropically according to the depth. To account for this asymmetry, an effective scattering length is defined as

$$\lambda_{\text{eff}} = \frac{\lambda}{1 - \langle \cos\theta \rangle}, \tag{3.3}$$

where λ is the scattering length of photons in ice, of the order of a few meters, and $\cos\theta = 0,94$ is the value of the average scattering angle measured by [58]. Dust molecules cause scattering and absorption of light; an accurate description of the photon loss has been implemented in the AMANDA simulation [44]. Photon scattering and consequent deviation from the Cherenkov cone direction make the track reconstruction more complicated.

The standard package used for photon propagation is the photon transport and detection code PTD [56], from which follows the more updated PHOTONICS [55]. Any of those models can use a different ice model simulation as input [58]. Simplifications are necessary, as lepton tracks traversing the ice can emit up to $\mathcal{O}(10^6)$ photons, whose propagation must be described through average values. The ice in PTD is modelled with tables accounting for photon detection probability in a homogeneous medium. Absorption has been estimated through a matching with a Monte Carlo simulation of the number of

[1] θ_C is the Cherenkov angle. The Cherenkov effect is described in chapter 2 2.1.

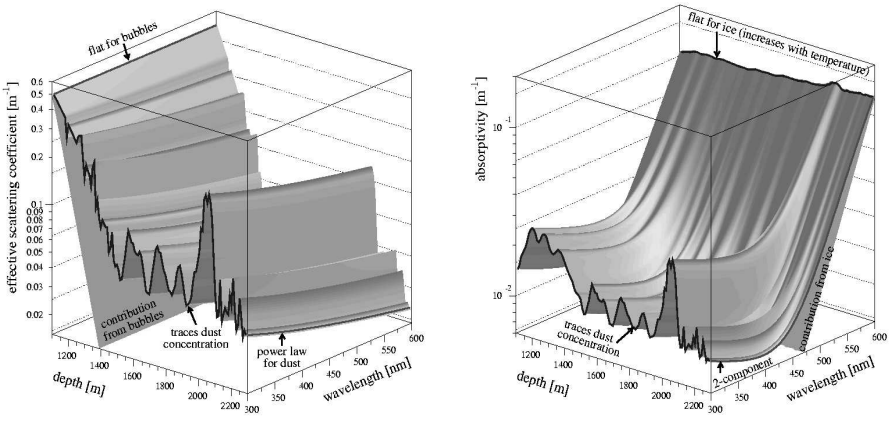

Figure 3.1: Photon scattering length (left) and absorption length (right) as a function of the depth and photon wavelength. Layers of ice of different properties are identified by the peaks. The values provided by the dust logger are $l_s = 110$ m for scattering and l_a =20 m for absorption. Both measurements were taken with respect to a photon wavelength $\lambda = 400$ nm.

photomultiplier hits composing muon events. A reference for this model (muon absorption model) can be found in [57]. PTD distinguishes four classes of absorption and scattering parameters, and groups the different photomultipliers according to their position in one of those classes. The package simulates all photons with an average wavelength $\lambda = 420$ nm. In photonics, ice layers of different optical features are accounted in the tables. We described in section 2.2 the geological origin of such a structure.

3.4 Step 4 - Detector Simulation

Data acquisition, photomultiplier response, electronics, detector dead time and noise rates are simulated and reproduced by the AMASIM software [59]. For each detected photon, the waveform from the photomultiplier is reproduced and the read-out electronics are simulated, including the delay due to the cable transfer of the pulse. The entire AMANDA electronics are installed in a challenging geographical location for detector maintenance and subject to severe weather conditions. As it is impossible to correctly simulate all the possible problems in the data acquisition, such as bad optical modules, cross-talk[2] and instability of the electronics due to weather changes, the measured data are filtered to exclude events belonging to any of the above mentioned problematic cases. Data and simulation then undergo the same selection criteria.

[2]Cross-talk is an electronic artefact. See section 4.1.

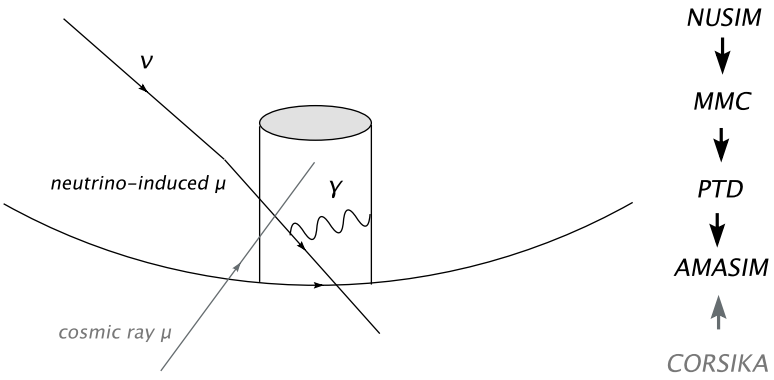

Figure 3.2: The AMANDA simulation chain.

3.5 Background Simulation

Although all the AMANDA optical modules point downwards to use the Earth as a filter, this limits but does not suppress the detection of background events, composed of charged leptons directly produced from cosmic rays. A simulation of the cosmic ray background is achieved with the CORSIKA package [60]. The simulated data sample composed of cosmic ray muons and neutrinos reproduces our measured raw data. The complete simulation chain is sketched in figure 3.2.

3.6 Weights

The introduction of weights is a way to save computing time and include a large number of different possibilities in a smaller simulated data sample. This allows the user to reproduce different neutrino spectra out of one unique simulated data sample.

An initial simulated sample is produced with a flux proportional to E^{-1}. The vertices of the charge scattering processes are simply isotropically distributed in the detector volume. This simplifies the situation considerably, in which it disregards the cross section computing and the medium density information related to the nucleon distribution. After the whole simulation chain has reproduced the final data sample, weights are applied.

One weight describes the atmospheric neutrino flux model, where the standard value is obtained with the Lipari flux calculation [91], but can be altered by the user as we will see in more detail in chapter 8. The cross section for neutrino interactions, including all the information about the scattering probability, the neutrino absorption length in the ice, the energy of the particles and the features of ice is described by a second weighting factor. The use of weights allows for a faster and less computer challenging calculation, producing a sample of $\mathcal{O}(10^6)$ simulated events.

Chapter 4

Event Reconstruction

In this chapter we illustrate the reconstruction sequence leading to the identification of a neutrino track, using the time record of each hit, and the coordinates of the channels composing the signal. The same reconstruction algorithms apply to both data and Monte Carlo simulated events, as they are recorded in the same format. Reconstruction fits are performed in increasing order of complexity, while the amount of data is reduced at each step with tighter filtering conditions. Likelihood-based algorithms, which are quite computing intensive, are applied in the last steps of the procedure. The reconstruction is implemented in the *recoos* program with use of the SiEGMuND software package. A technical reference can be found in [68].

4.1 Pattern Recognition

The AMANDA data acquisition system records pulses from the photomultipliers and stores all the values in F2K format (see 2.6). The only selection applied at this level is the fulfillment of the trigger conditions described in chapter 2.5.3. A pattern of light signals inside a short time window can be ascribed to a neutrino-induced event; aim of the reconstruction is to determine the direction of such lepton tracks. Atmospheric neutrinos, which form the signal in this analysis, are produced with equal probability around the Earth. However, the tracks coming from the Southern hemisphere are indistinguishable from the atmospheric muon background; an accurate reconstruction allows for rejection of those events. Step after step, tracks which show problematic or uncertain reconstruction are rejected. The information form the final sample of tracks is then recorded in a ROOT file in the structure of a ROOT tree.
Simulated data are produced according to the simulation chain described in chapter 3 and stored in the same ROOT format, with additional information on the true variables. From this stage on, the same selection and reconstruction criteria are applied to the measured and simulated data.

4.2 Background Classes

The recognition algorithm of a muon track can be influenced by several types of background events, that require specific filters. They are basically of two types: physical events, i.e. down-going particles, and events due to electronic artefacts.

Background of Physical Events

Multiple muons from a single air shower (muon bundles) can be misinterpreted as a single, extremely bright muon track. The energy reconstruction could fail in such case. Radiative energy loss processes, generated along the muon trajectory, can originate stochastic light emission which distorts the Cherenkov cone direction. Stopping muons, that are events which loose all their energy inside the detector, emit photons that can be interpreted as product of an up-going event. Muons that enter the detector with a nearly horizontal angle can be mis-reconstructed because of the finite resolution of the algorithm. Moreover, two or more muons from independent air showers have a small probability of crossing the detector in coincidence. Finally, the ice layers structure described in section 2.2 can distort the photon trajectories in such a way that they can be interpreted as up-going.

Background of non-Physical Events

Before proceeding with the reconstruction chain, data files recorded in unstable detector conditions or events having possible electronic artefacts are excluded. To localise such cases, the F2K files are investigated. The photomultipliers in ice have a low noise rate, however, noise and after-pulse hits must be removed. Finally, data are calibrated in time, geometry and amplitude as described in section 2.9. These processes go under the name of hit cleaning.

Flares

Flary events are events triggered as a particle, although generated by electronic noise. It can happen that randomly generated hits due to electromagnetic induction pass the trigger condition and hence are recorded as a muon event. This situation is not unlikely especially in case of storms or other bad weather conditions at South Pole, as cables connecting the strings to the MAPO building are so close to the surface, that storms can induce electromagnetic noise. Most of the suspected flary events are already excluded from the data sample by selecting only the good data taking period with the monitoring system. However, some of those events might show up in the regular data taking files and must be rejected. An algorithm to label such events has been developed

in [63], where a flare indicator is constructed on the base of some opportune variables. The probability of rejecting a real particle event by the flare filter is $< 10^{-10}$.

Cross Talk

With "cross talk" we indicate a correlation between the electronics of neighbouring optical modules. Events showing a very peaked ADC value[1] over a quite short time over threshold are likely to be due to electronic noise rather than to a real triggered event. For this reason, in the space ADC-TOT, a region of physical events is identified, outside which entries are rejected as suspected of cross-talk. The ADC-TOT dependence is fitted for each optical module with a function $f(\mathrm{TOT})$. To avoid possible rejection of physical events, the border line is shifted by 20 ns in TOT. Only the hits fulfilling the condition $\mathrm{ADC} < f(\mathrm{TOT} - 20\,\mathrm{ns})$ are considered valid for higher order reconstruction. The situation is illustrated in figure 4.1.

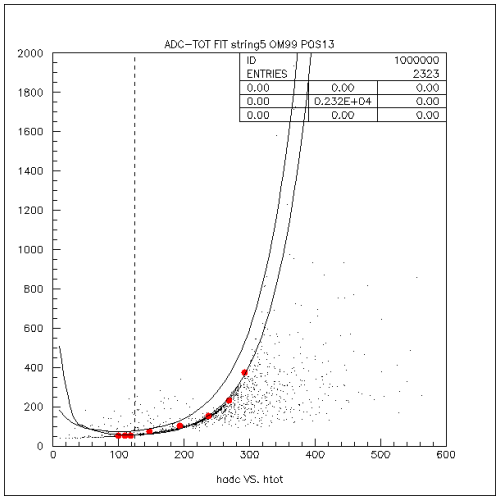

Figure 4.1: Cross talk pairs can influence the track reconstruction. Here the ADC vs TOT distribution for one channel is illustrated. The physical region lays right of the fit function. To avoid rejection of physical events, the actual function is further shifted by -20 ns (curve on the left).

[1] ADC is the maximum value of the pulse; time over threshold (TOT) is the interval in which the function has values over a noise rate threshold. Those quantities are described in section 2.5.2.

4.3 Variables used for Reconstruction

Geometry

The coordinates of the photomultiplier transmitting a signal are the basic variable used to identify a track. A muon traversing the detector produces a linear signature, along which we expect clusters of hits. Cherenkov photons illuminate a cone of opening angle $\theta_C \simeq 41°$. Muon and neutrino are almost collinear, so even though the interaction vertex can be far outside the detector, the reconstruction is straight-forward. All other possible geometries, i.e. spherical cluster of hist typical of an electromagnetic cascade, are not relevant for this analysis which looks at muon neutrinos only.

Time Residual

Given a track hypothesis, and a point laying on the track, it is possible to evaluate the expected arrival time of a photon at every optical module. The solution is unique if we assume a scattering-free medium. The time residual, defined as the difference between the observed and the expected arrival time of a Cherenkov photon, is a useful variable for reconstruction, as it gives a measure for the weight of each hit in the reconstructed track. The situation is illustrated in figure 4.2. The coordinate of a particle propagating at the velocity of light is

$$l(t) = l_0 + c(t - t_0)\hat{d}, \tag{4.1}$$

where $\hat{d}$ is the direction versor of the track. The initial initial condition is the point $l_0 = l\,(t_0)$. The time of arrival in point C is

$$t_C = t_0 + \frac{1}{c}(\vec{r}_{OM} - \vec{l}_0) \cdot \hat{d}. \tag{4.2}$$

The distance of the optical module from the track, indicated with ρ in figure 4.2, can be written as

$$\rho = |\,(\vec{r}_{OM} - \vec{l}_0) \wedge \hat{d}\,|. \tag{4.3}$$

The geometry of the situation is described by the Cherenkov angle θ whose value, for very relativistic particles, depends only on the phase refraction index n_p of the propagation medium. Light propagation in ice is determined by the group refraction index n_g:

$$c_{\text{ice}} = \frac{c}{n_g}. \tag{4.4}$$

In the pure geometrical, scattering free case, the expected arrival time of a photon at an optical module with coordinate $\vec{r}_{\text{OM}}$ (point D) is

$$t_e = t_C + \frac{\rho}{c}\left(\frac{n_g}{\sin\theta} - \frac{1}{n_p \sin\theta}\right). \tag{4.5}$$

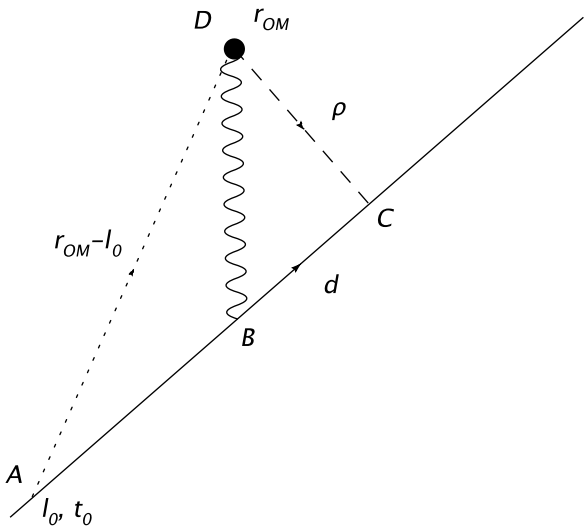

Figure 4.2: Sketch of the distance travelled by photons to reach an optical module. The Cherenkov angle, for particles with $\beta = 1$, is $\widehat{CBD} = 41°$. A photon travelling unscattered follows the path BD. A general point of the track $l_0\,(t = t_0)$ is the initial condition.

If t_γ is the observed photon arrival time at the optical module, and t_e the expected arrival time, the time residual is defined as the difference

$$t = t_\gamma - t_e, \tag{4.6}$$

The distribution of the variable t is determined by different effects: physical, as scattering and showers, and electronic, as jitters and random noise.

4.4 Reconstruction Fits

The main reconstruction algorithms are described in a sequence according to their growing complexity. A detailed list of all fits and filter conditions applied to the data sample of this analysis is reported in appendix A.
Two fits of rather simple implementation (direct walk and JAMS) allow for a first guess of the track direction, making it possible to reduce the amount of triggered events from about $8 \cdot 10^9$ to the order of 10^6. More than 95% of cosmic ray background can be identified and rejected at this level, before undergoing an elaborated reconstruction. To this reduced data sample, likelihood-based fits are applied, based on the starting values provided by the first guess algorithms.

4.4.1 First Guess Methods

Direct Walk

This is a first approximate fit to try to estimate the direction of a muon traversing the detector [61]. The algorithm considers all the pairs of optical modules transmitting a signal in a certain time window $\Delta t = 30$ ns and assuming as a track hypothesis the line passing through the two points. The condition is that the two optical modules are separated by a distance $d > 50$ m. This ensures a certain resolution, as one scattered photon could contribute twice if the optical modules considered were close to each other. In case of events with high hits multiplicity, there can be many candidate tracks: if their number exceeds 200, the procedure is started again within a smaller time window $\Delta t = 25$ ns. The quality of the reconstructed track is established considering the distribution of all hits inside the selected time window. Time residual and distance of the photomultipliers from the track are evaluated for each hit, and a parameter is determined to evaluate the quality of the reconstruction:

$$Q = \min(N_{\text{hits}}, 30\,\sigma + 7), \tag{4.7}$$

where σ is a measure of the spread of hits along the line:

$$\sigma = \frac{1}{N}\sum_i (d_i - \bar{d})^2. \tag{4.8}$$

Tracks with $Q > Q_{\max}$ are selected, where $Q_{\max}$ is the maximum for all candidates in the event. Since there can be more than one candidate track, a cone of opening angle 15° around each track is considered and the number of other candidates belonging to that cone is counted. In the end the cone with the largest multiplicity is selected, as exemplified in figure 4.3.

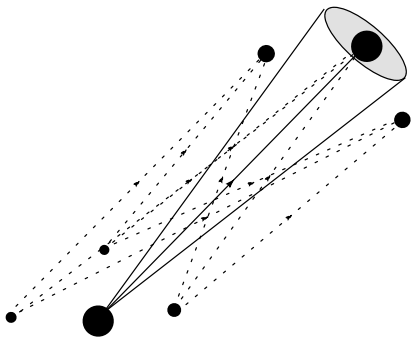

Figure 4.3: The direct walk fit geometry. A possible neutrino track is estimated considering pairs of distant optical modules, connecting them with a line and searching for the cone around the line having the highest multiplicity of possible candidate tracks.

"Just Another Muon Search"

This algorithm (often shortened JAMS) is meant to identify a typical misinterpreted event composed by two nearly simultaneous down-going muons reconstructed as an up-going event. It is possible that two almost coincident down-going particles traverse the detector so that the lower event slightly precedes in time the upper one. Such a pattern in the set of hit photomultipliers would be easily misinterpreted as an up-going neutrino. The fit algorithm is based on an analysis of the hit topology [62].
The coordinates $(x_0, y_0, c\,t_0)$ of hit signals are investigated[2]. A search for clusters of hits is performed along 26 regularly spread directions, defined by cones of an opening angle of 25°. Clusters with the higher hit multiplicity are selected, and a track candidate is reconstructed on the direction of the cone axis, taking as a reference point the average coordinates of the hits in the cluster. The expected arrival time at the second cluster is evaluated (see figure 4.4). For each track, defined by a set of parameters (x, y, z, θ, ϕ), a basic likelihood function is defined as a product over all hits of Gaussian distributions around the time residual. A quality parameter is assigned to each track, investigating the distribution of neighbour hits. Track candidates which fit a down-going hypothesis are identified and rejected.

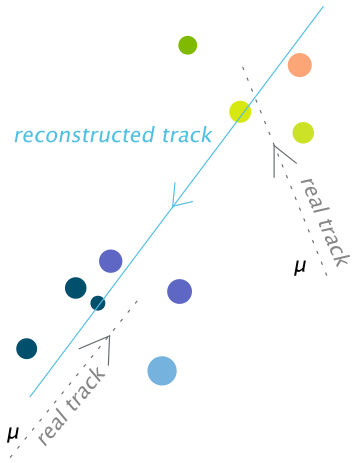

Figure 4.4: The situation in which two down-going muons are misreconstructed as an up-going particle. This track should be rejected by the JAMS algorithm.

[2]written here respect to a reference frame where the z axis is the versor of of the particle direction

4.4.2 Advanced Reconstruction

The reconstruction of a lepton track out of a pattern of light signals is a typical problem of likelihood maximisation. It can be summarised as the question to estimate a set of parameters $\{\mathbf{a}\}$, given a set of measured values $\{\mathbf{x}\}$. If $\mathcal{P}(x_i, \mathbf{a})$ is the probability density function of observing the value x_i for given values of the parameters $\{\mathbf{a}\}$, a likelihood function is defined as

$$\mathcal{L}(\mathbf{x}|\mathbf{a}) = \prod_i \mathcal{P}(x_i, \mathbf{a}). \tag{4.9}$$

The maximisation of $\mathcal{L}(\mathbf{x}|\mathbf{a})$ gives an estimate for the parameters $\{\mathbf{a}\}$. All fits based on likelihood maximisation use an initial track hypothesis from a first guess method. In the AMANDA pattern recognition procedure, a likelihood function is assigned to the track. The measured values $\{\mathbf{x}\}$ can be either the time residual, or the hit photomultipliers coordinates, whilst the quantities to be determined $\{\mathbf{a}\}$ are the geometrical parameters of the track, i.e. one point (x, y, z) and one direction defined in polar coordinates by the zenith and azimuth angles (θ, ϕ). The best track is obtained by varying those parameters until the minimum of the likelihood function is found.

Likelihood based on the Pandel Function

The Pandel function is an analytical parameterisation of the photon arrival time distribution, analysed for the case of an isotropic, monochromatic source [64]. The probability density of photon arrival time at distance d is parameterised as

$$\mathcal{P}(t, d) = N_0(d)\, \frac{t^{\frac{d}{\lambda_s}-1}\, \tau^{\frac{-d}{\lambda_s}}}{\Gamma\left(\frac{d}{\lambda_s}\right)}\, e^{-\left(\left[\frac{1}{\tau}+\frac{c}{\lambda_a}\right] t+\frac{d}{\lambda_a}\right)}, \tag{4.10}$$

where N_0 is a distance-dependent normalisation constant, and $\tau = 557\,\text{ns}$, $\lambda_s = 33.3\,\text{m}$ and $\lambda_a = 98\,\text{m}$ are parameters related to ice properties. Details can be found in the reference quoted.
Given a certain track hypothesis τ, the probability density functions $\mathcal{P}(t)$ of measuring a photon arrival time t are considered, assumed that the hypothesis is true. A likelihood function based on the photon arrival times is defined as

$$\mathcal{L} = \prod_i \mathcal{P}(t_i|\tau), \tag{4.11}$$

where t_i are the observed photon arrival times at the i-th optical module. The track is dependent on the five parameters: $\tau = \tau(x, y, z, \theta, \phi)$. The variation of this hypothesis in the parameter space which shows the maximum likelihood value is taken as a best guess for the true direction of the particle. The main numerical problem is represented by the fact that the maximisation algorithms might converge around a local maximum. To avoid this problem,

the algorithm is performed a certain number of times with random track hypotheses ("n-fold iterative likelihood fit").
Furthermore, expression (4.10) is to be convoluted with the fluctuation probability of the single optical module, which is assumed to be Gaussian distributed. This results in the probability

$$\mathcal{P}'(t,d) = \int_{-\infty}^{+\infty} \frac{1}{\sqrt{2\pi}\sigma_t}\, e^{-\frac{(t-t')^2}{2\sigma_t^2}}\, \mathcal{P}(t',d)\, dt'. \tag{4.12}$$

The angular resolution of the tracks obtained with a likelihood-based algorithm is largely improved, reaching the precision of 2.5°, from the initial 7.5° of the direct walk fit.

Bayesian Likelihood

The Bayesian algorithm is developed to try whether an hypothesis of down-going particle could match the reconstructed up-going track. A large fraction of apparently up-going neutrino tracks are in fact misreconstructed muons arriving with the same Cherenkov angle, as shown in figure 4.5, and must be rejected to resolve the signal. Instead of searching the best track for a given a set of measured quantities, one could ask how likely is that another known source produced the observed signal. The key of the Bayesian algorithm is to assume an a-priori knowledge of the muon flux, and reconstruct the track as forcely down-going. The information is based on measurements of down-going muons recorded in AMANDA, and used as a weight for the track hypothesis. According to Bayes' theorem [70], the probability that a hit pattern $\mathcal{H}$ observed in the data is reconstructed as a muon track μ is

$$\mathcal{P}(\mu|\mathcal{H}) = \mathcal{P}(\mathcal{H}|\mu)\frac{\mathcal{P}(\mu)}{\mathcal{P}(\mathcal{H})}. \tag{4.13}$$

$\mathcal{P}(\mathcal{H}|\mu)$ is the likelihood that a muon is responsible for the hit pattern $\mathcal{H}$ observed in the data; $\mathcal{P}(\mu)$ is the probability of having a muon, assumed the prior knowledge of the flux, and $\mathcal{P}(\mathcal{H})$ a normalisation representing the probability of a pattern $\mathcal{H}$. A bayesian likelihood can then be defined based on the probability obtained from expression (4.13)

$$\mathcal{L}_B = \prod_{\text{hits}} \mathcal{P}(\mu|\mathcal{H}). \tag{4.14}$$

As we are interested on the zenith angle of the reconstructed event, we consider a polynomial fit $P(\theta)$ which weights the track fitting it to the muon flux curve. With this assumption, the Bayesian likelihood can be put in the form

$$\mathcal{L}_B = P(\theta)\, \mathcal{L}(t|d,\theta), \tag{4.15}$$

where $\mathcal{L}$ is the general likelihood, evaluated from the time residual, and θ the zenith angle of the track. Comparing the likelihood of a reconstruction fit

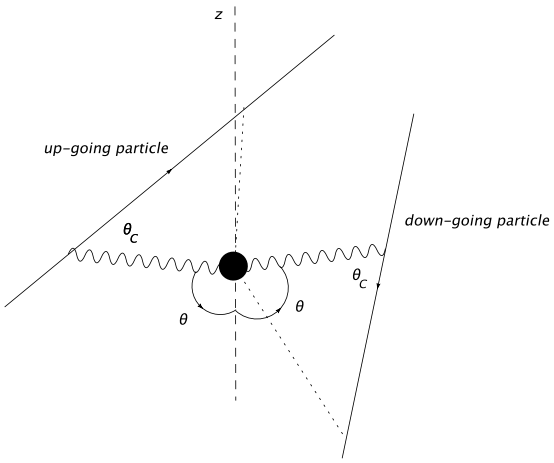

Figure 4.5: Two particles, one down-going and the other up-going, can have the same photon arrival angle at one optical module.

with the Bayesian likelihood, it is possible to reject additional background of misreconstructed down-going particles.

Likelihood based on Hit Probability

The evaluation of the hit probability of each optical module, as a function of its distance from the track, allows for the definition of a likelihood function which does not depend on the time residual, but is purely geometric. The not-hit probability of an optical module is determined by $1 - P_{\mathrm{hit}}$ and increases with the distance. The likelihood function of a track hypothesis is constructed in this case as the joint probability that hit channels be hit, and quiet channels not be hit, for a given event [65]

$$\mathcal{L} = \prod_{i=1}^{n_{\mathrm{hit}}} P^i_{\mathrm{hit}} \prod_{i=n_{\mathrm{hit}}+1}^{N_{\mathrm{OM}}} P^i_{\mathrm{no-hit}}, \tag{4.16}$$

where n_{hit} is the number of hit channels, and n_{OM} the number of total channels (677 for AMANDA).
The $\mathcal{P}_{\mathrm{hit}}\mathcal{P}_{\mathrm{nohit}}$ method reconstructs tracks with an improved resolution respect to the Pandel likelihood fit. A reconstruction with this algorithm has been applied to the Mainz L6 data sample (see 5.3), and used in this analysis as standard reconstruction fit. The method of hit probability has been used in this work, chapter 6 to estimate the detector efficiency.

4.4.3 Reconstruction of the Energy of a Lepton Track

The number of emitted Cherenkov photons depends on the energy of the muon track. A likelihood function as the one defined in expression (4.16), which

takes into account the expected and observed number of hit signals, can be used to estimate the muon energy. Assuming that the photon arrival times are described by the Pandel function (4.10), the light intensity at distance d can be obtained from the integral

$$W(d) = \int_0^\infty \mathcal{P}(d,t)\, dt\,. \tag{4.17}$$

The average number of detected photons $n(d,\theta,E)$ can be expressed as [66]

$$n(d,\theta,E) = \frac{a(\theta,E)}{W(d)} + b\,, \tag{4.18}$$

where θ is the zenith angle, and E the energy of the lepton track. The coefficient a contains the photomultiplier quantum efficiency, and b accounts for noise contribution.
Let $\mathcal{P}^{(1)}_{\rm hit}$ be the hit probability for a single photon. The no-hit probability for one single photon is $1-\mathcal{P}^{(1)}_{\rm hit}$. From this, the no-hit probability for n photons can be obtained as

$$\mathcal{P}^{(n)}_{no-hit} = \left(1-\mathcal{P}^{(1)}_{\rm hit}\right)^n, \tag{4.19}$$

as for the composed probability for independent events. This last expression represents the probability that given n photons, *none* hits the photomultiplier. At this point one can write the hit probability generalised to n photons:

$$\mathcal{P}^{(n)}_{hit} = 1-\mathcal{P}^{(n)}_{\rm no-hit} = 1-\left(1-\mathcal{P}^{(1)}_{\rm hit}\right)^n. \tag{4.20}$$

Expression (4.20) represents the probability that, given n photons, *at least one* is seen.
The energy of a lepton is a sixth track parameter, further to the five geometrical (x,y,z,θ,ϕ). In principle, it could be estimated minimising the likelihood in a six-dimensional space, but from a technical point of view, the numerical procedure gets slower. Therefore the energy reconstruction is performed in two steps: first the geometry of the track is reconstructed, and then a second minimisation leads to a best estimate for the enegy. This procedure is possible only in those cases where the measured values given as an input to the likelihood function do not depend on the energy, as in the case of the $\mathcal{P}_{\rm hit}\mathcal{P}_{\rm nohit}$ likelihood. For other cases, as for the likelihood based on the amplitude value, the minimisation must be achieved in one unique step.
As mentioned in section 2.3, most of the muons traverse and exit the detector. This fact limits the information about the actual number of Cherenkov photons emitted, so that in case of very energetic events the energy is often underestimated. The energy estimator provided by this algorithm has been corrected with a polynomial function [74] and used in this analysis as basis for the unfolding.

4.4.4 Paraboloid Fit and Track Resolution

Once a track candidate has been identified with any of the above described likelihood methods, the question remains about its geometrical resolution $(\delta_\theta, \delta_\phi)$. Let us assume that the best estimate for the track parameters is provided by a maximum likelihood $\mathcal{L}_{\max}$, and that the maximum value has been found in the space (θ, ϕ). We consider the set of parallel tracks, disregarding the point (x, y, z); this reduction simplifies considerably the problem. The negative logarithm $-\log \mathcal{L}$ is approximated with a Gaussian at the minimum. An ellipse is identified in the two dimensional space, so that $-\log \mathcal{L}$, constrained on the ellipse, has increased by $1/2$ with respect to the minimum value $-\log \mathcal{L}_{\max}$:

$$-\log \mathcal{L}_{\text{ellipse}} + \log \mathcal{L}_{\max} = \frac{1}{2}\,. \tag{4.21}$$

An analytic χ^2 minimisation provides the best paraboloid approximating $-\log \mathcal{L}$ at the minumum [67]. Writing the paraboloid in the parametric form, the problem reduces to the determination of a set of 7 parameters:

$$P : a + b_1\,\phi + b_2\theta + \frac{1}{2}(\phi, \theta)\, C\, (\phi, \theta)^T. \tag{4.22}$$

The three parameters a, b_1, b_2 are related with the position of the minimum; the matrix C contains the curvature. The errors on the resolution can be obtained by the coefficients $(C)_{ij}$, as the covariance matrix of the Gaussian approximation is the inverse of C.

$$\begin{aligned} \sigma_\phi^2 &= C_{11}^{-1} \\ \sigma_\theta^2 &= C_{22}^{-1} \\ \text{cov}(\phi, \theta) &= C_{12}^{-1}. \end{aligned} \tag{4.23}$$

In a reference frame where the matrix C is diagonal, the errors on the two parameters (θ, ϕ) can be read as the axes of the rotated ellipse. The geometrical average

$$S = \sqrt{\sigma_1 \cdot \sigma_2}\,, \tag{4.24}$$

representing the area of the ellipse, is used as an estimate of the track resolution.

Chapter 5

Event Selection

The data sample investigated in this analysis consists of atmospheric neutrino events recorded over the four year period 2000 - 2003, selected according to some quality requirements. The filtering criteria are established by comparing real data to Monte Carlo simulation, optimising the matching on a 20% of the data events[1]. The raw data were first elaborated and selected at Zeuthen. Selection criteria are applied both to detector stability and to the quality of the signal recorded, and in a second stage to the reconstructed track. Further advanced reconstruction algorithms and rejection criteria are developed and applied in Mainz to the Zeuthen filtered sample. As a last step, selection conditions are applied to some variables for the specific purpose of this analysis, which is to optimise the agreement between data and simulation and reject background with minimal signal loss.

5.1 Measured Data at Initial Level

Data are initially recorded by the AMANDA data acquisition system in F2K format and shipped North via airplane. The complete data sample from the years 2000-03, which will be investigated in this analysis, occupies about 8 TBytes on tape. It consists of about 10^9 events, of which the vast majority are atmospheric muon events and will be rejected as background during the selection and reconstruction process. F2K is ASCII format which has been described in section 2.6. The whole simulated data sample covering the four year time period analysed here contains about 8×10^5 events.

5.2 Zeuthen Selection and Reconstruction

Raw data of the years 2000-03 have been accurately selected and reconstructed in successive stages in Zeuthen with the SIEGLINDE software package [46].

[1] According to the AMANDA blindness policy, the analysis criteria are established basing on a 20% of the events. The rest is disclosed after the procedure has been approved.

In chapter 4 the reconstruction algorithms are described.
Firstly the raw data are processed with a general set of selection criteria based on detector stability and hit quality. In addition, whole files are rejected when they show unstable rates in the AMANDA monitoring system.

- Detector stability
  - exclusion of unclean data taking periods, including flare periods, detection maintenance periods, changes of the trigger conditions, and all possible alterations which could make data taking unstable.
  - exclusion of known defective optical modules, which are either not working or showing unstable noise rates.
  - selection of files after amplitude and geometry calibration (see 2.9). Data taken with uncertain calibration, on the other side, are disregarded.
- Hit quality
  - exclusion of the time over threshold values falling outside a window of 50 to 200 ns for electric cable connected modules and 5 ns for optical connected modules.
  - selection of the first hit in the case of multiple hit signals.
  - exclusion of topologically isolated hits, which are unlikely to belong to a track and may instead be a result of electrical noise.

Applying the different exclusion conditions can mean that the remaining hits for an event do not fulfill the trigger condition any longer. Such events will be rejected at this level. The recorded hits passing the conditions are processed with the first reconstruction algorithm. After every reconstruction, with the increasing complexity of the algorithms used, further selection conditions based on some quality parameters are applied to reject all possible sources of background.

Fit performed in Zeuthen

1. As mentioned in chapter 4, the easiest and least computer intensive algorithm is the direct walk reconstruction fit. This allows for a first rough estimate of the track direction. After the direct walk result, all the tracks with zenith $\theta < 70^\circ$ are rejected. The coordinate system of AMANDA labels $\theta = 0$ as a particle coming from the Southern direction, and we often refer to events from the Southern hemisphere as downgoing.

2. The second reconstruction fit is performed with the JAMS algorithm (4.4.1). Events identified as suspected double-muons are rejected. The

angular resolution provided by the direct walk fit is slightly improved with this second level. After the JAMS reconstruction, all events with zenith $\theta < 80^\circ$ are rejected.

3. At this level, all hits suspected of cross-talk[2] are rejected and the trigger condition is verified. Events that do not fulfil the trigger condition are rejected.

4. This considerable reduction of events allows likelihood-based reconstruction fits to be applied, more advanced from the point of view of computing time and complexity. At first, the JAMS reconstructed track is assumed as starting hypothesis and the Pandel function is applied to evaluate the expected photon arrival time at each optical module. The iterative likelihood is computed and maximised with a 32-fold iterative process.
   The likelihood algorithm can reconstruct a track with a slightly different zenith respect to the JAMS fit; again all tracks with $\theta < 80^\circ$ are rejected.

5. Finally, the possibility of a misreconstructed down-going event is investigated evaluating the likelihood of a down-going track according to the Bayes reconstruction fit. Considering the up-going track from the JAMS result, the comparison with a possible down-going track is performed with a 64-fold iterative likelihood. All tracks which result in a maximum likelihood as down-going are rejected.

The Zeuthen selection provides a final data sample containing about $7 \cdot 10^6$ events. The exact values are shown in table 5.1.
This sample has been used as a basis for a large number of AMANDA analyses [71, 72, 73, 74].

Raw data	$7,14 \times 10^9$
Level 1 $\theta_{\text{direct walk}} > 70$	260×10^6
Level 2 $\theta_{\text{JAMS}} > 80$	28×10^6
Level 5 $\theta_{\text{Pandel}} > 80$	$7,85 \times 10^6$

Table 5.1: Number of events after each step of the Zeuthen selection.

5.3 Mainz Selection and Reconstruction

The data sample resulting from the Zeuthen selection has undergone further processing in Mainz to other reconstruction levels. Stricter selection conditions

[2] Cross-talk is an electronic artefact. See section 4.2 for an explanation.

have been established, seen the high computing time of the reconstruction algorithms used.

1. All tracks with $\theta < 90^\circ$ from the 32-folded Bayesian likelihood are rejected. This restricts the data sample to events below the horizon.

2. A fit algorithm based on the hit probability is applied. The 10-fold likelihood is evaluated and the angular resolution of the reconstructed track is further refined. After this level a hit cleaning is applied to those hits having a residual time that exceeds the expected value by $3\,\sigma$.

3. The Pandel function is applied to evaluate the expected photon arrival times with reference to the high resolution track obtained from the last reconstruction step. After this level the residual time condition is checked and events not fulfilling the condition are rejected.

The data sample obtained after the Mainz reconstruction is further reduced by about a factor of 10 with respect to the Zeuthen sample.

Raw data	$7,14 \times 10^9$
Zeuthen sample	$7,85 \times 10^6$
Mainz sample	$8,28 \times 10^5$

Table 5.2: Number of events after each selection step.

5.4 Variables Used in the Final Selection

A few variables are considered in this analysis to check data quality and compare data with simulation. The only quantity directly recorded is the number of hit channels, all the others depend on the reconstruction fit. Unless differently specified, we refer to the $P_{\mathrm{hit}}P_{\mathrm{no-hit}}$ fit described in point (2) of the previous paragraph. In the following paragraph, we describe the conditions applied to those variables to reject background.

1. The zenith angle, or declination angle of the track, with respect to a coordinate system where 90° is the horizon direction, and 180° is the North Pole.

2. The number of hit channels N_{ch} contributing to the signal.

3. The smoothness, which is a measure of the uniformity in the distribution of hits along the track. We consider the hits within 50 m from the track and with a low residual time -25 ns $< t < 75$ ns. For each optical module within the distance l, the hit probability is evaluated as a function of the distance. The expected number of hits is then compared with the observed number, as a function of the position along the track (see figure

5.1). The observed and expected number of hits, respectively, are given by

$$N(l) = \sum_i \theta\,(l - l_i) \tag{5.1}$$

$$N_{\text{expected}}(l) = \sum_j \mathcal{P}(d_j)\,\theta\,(l - l_j) \tag{5.2}$$

with i running over hits, and j over the optical modules within the distance d. $\mathcal{P}(d_j)$ is the probability that module j is hit. The smoothness is defined as

$$S = \frac{\text{sgn}\,[N(l_{\max}) - N_{\text{expected}}(l_{\max})]}{N(\infty)} \max_l |N(l) - N_{\text{expected}}(l)| \tag{5.3}$$

By definition $-1 < S < +1$. For a given track hypothesis, a value $S \to +1$ indicates that hits are missing. $S \to -1$ instead means that unexpected hits appear in optical modules too far away from the track. In all cases, $S \neq 0$ indicates a possible misreconstruction.

4. The likelihood difference between the considered track and a track coming from the opposite direction with same angle. Figure 4.5 illustrates this case. When the likelihoods of the two tracks are too close, a misreconstructed event is difficult to identify (see figure 5.3).

5. The angle ψ between two tracks hypotheses[3], results of two subsequent fits of the same event, whose geometry is illustrated in figure 5.2. Each track is identified by zenith and azimuth (θ, ϕ), so if e_1 and e_2 are the two versors of the tracks

$$\begin{aligned} t_1 &: e_1(\sin\theta_1 \cos\phi_1, \sin\theta_1 \sin\phi_1, \cos\theta_1) \\ t_2 &: e_2(\sin\theta_2 \cos\phi_2, \sin\theta_2 \sin\phi_2, \cos\theta_2). \end{aligned} \tag{5.4}$$

the angle ψ can be determined from the relation $t_1 \cdot t_2 = \cos\psi$

$$\cos\psi = \sin\theta_1 \sin\theta_2 \cos(\Delta\phi) + \cos\theta_1 \cos\theta_2 \tag{5.5}$$

ψ lies in the plane individuated by the two versors. A large value of this angle indicates that the two subsequent fits strongly disagree, rather than represent an adjustment of each other.

6. The angular resolution of the track. The negative logarithm of the likelihood, which is a function of the track parameters (θ, ϕ), shows a minimum in correspondence of the most likely track hypothesis. The likelihood function is approximated with a second degree polynomial at the minimum, whose parameters are determined with a least square fit in this two-dimensional parameter space. The resolution is defined from the paraboloid fit errors σ_1 and σ_2 (see expression (4.24)).

[3] often called "space angle" in AMANDA

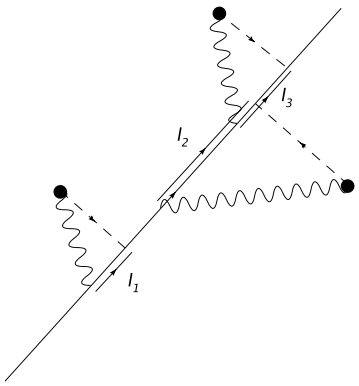

Figure 5.1: Projection of the photon distances to each optical module hit along the direction of the track.

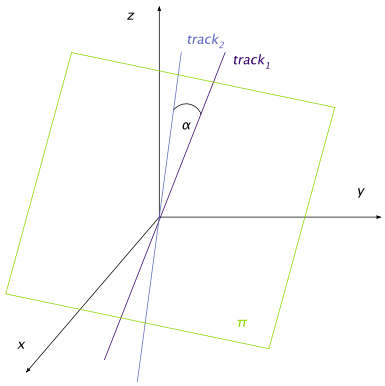

Figure 5.2: The space angle between two tracks, defined on the plane individuated by the two versors. As the two tracks are resulting from two different fits of the same event, the angle should be small.

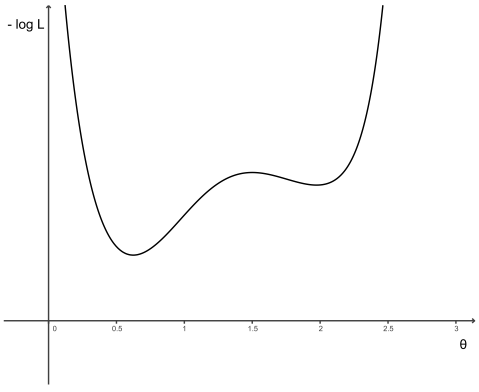

Figure 5.3: The negative likelihood logarithm can have a local minimum not far from the absolute one, in correspondence of a down-going track. When the two minima are not clearly resolved, the track can be misreconstructed

5.5 Final Selection

Dedicated selection conditions have been applied to some parameters of the track to refine our data sample. A sample of 20% of our measured data is compared with a simulated sample to establish the strength of the rejection condition and check the quality of the selected events. The variables that

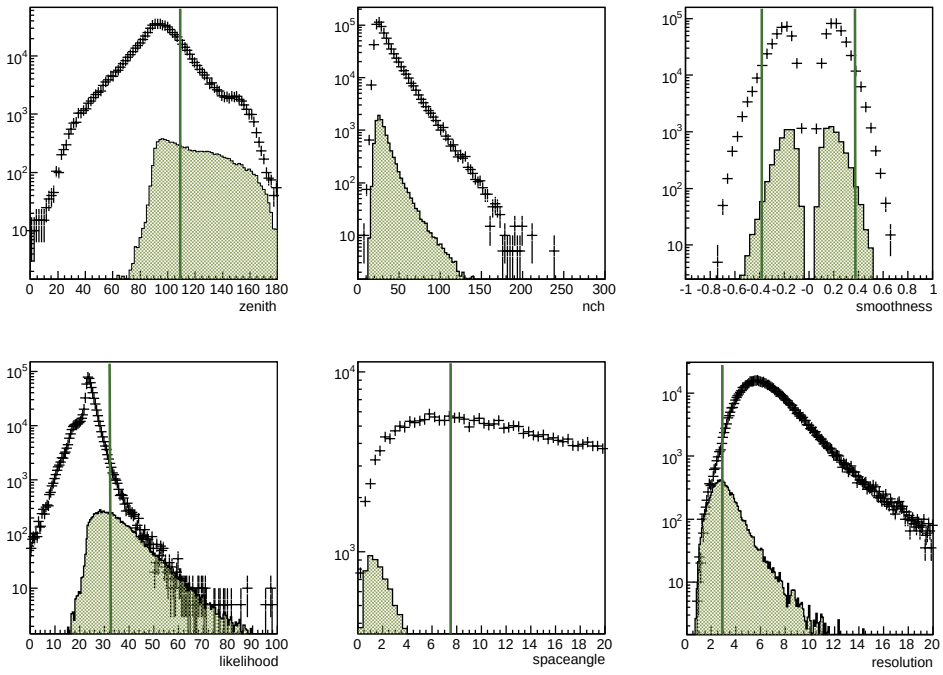

Figure 5.4: Distributions of the six variables considered for the selection, after the Mainz L6 filtering. Monte Carlo simulation is represented by a filled histogram. Data points are obtained by $5 \cdot 20\%$ of the total sample. Vertical lines show the threshold value for events to pass the final selection.

have been compared between data and Monte Carlo simulations are described in paragraph 5.4. The zenith angle distribution (figure 5.4 plot 1) allows for an initial, simple rejection of tracks coming from the Northern direction. As shown in the figure, background is still largely present in the sample. No condition is applied to the variable N_{ch}, whose distribution is anyway used to look at the matching between data and Monte Carlo (plot 2). The condition on the smoothness (plot 3) is meant to reject tracks whose reconstruction does not optimally match the hits pattern, as either channels are missing, or signals are spread far from the track region. The likelihood difference (plot 4) allows for rejection of tracks which could be misreconstructed as upgoing, although originated by cosmic ray muons. Here the likelihood difference is calculated between a down-going Pandel fit and upgoing Bayesian. Small

values indicate that there is no clear distinction between the up- and down-going reconstruction, hence it is prudent to dismiss the track. The space angle (plot 5) is considered in which it represents a measure of the goodness of the fit. A track showing no reconstruction ambiguity has small space angle between different fits. The angular resolution of the track (plot 6) indicates the precision of the fit result. Background identification based on zenith angle rejection is more efficient by good resoluted tracks.
The sample before the final selection is composed of $7.3{\cdot}10^5$ data events, and about 10^4 simulated events (figure 5.4). A first set of conditions (A) for refining the sample are set to:

(A)

zenith $> 110\,^\circ$
smoothness > -0.4
likelihood difference > 25
space angle $< 15\,^\circ$
median resolution $< 4.5\,^\circ$

After this selection level the remaining simulated sample is composed of 7145 measured data events, and 5219 simulated events[4]. These results are shown in figure 5.5.
Background is still present in the sample, as it is evident from the absolute normalisation, hence the strength of the conditions has been tightened (B) to the following values

(B)

zenith $> 110\,^\circ$
smoothness > -0.375
likelihood difference > 32.5
space angle $< 7.5\,^\circ$
median resolution $< 3\,^\circ$

Once the conditions of level (B) are applied, the data sample is composed of 2640 events and the simulated sample of 3194. Those results are shown in figure 5.6.
Although the agreement between data and Monte Carlo at level (B) is satisfactory, it can be refined by choosing a variable threshold on some variables, so that the strength of the selection is different in the high and low energy regions. This would also allow less signal suppression in the data. The selection is further optimised substituting the fix condition on the two variables median resolution and likelihood difference with a condition which is function of zenith and number of channels. The values used for the selection are illustrated in figure 5.7 and have been optimised in a previous analysis [74]. In particular,

[4]Simulated events are weighted, hence their absolute number does not correspond with the integral of the distribution.

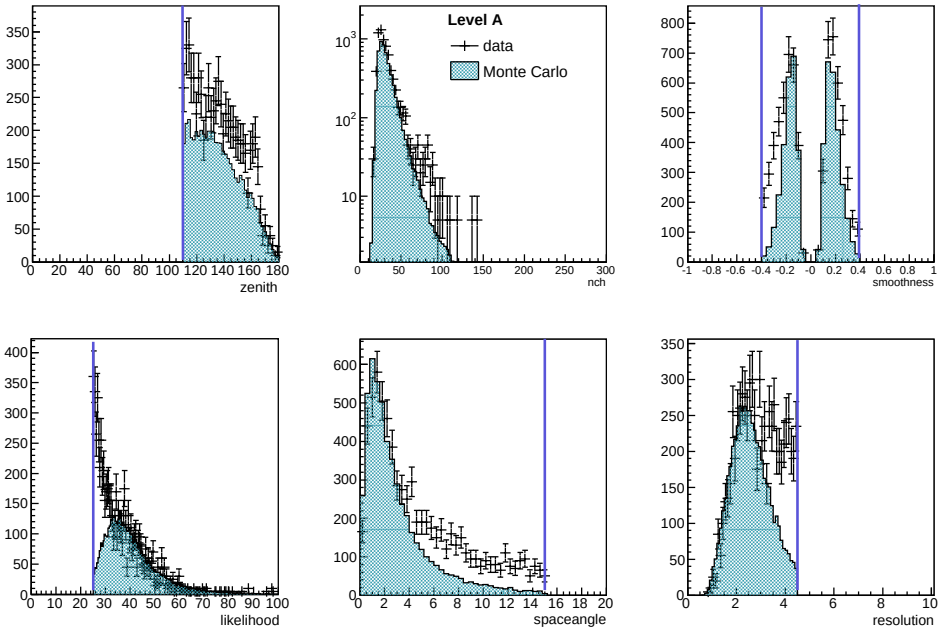

Figure 5.5: The six variables investigated after selection level (A); the blue lines represent the selection value threshold. Results from Monte Carlo simulations are not normalised to data. Data events considered are 20% of the total sample, multiplied by a factor 5.

the dependence of the condition on the number of hits ensures that events with high hit multiplicity are selected with looser conditions. It is crucial for this analysis not to suppress signal in the high energy region, as the contribution of neutrinos from charm becomes important around one TeV, where statistics are low according to the expected flux prediction. This last case (C) optimises the agreement between simulation and data, and simultaneously ensures minimal signal loss, and hence it will be used in this analysis. To summarise, the conditions for an event to pass the final selection are

(C)

zenith $> 110\,^\circ$
smoothness > -0.375
likelihood difference $> f_a(\theta, N_{\mathrm{ch}})$ (see fig. 5.7 [a])
space angle $< 7.5\,^\circ$
median resolution $< f_b(\theta, N_{\mathrm{ch}})$ (see fig. 5.7 [b])

After the selection level (C), the data sample is composed of 3395 atmospheric neutrino events, and 3974 simulated events. An overview of the six variables analysed is shown in figures 5.8 and 5.9. The normalisation of the Monte Carlo

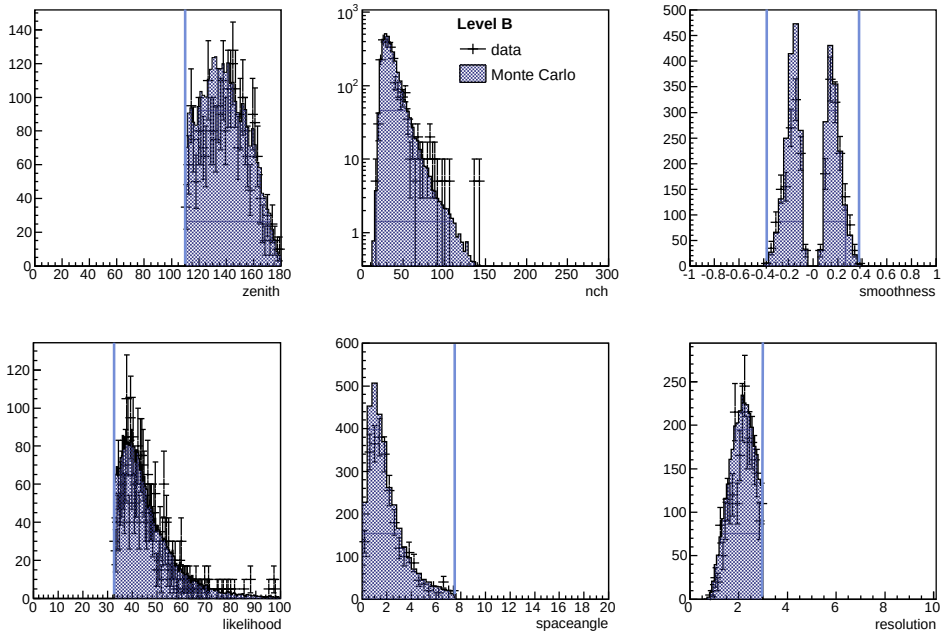

Figure 5.6: The six variables investigated after selection level (B). Results from Monte Carlo simulations are not normalised to data.

distribution is affected by small variation due to the flux model applied. In all the plots shown is this chapter, the weight for simulated events is calculated with respect to the Lipari model [91]. The variable N_{hits} is of particular interest as strongly related to the energy of the event, hence no condition is applied on its distribution. In chapter 8, this variable will play an essential role in the unfolding and reconstruction of neutrino energy.

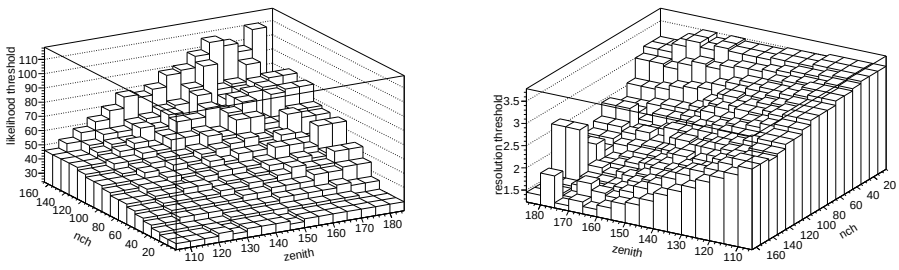

[a] [b]

Figure 5.7: threshold for likelihood difference [a] and median resolution [b].

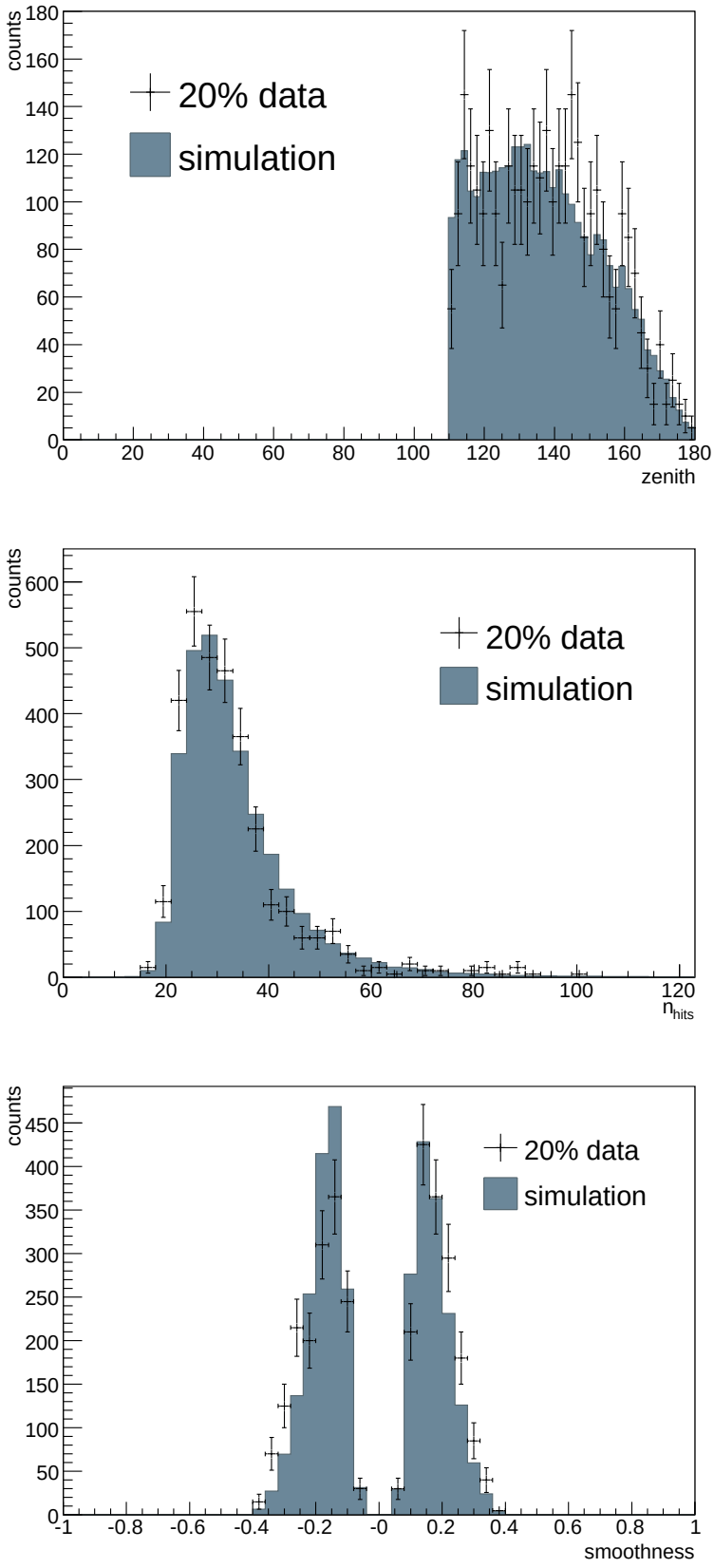

Figure 5.8: Comparison between data and simulation after the last selection level. The variables zenith, number of channels and smoothness are shown.

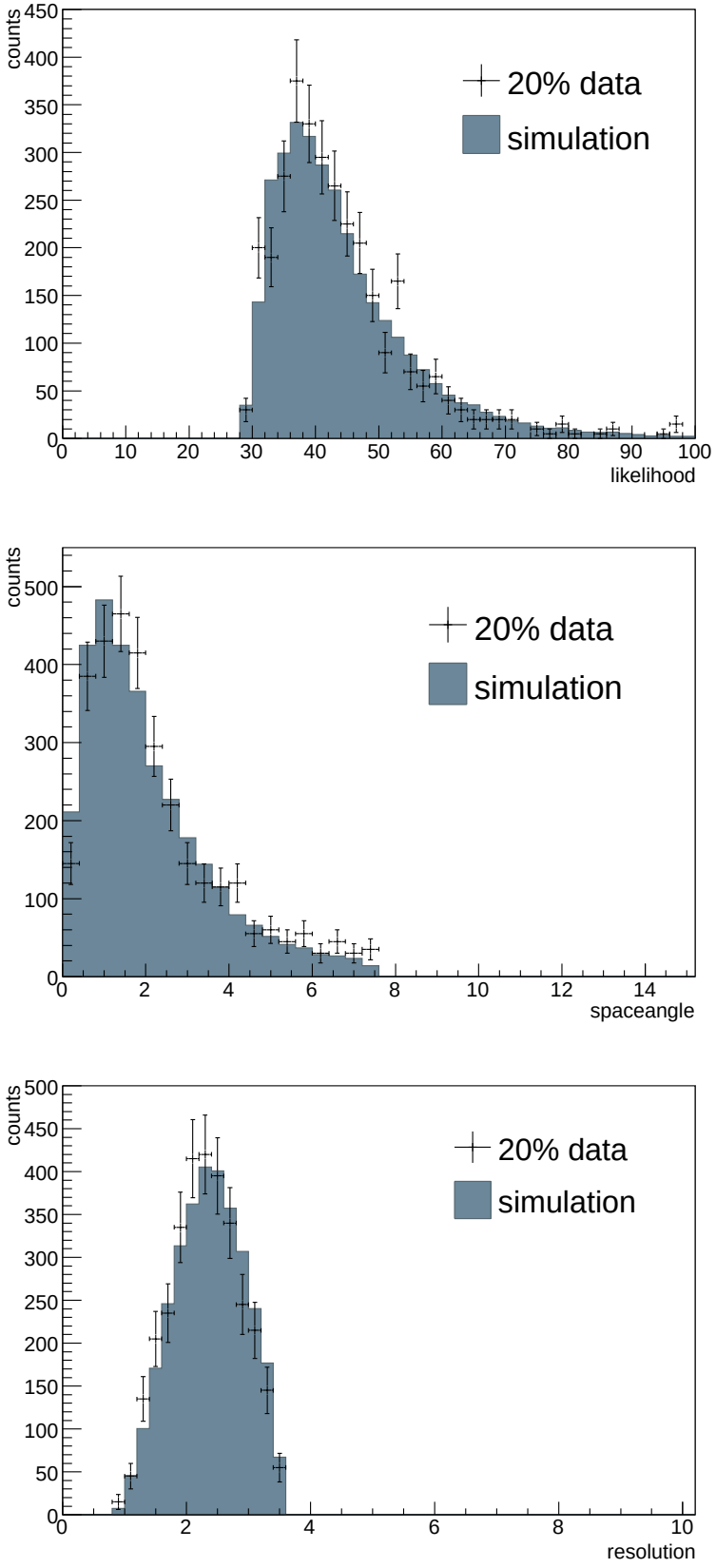

Figure 5.9: Comparison between data and simulation after the last selection level. The variables zenith, number of channels and smoothness are shown.

Chapter 6

Detector Efficiency and Effective Area

A way to determine the acceptance of the detector is to count how many Cherenkov photons are missed when a charged particle traverses the detector, as a function of the distance of the photomultiplier from the track. Ice has low absorption, but many of the recorded photons have been scattered before reaching one photomultiplier. This affects both arrival time and direction, making the reconstruction challenging. The comparison of data with simulations assuming various efficiencies allows us to extrapolate and estimate the detector acceptance. Moreover, the acceptance is a function of the arrival angle of the photons. This last aspect is to be ascribed to the geometry of the AMANDA optical modules. In the final paragraph, the neutrino effective area is evaluated as a function of the energy and zenith angle of the lepton track.

6.1 Hit Probability

A charged particle traversing the ice emits Cherenkov photons along its path with an angle θ_C respect to the trajectory direction. Light is detected by a lattice of photomultipliers around the track. For each photomultiplier we evaluate the photon distance d, defined as the distance that a photon has to travel to reach unscattered the position of the photomultiplier (see fig. 6.1). The information about the photon distance is purely geometrical and depends on the declination angle of the track only. Each track is reconstructed from a set of hits $\mathcal{H}$, selected as described in chapter 4. For each optical module which has been hit, we evaluate the photon distance from the track, as shown in figure 6.4 and 6.5. The first shows the distribution of the distance of each track from each optical module, up to a value of 50 meters. The second one shows the number of photomultipliers which did actually see *at least one* hit, among the ones lying within the distance d from the track. In figure 6.2, the situation for one single track is illustrated. The coloured numbers indicate

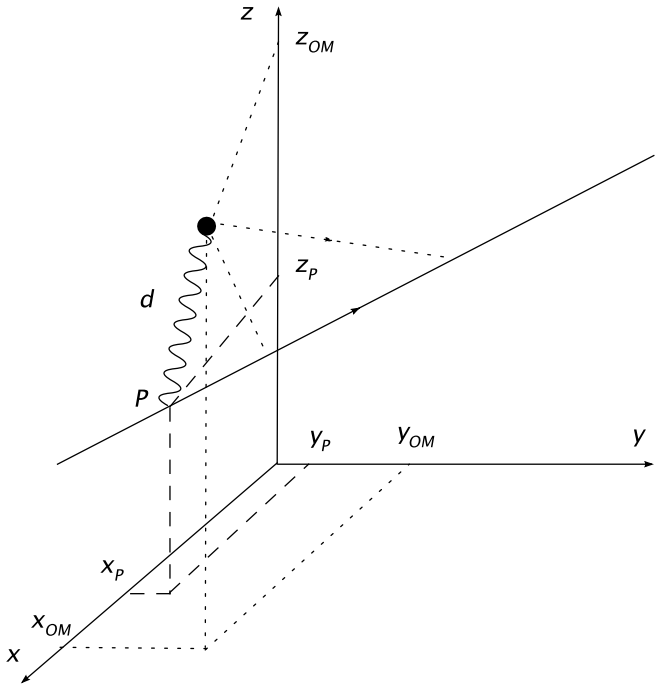

Figure 6.1: The geometrical definition of photon distance d, from the track to the photomultiplier.

the photomultiplier detecting light which passed the trigger condition. Such a pattern is the input for the reconstruction chain. The information about the set of hit channels is stored in the F2K files, and is later no longer recorded, after the event is identified as reconstructed track. This makes it necessary to use the original F2K files for the analysis described in this chapter. An example of F2K is shown in figure 2.14; it contains time and position of each photomultiplier hit after hit cleaning. One example of reconstructed track is shown in figure 6.3, where the coloured numbers indicate the hit channels laying within a photon distance of 50 meters from the track. If we name N_0 the number of photomultipliers within a certain distance d, and N_H the number of photomultipliers within the distance d detecting a light signal, the efficiency is defined through the hit probability as

$$\epsilon = \frac{N_H}{N_0}. \tag{6.1}$$

The distributions of the variables N_H and N_0 are shown in figures 6.4 and 6.5. In the simulated data it is possible to vary the efficiency of the optical modules with respect with the nominal value. We use here a $\pm 30\%$ variation in the photon detection efficiency of the simulated data. Figure 6.6 shows the variable ϵ defined in expression (6.1) as a function of the photon distance, for data and three Monte Carlo simulations with acceptance $70\%, 100\%, 130\%$.

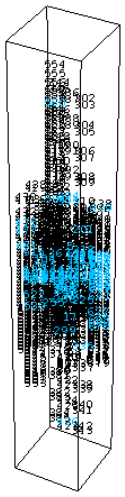

Figure 6.2: A pattern to be reconstructed as a track. The hit optical modules (coloured) embedded in the whole detector.

The binning is in 25 bins of the width of 2 m each.

6.2 Determination of the Detector Efficiency

Comparing the data distribution of hit optical modules with the variable acceptance Monte Carlo, it is possible to extrapolate the photon detection efficiency in the data. To this purpose, we plot the efficiency obtained for each simulated data sample (unbinned) and interpolate with an appropriate fit between the three points. We present here the result of polynomial fits of degree 1 and 2 (see figure 6.7). To evaluate the detector efficiency we choose to compare the measured data with the second degree polynomial $P(x) = ax^2 + bx + c$ interpolating the three varied efficiencies Monte Carlo. The least squares method gives as a best estimate

$$\begin{aligned} a &= 1.3 \cdot 10^{-5} \\ b &= 0.004 \\ c &= 0.166 \end{aligned} \tag{6.2}$$

Our data point has the value $d = 0.438$, leading to the crossing point with the polynomial curve

$$ax^2 + bx + c = d \Rightarrow x = 94.6$$

Our estimate of the detector efficiency is then

$$\epsilon = 95\% \tag{6.3}$$

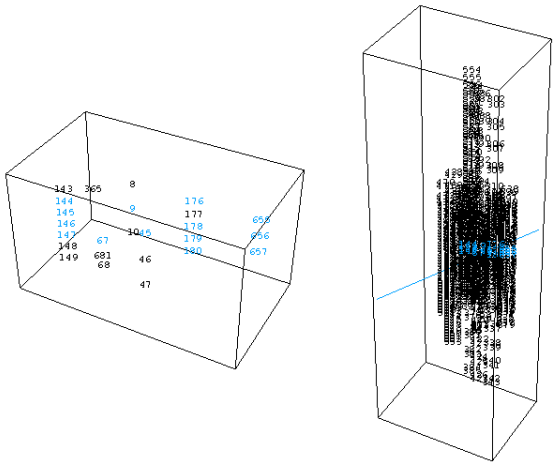

Figure 6.3: The hit optical modules lying within 50 meters from the track, and the track line reconstructed and embedded in the complete detector view.

This result is compatible with the value previously obtained in other analyses, see for instance [73] and [74].

6.3 Expected Number of Photons

We assume that the hit probability is Poisson distributed. The Poisson statistics describes the probability for a number of events occurring with a known average rate in a defined time interval, independently of the time since the last event. If we name P_{hit} the hit probability, r the distance[1] of each optical module from the track, $N(r)$ the number of hits at distance r, and $\lambda(r)$ the average expected number of photons at distance r, we have

$$P_{\text{hit}}(\lambda(r), N(r)) = \frac{\lambda(r)^{N(r)} e^{-\lambda(r)}}{N(r)!}. \tag{6.4}$$

Having previously defined the hit probability (expression 6.1), we consider the probability to see no photons $P_{\text{no hit}} = 1 - P_{\text{hit}}$ at distance r. If the hit probability is Poissonian distributed, the substitution $N = 0$ in equation 6.4 yields

$$P_{\text{not hit}} = P(0, \lambda) = e^{-\lambda} \tag{6.5}$$

We obtain a relation between the hit probability investigated in the previous part and the expected number of photons λ. Both functions of the distance r

$$P_{\text{hit}}(r) = 1 - e^{-\lambda(r)} \tag{6.6}$$

[1] As often in this chapter, we refer to the distance traveled by photons as illustrated in figure 6.1.

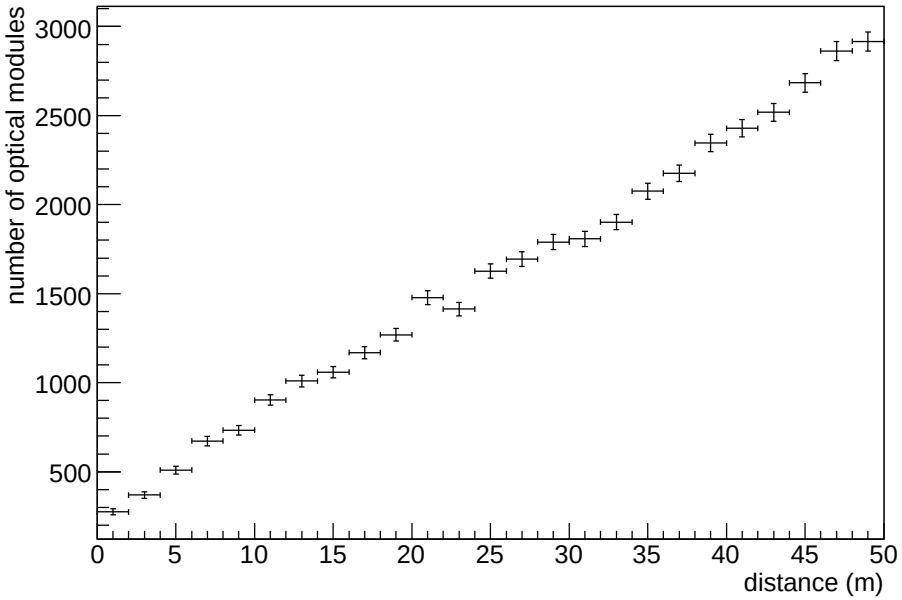

Figure 6.4: Histogram of the variable N_0 (number of optical modules function of the photon distance).

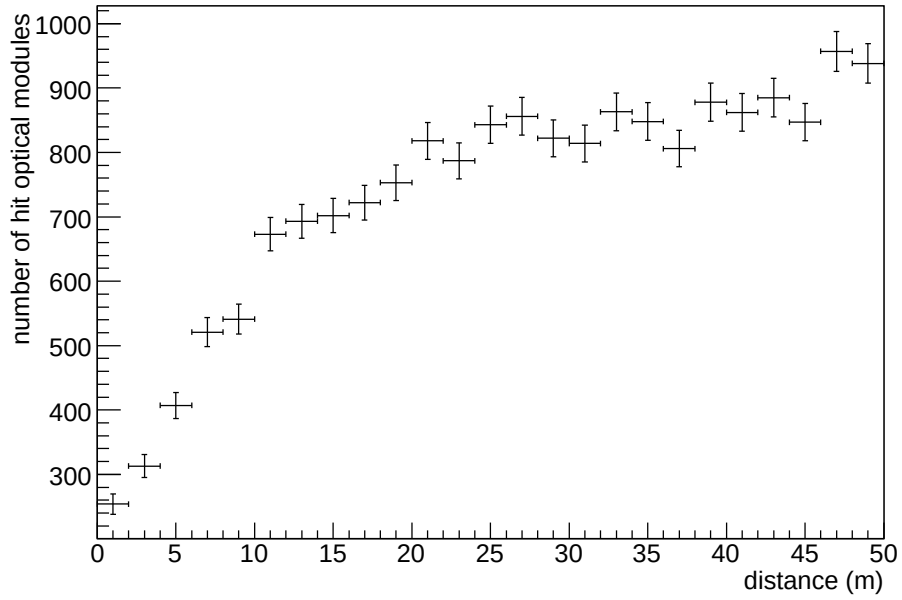

Figure 6.5: Histogram of the variable N_H (hit optical modules as function of the photon distance).

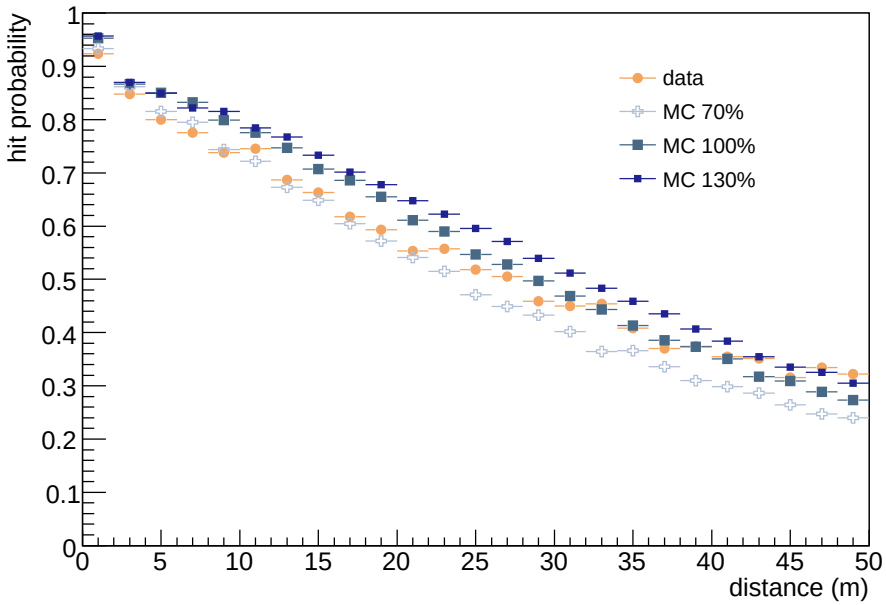

Figure 6.6: The hit probability for the complete data set. Here data are compared with a simulated sample with varied efficiency, namely $100 \pm 30\%$. The hit probability is obtained as the ratio between the number of hit channels over the number of total channel laying at a certain distance from a track. The result shown here accounts for all the tracks in the 4 years data sample, up to a distance of 50 meters.

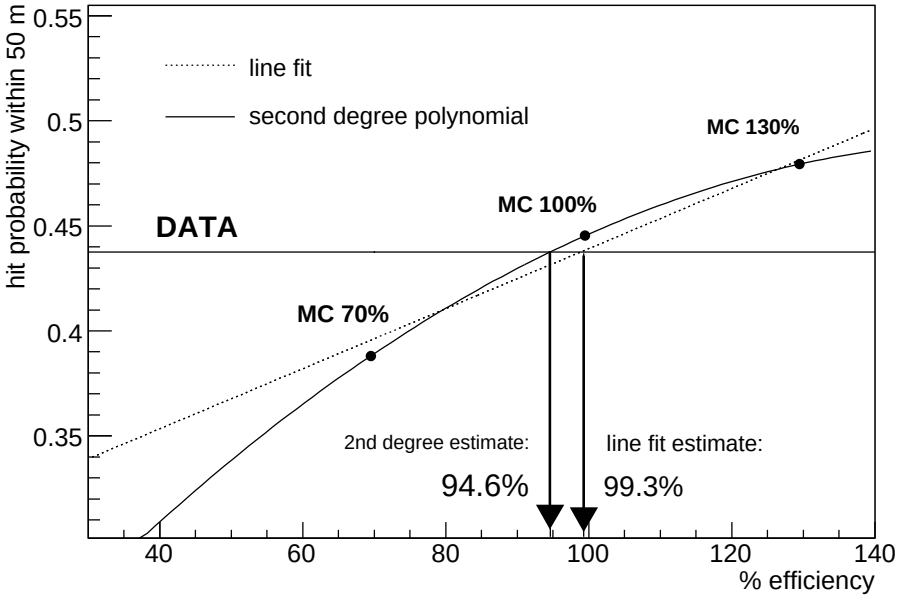

Figure 6.7: Interpolation of the simulated data with varied efficiency. Both a linear fit and a second degree polynomial fit are shown. The second degree polynomial fit is chosen. The data point crosses the curve at $\varepsilon = 95\%$

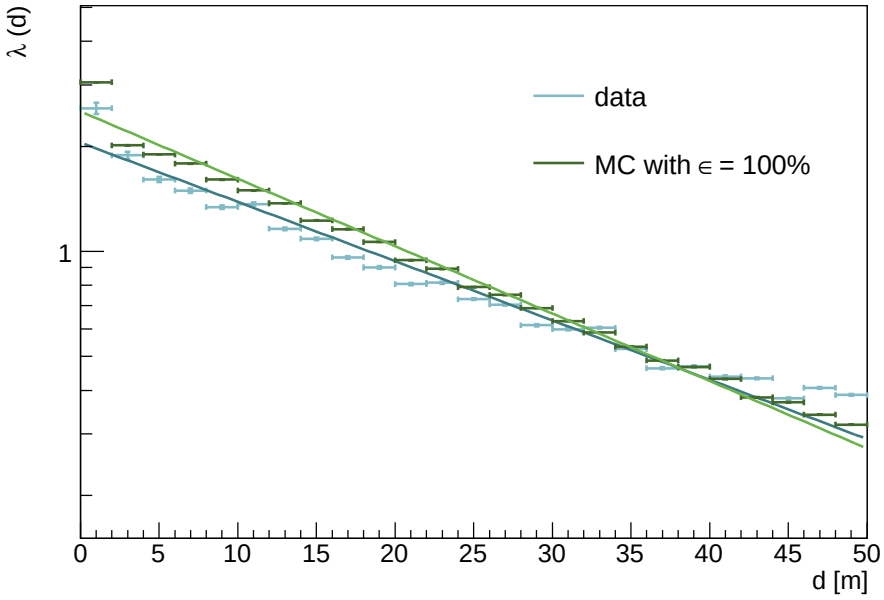

Figure 6.8: Data and Monte Carlo with 100% efficiency plotted. $\log(\lambda)$ is interpolated with $a + br$, with r being the distance travelled by photons.

We assume the functional form for λ to be linear in the distance r with general coefficients a, b to be obtained with a fit

$$\lambda = a + b\, r, \tag{6.7}$$

with r being the photon distance from the optical module. We interpolate the not-hit probability to fit this parameterised curve. The fit is shown in figure 6.8. The efficiencies are plotted in figure 6.8 respectively for data and simulation with 100% acceptance.

6.4 Errors on Efficiencies

The efficiency ϵ is generally defined as the ratio between the number of the events which pass the count N_p out of N_0 candidates, and the total counts N_0

$$\epsilon = \frac{N_p}{N_0}. \tag{6.8}$$

The measure of N_p events out of a sample of size N_0 is a binomial process [69] whose probability is expressed by

$$\mathcal{P}(N_p, \epsilon, N_0) = \left(\begin{array}{c} N_0 \\ N_p \end{array} \right) \epsilon^{N_p} (1-\epsilon)^{N_0}\,, \tag{6.9}$$

with mean value $\overline{N}_p = \epsilon N_0$ and variance $\sigma^2_{N_p} = n\epsilon(1-\epsilon)$. According to the definition of efficiency given in equation (6.8), the error on ϵ is

$$\sigma^2_\epsilon = \frac{N_p(N_0 - N_p)}{N_0^3} \tag{6.10}$$

Note that he two quantities N_p and N_0 are correlated, hence we cannot apply the usual error propagation relation and have to take into account the covariance term $\sigma_{N_f}\sigma_{N_p}$. The resulting statistical error obtained with the formula of expression (6.10) is very small. As we have only three measurements for the simulated data, however, there is a clear uncertainty in the choice of the fit. We have chosen for the measured efficiency

$$\epsilon = (95 \pm 5)\% \tag{6.11}$$

6.5 Detector Effective Area

The flux of produced neutrinos is related to the flux of detected lepton events through the *effective area*. This quantity accounts for both the neutrino charged current cross section and for the finite geometry of the detector. To detect a neutrino, a charged current scattering has to occur in the ice in the vicinity of the detector and originate a lepton. It is useful to ask how many neutrinos we expect in the instrumented volume, and how many do we actually see. The first information is provided by the neutrino flux Φ_ν, convoluted with the charge current scattering cross section, the detector geometry and efficiency. The second information consists of our observed data. This relation is expressed in equation 6.12.

$$N_{\text{obs}} = \Phi_\nu \cdot A_{\text{eff}} \cdot t \tag{6.12}$$

The quantity A_{eff} is the effective area and includes both the detector efficiency and the cross section $\sigma(\nu N \to lX)$; t is the time of data taking. We can also refer to the rates

$$R_{\text{obs}} = \frac{N_{\text{obs}}}{t} \qquad R_{\text{true}} = \frac{N_{\text{true}}}{t} \tag{6.13}$$

If we take into account the detector efficiency, namely the ratio $R_{\text{obs}}/R_{\text{true}}$, the measured rate of events can be expressed as

$$R_{\text{obs}} = \Phi_\nu \, \sigma \, n \int_V \epsilon \, dV \,, \tag{6.14}$$

where n is the particle density and V the detector volume. In the case where ϵ is constant, this expression reduces to $\epsilon \, R_{\text{true}}$. The effective area is then written as

$$A_{\text{eff}} = \sigma \, n \int_V \epsilon \, dV. \tag{6.15}$$

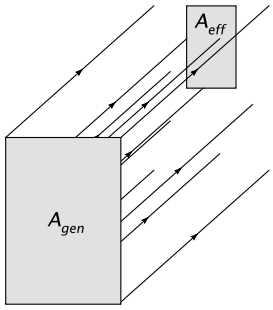

Figure 6.9: The relation between true and observed number of events is the ratio between the generation area and the effective area.

When referring to a simulated data sample, the true number of events is the generated amount of events on the Earth surface, and the following relation holds

$$\frac{A_{\text{eff}}}{A_{\text{true}}} = \frac{N_{\text{obs}}}{N_{\text{true}}} \tag{6.16}$$

The neutrino effective area represents the area of an ideal telescope (100% efficiency) detecting the same number of events as our detector sees, given the same number of starting (generated) events. In other words it represents the area of a telescope having its finite geometry as a unique cause of loss.
In analogy, the effective volume represents the volume of an ideal detector observing the same number of events N_{obs} as our detector sees:

$$V_{\text{eff}} = \int_V \epsilon \, dV = V_{\text{true}} \frac{N_{\text{obs}}}{N_{\text{true}}} \quad . \tag{6.17}$$

Whilst the neutrino effective volume coincides with the muon effective volume, the two effective areas differ. This is due to the fact that the two expected fluxes differ by a factor proportional to the cross-section $\sigma(\nu \to \mu)$

$$\Phi_\mu = \Phi_\nu \, \sigma \, n \, \langle r_\mu \rangle \tag{6.18}$$

with n being the particle density and $\langle r_\mu \rangle$ the average muon free path. To identify the rate of observed muons as a function of the expected muon flux and the muon effective area, we obtain

$$R^\mu_{\text{obs}} = \Phi_\mu \, A^\mu_{\text{eff}} = \Phi_\mu \frac{1}{\langle r_\mu \rangle} \int_V \epsilon \, dV \tag{6.19}$$

The following geometrical relation holds between muon effective area and effective volume

$$V^\mu_{\text{eff}} = \langle r_\mu \rangle \, A^\mu_{\text{eff}}. \tag{6.20}$$

We have estimated the detector effective area comparing the two quantities

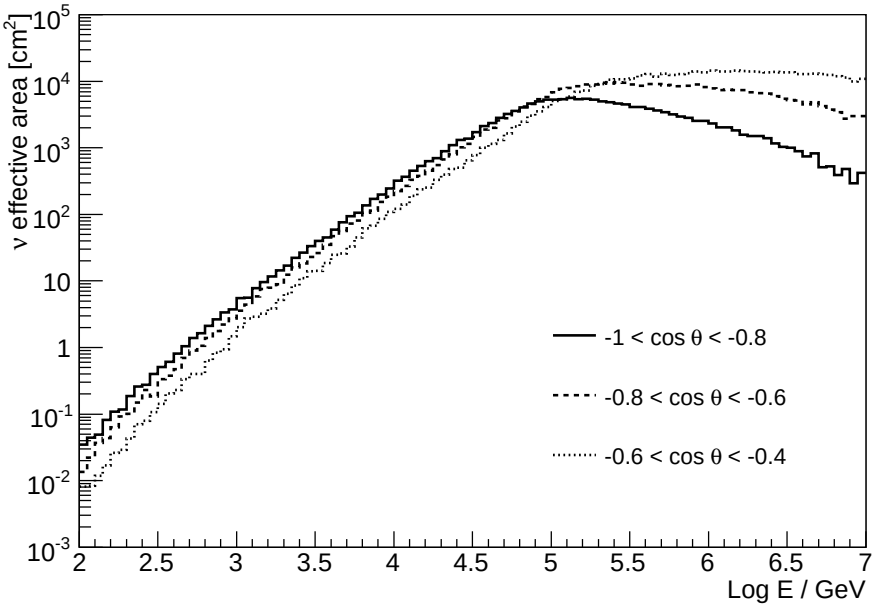

Figure 6.10: The neutrino effective area, as a function of the neutrino energy, for different values of the zenith angle θ.

- N_{obs}, integral of the true energy distribution of a simulated sample, shown in figure 6.11
- Φ_ν, expected flux according to a model prediction, shown in figure 6.12

The predicted flux of neutrino events has been propagating through the detector over a period of 807 days. This considered, we make a distinction between declination arrival angles, as the detector geometry gives different responses in efficiency to vertical or horizontal tracks. The resulting effective area, as a function of the neutrino energy and for different declination bins, is shown in figure 6.10. It will serve in chapter 8 to reconstruct the flux of *observed* events, from the measured counts N_{obs} of a real data sample.

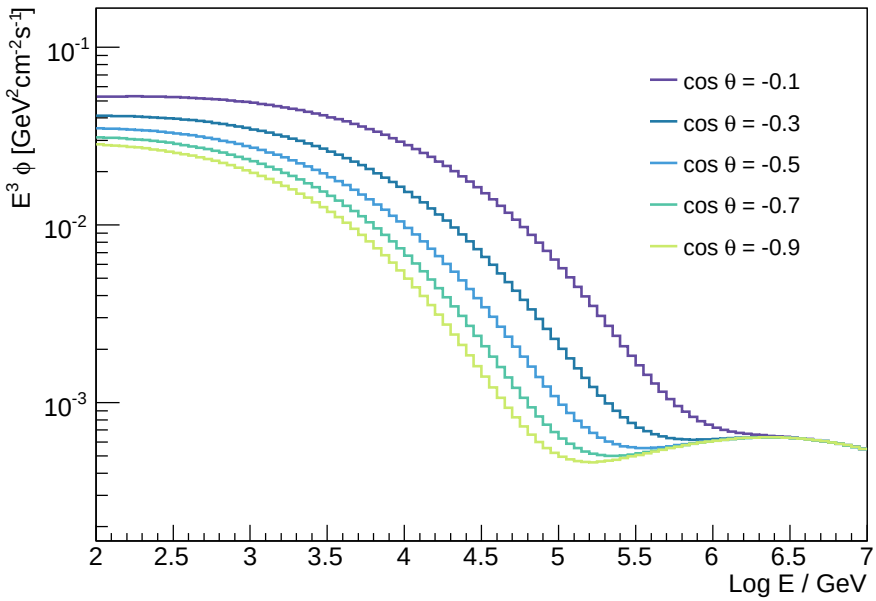

Figure 6.11: Neutrino flux, in different bins according to the zenith angle θ of arrival of the particle.

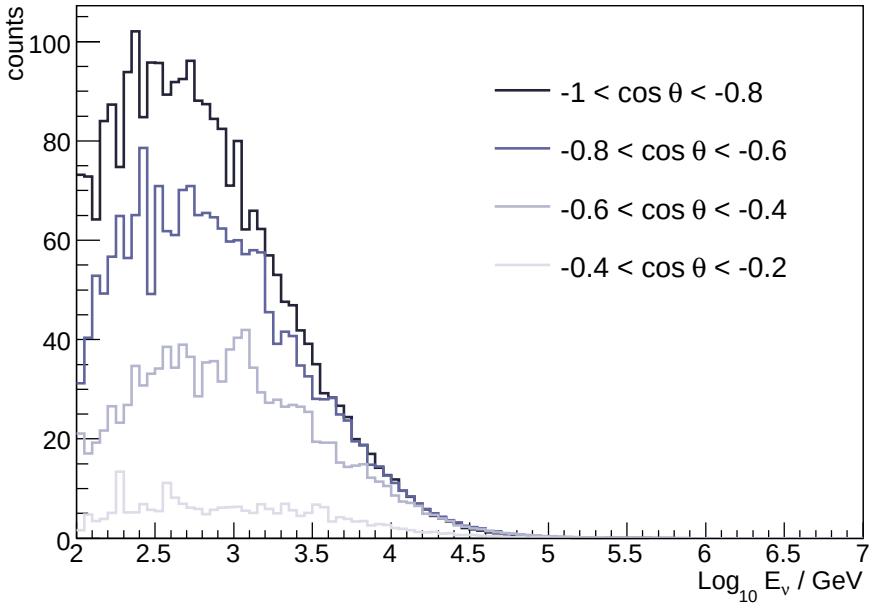

Figure 6.12: True neutrino energy in different bins according to the zenith angle.

Chapter 7

The Unfolding Problem

Let us suppose we travel around Europe and take a look at what people are reading on the train. We have some statistics from bookshops in different countries concerning the amount of copies sold of some literary genres, let's say detective stories, poetry and dramatic literature. Most of the British read detective stories, while the French prefer poetry and the Russians dramatic pieces, with some exceptions. We take note of this information, put it in our pocket and board a train. Travelling around we don't ask anyone for their nationality, but we throw a glance on their reading. After a few months we build a three class histogram stating: how many British, French and Russians did we meet?

Two remarks are in order: first, there is no possibility of defining a mathematical function "literary taste (nationality)". Second, we believe in our bookshop quest, allowing for some limited fluctuations from the expected distribution and rejecting large fluctuations as unphysical. If our statistics from the bookshop is sufficiently large, this bias will be negligible.

Unfolding is a simple problem to state with a fairly complicated solution.

7.1 The Unfolding Problem

Let us suppose we want to investigate a certain physical quantity x with its statistical distribution $f(x)$. Due to the fact we are using a real detector, the following points should be taken into account:

1. The variable x is not directly accessible with a measurement, but a quantity y related to it is available.

2. Limited acceptance: the probability of measuring each event is smaller than 1. This will result in a difference between the integrals of the true and measured distributions.

3. Finite resolution: the precision of a measurement is limited. If the result is in the form of a binned distribution, values in a certain bin of the true

distribution could contribute to another bin of the measured distribution. In general, a smearing or shift in the measured distribution $g(x)$ can occur.

4. The functional relation $y = h(x)$ is analytically unknown. If this is the case, the only information about the true variable and its distribution comes from a simulated data sample, having a model of the source as initial assumption.

Let us denote the probability density functions of the true variable x and unfolded variable y as $f(x)$ and $g(y)$ respectively. This kind of problem has the general solution

$$g(y) = \int A(x,y)f(x)dx + b(y) \tag{7.1}$$

where $A(x,y)$ represents the detector effect and $b(y)$ an arbitrary background parameterisation.

Def. *Unfolding* is the inverse problem of solving for $f(x)$ from $g(y)$.

The problem of solving for $f(x)$ is a so called *ill posed problem*, because of its non-stable, rapidly oscillating behaviour, meaning that small variations in the input variable can result in large changes in the solution. In the general case, a solution of the unfolding problem does not exist. If the unfolding process is the functional f connecting objects of a space A (true variables) with objects of an image space B (measured variables), such a function has the property

$$Ker\{f\} \neq 0.$$

The true and measured distributions, whose relation is given by equation (7.1) are more conveniently expressed in their discrete version, as any numerical solution of the integral equation for continuous variables will require an approximation by a finite number of elements. A measure of $g(y)$ will be represented in the form of a histogram g_i, with i running over bins. For the sake of simplicity we will describe the discrete case. A more general expression can be obtained by adding a background term b_i (see expression 7.1), which we will ignore for now. In the discrete case we write the transition operator in a matrix form

$$y_i = A_{ij}x_j \tag{7.2}$$

If the true and measured variable coincide, in the most ideal case we can describe, the transition operator is the identical function. If we take into account limited acceptance, but no smearing, A_{ij} will still be a diagonal matrix with eigenvalues $\lambda^{(i)} \leq 1$. Those values can be seen as the acceptance, or probability of measurement, for each entry. In reality, a smearing between input data and results can occur, due to correlations between neighbouring

bins. The matrix element on the main diagonal of A will deviate from the identity by a small quantity ϵ. The better the resolution of the measurement, the greater the number of zero-value off-diagonal elements. The better the acceptance, the smaller the value of ϵ:

$$A = \begin{pmatrix} 1-\epsilon & \epsilon & 0 & ... & 0 \\ \epsilon & 1-2\epsilon & \epsilon & ... & 0 \\ ... & ... & ... & ... & ... \\ 0 & 0 & ... & 0 & 1-\epsilon \end{pmatrix}$$

The only off-diagonal terms are connecting neighbour bins. In the general case x and y are chosen with the same binning, which implies a square matrix. As we will see later in this chapter, it is possible to choose any binning for the input and output variables, so we will not lack generality with this assumption. Beside this, we can assume a symmetric matrix. In general, if no systematics affect the measurement, we can expect the smearing to be symmetric around the central value, provided that the number of measurements is large enough. The unfolding process consists of finding and inverting the matrix A

$$\vec{x} = A^{-1}\vec{y} \tag{7.3}$$

with the error propagation given by

$$\sigma_x = A^{-1}\sigma_y {A^{-1}}^T. \tag{7.4}$$

The result is easily achieved with a matrix A with dominating diagonal, and becomes worse as A shows large correlations between bins, namely large off-diagonal elements. In general, if A is a symmetric matrix, we can change basis to its diagonal form $D = UAU^T$ so that

$$\vec{y} = Ax = U^T DUx \Rightarrow U^T\vec{y} = DU^T\vec{x}. \tag{7.5}$$

In the new basis $c = U^T y$ and $b = U^T x$, and the unfolding relation is brought to diagonal form

$$c = Db. \tag{7.6}$$

The components do not mix ($c_j = \lambda^{(j)} b_j$) and the statistical fluctuation on the coefficients c_j is magnified or reduced by multiplication with the corresponding eigenvalue. As we will describe in the next paragraph, the direct inversion does not always fulfil the requirements of good statistical properties.
Our aim is to provide a numerical solution for the problem, applicable to the case of neutrino energy reconstruction. For this reason we will describe the perturbative approach to the solution, related to an iterative solution by likelihood maximisation.

7.2 Origin of the Problem Oddities

The point where the problem of unfolding encounters some difficulties can be identified trying to solve the problem by simple inversion. To do that, we can reduce to a 2 bins case, which does not lack generality respect to n bins. The relation between true and measured variables $y = Ax$ is defined through the operator A for which we assume the form

$$A = \frac{1}{2}\begin{pmatrix} 1+\epsilon & 1-\epsilon \\ 1-\epsilon & 1+\epsilon \end{pmatrix} \tag{7.7}$$

with $\epsilon \in [0,1]$ representing the efficiency of the detector, so that $\epsilon \to 1$ represents an ideal case. From elementary linear algebra, in general it is always possible to find two matrices U and V so that A can be written as $A = UDV^T$ with D being a diagonal matrix [75]. In particular if A is symmetric, this is a proper rotation of the form $A = UDU^T$. A matrix A of the form given in expression (7.7) is diagonalised to

$$D = \begin{pmatrix} 1 & 0 \\ 0 & \epsilon \end{pmatrix} \tag{7.8}$$

by the matrix

$$U = \frac{1}{\sqrt{2}}\begin{pmatrix} 1 & 1 \\ 1 & -1 \end{pmatrix} \quad . \tag{7.9}$$

Let us consider the vector y and the covariance matrix S which represent the measured variable and the statistical errors on the measured values in case there is no correlation between bins:

$$y = \begin{pmatrix} y_1 \\ y_2 \end{pmatrix} \qquad S = \begin{pmatrix} y_1 & 0 \\ 0 & y_2 \end{pmatrix}. \tag{7.10}$$

Solving the linear equation $y = Ax$ implies inverting A, which is more conveniently brought in its diagonal form

$$y = Ax = UDU^T x \tag{7.11}$$

Multiplying both sides by $U^{-1} = U^T$ we obtain

$$DU^T x = U^T y \tag{7.12}$$

$$Dx' = y' \tag{7.13}$$

here x' and y' denote the rotated vectors

$$x' = U^T x = \frac{1}{\sqrt{2}}\begin{pmatrix} x_1 + x_2 \\ x_1 - x_2 \end{pmatrix} \qquad y' = U^T y = \frac{1}{\sqrt{2}}\begin{pmatrix} y_1 + y_2 \\ y_1 - y_2 \end{pmatrix}. \tag{7.14}$$

The problem is solved inverting the matrix D. The inverse of a diagonal matrix is a diagonal matrix with inverse eigenvalues

$$D^{-1} = \begin{pmatrix} 1 & 0 \\ 0 & \frac{1}{\epsilon} \end{pmatrix}. \tag{7.15}$$

This matrix exists $\forall \epsilon \neq 0$. This allows for the solution of the system. Rotating back to the original basis we obtain the vector x

$$x = Ux' = UD^{-1}y' = \frac{y_1 - y_2}{2\epsilon} \begin{pmatrix} 1 \\ -1 \end{pmatrix} + \frac{y_1 + y_2}{2} \begin{pmatrix} 1 \\ 1 \end{pmatrix}. \tag{7.16}$$

The parameterisation of equation (7.16) illustrates the source of ill-poseness of the problem. If $\epsilon \to 0$ and the measured values y_1, y_2 are such that $(y_1 - y_2)^2 < y_1 + y_2$, the first term coefficient $y_1 - y_2$ is not statistically significant, whilst the second coefficient $y_1 + y_2$ has a statistical weight. But for $\epsilon \to 0$ the first coefficient becomes much larger than the second, so that in the solution the statistically random part prevails on the statistically well-behaving one. This originates a so called *random oscillation* problem. The errors are the components of the covariance matrix. In the rotated basis, for $(y_1 - y_2)^2 < y_1 + y_2$, the covariance matrix is diagonal and the two equations described by the system $y = Ax$ are decoupled:

$$S' = U^T S U = \frac{1}{2} \begin{pmatrix} y_1 + y_2 & y_1 - y_2 \\ y_1 - y_2 & y_1 + y_2 \end{pmatrix} \to \frac{1}{2} \begin{pmatrix} y_1 + y_2 & 0 \\ 0 & y_1 + y_2 \end{pmatrix} \tag{7.17}$$

$$y_1' = \frac{1}{\sqrt{2}} \left((y_1 + y_2) \pm \sqrt{y_1 + y_2} \right) \tag{7.18}$$

$$y_2' = \frac{1}{\sqrt{2}\epsilon} \left((y_1 - y_2) \pm \sqrt{y_1 + y_2} \right) \tag{7.19}$$

The second component y_2 becomes random and strongly amplified for small ϵ. When solving the system, this components contributes to both components of x, bringing the random factor contribution to have a strong part in the solution. This lays in the fact that the inverse of the matrix A has rank smaller than its dimension for $\epsilon \to 0$, as can easily be seen from the fact that the two lines of the first term are not linearly independent:

$$A^{-1} = \frac{1}{2} \begin{pmatrix} 1 & 1 \\ 1 & 1 \end{pmatrix} + \frac{1}{2\epsilon} \begin{pmatrix} 1 & -1 \\ -1 & 1 \end{pmatrix} \tag{7.20}$$

For this reason the solution of the problem requires a regularisation term with the function of limiting the random oscillating behaviour of the solution. The question is finding not an exact solution, but a best estimated for an unfolded vector x holding in the case of $(y_1 - y_2)^2 < y_1 + y_2$ and for small ϵ.
When going back to the origin of the problem, a small value of ϵ characterises a poor efficiency detector, implying a bigger difficulty in determining through unfolding both the components of x, process which is directly correlated with the size of the errors on y.

7.3 Covariance and correlation

A complication in the unfolding process occurs in cases of correlations between bins. Let f be the true variable obtained by the direct inversion of A

$$f = A^{-1}g \tag{7.21}$$

If the measured g has no bias, the expectation value $\langle\hat{f}\rangle$ is equal to the true $\langle f\rangle$. Error propagation from the measured g to the estimated f yields

$$\sigma\left(\hat{f}\right) = A^{-1}\,\sigma\left(\hat{g}\right)A \tag{7.22}$$

providing the covariance matrix $\sigma(\hat{f})$ from the covariance matrix $\sigma(\hat{g})$ of the measured data. Equation (7.17) shows that in A^{-1} there is a random oscillating term, which can amplify unphysical oscillations of $\sigma(\hat{g})$ giving them a large weight. In this sense the direct inversion method turns out to be not reliable.

Acceptable unfolding results can be obtained by regularisation. Regularisation is a sort of a-priori information on the smoothness of the true solution, which allows to keep random fluctuations under control. Since this can introduce a bias, the weight of the a-priori information has to be determined by statistical methods so that the resultant bias is small compared to the statistical errors. This means that a measure with limited resolution always means a loss of statistical accuracy.

7.4 The Likelihood Approach

The likelihood approach, implemented in the numerical unfolding code used in this thesis, is an alternative to the direct inversion. Let $\mathcal{L}(x, y, A)$ be the likelihood of having a measure y for the quantity x assuming a detector response A, with probability distributions $f(x)$ and $g(y)$. The number of events in bin i is $y_i = \sum_j A_{ij}x_j$. Assuming that the observed quantity $\hat{y}$ follows the Poisson distribution, an estimate for x is obtained by maximising the likelihood

$$\mathcal{L}(x, y, A) = \prod_{i=1}^{n} \mathcal{P}(y_i, \hat{y}_i). \tag{7.23}$$

For numerical implementation, this is better achieved minimising the negative logarithm

$$S = -\ln\mathcal{L}(x) = \sum_{1}^{n} y_i - \sum_{1}^{n} \hat{y}_i \log y_i + k, \tag{7.24}$$

where the constant k contains the factorial $\hat{y}!$. From now on we will disregard the constant terms, as the problem is to minimise this function. To determine the minimum, S is approximated by a quadratic function in the neighbourood

of a point x_0. The density function $f(x)$ is expanded on the functions p_j[1] with coefficients a_j

$$f(x) = \sum_{j=1}^{m} a_j p_j(x). \tag{7.25}$$

As the purpose is to solve the problem perturbatively, in a region around a minimum x_0, the likelihood function can be written in the form

$$S(x) = S(x_0) - (x - x_0)^T \nabla S + \frac{1}{2}(x - x_0)^T H(x - x_0) \tag{7.26}$$

with the gradient ∇S and the Hessian H having as components the first and second derivatives of S. In this approximation, a minimum of the likelihood function is described by $\nabla S = 0$. The approximated result is

$$x_{app} = x_0 + H^{-1} \nabla S. \tag{7.27}$$

The second iteration is obtained by substituting x_0 with the first solution x_{app}. The convergence of such an iteration steps method is ensured by the condition that for every correction $\Delta S \ll S$ (perturbative regime). In the case of logarithm likelihood functions, it can be shown that it is reasonable to approximate them with a quadratic form close to the solution, therefore the convergence is reached within a few iteractions.

7.5 Interpolating spline functions

Spline functions are one of the possible solutions to interpolate between pairs (x_i, y_i) with $x_i \in [a, b]$. The discrete set $Y = y_1 ... y_n$ represents the values of a function $y = f(x)$ for $x = x_i$, with $x_1 = a, x_n = b$. A cubic spline function $S(x)$ is a function with $S(x_i) = y_i$, twice continuously differentiable in the interval $[a, b]$, coinciding on every subinterval $[x_i, x_{i+1}]$ with a third degree polynomial

$$S_i(x) = a_i + b_i(x - x_i) + c_i(x - x_i)^2 + d_i(x - x_i)^3 . \tag{7.28}$$

The points x_i are called *knots*. At every inner knot x_i the two polynomials defined on adjacent intervals have the same value and the same first two derivatives. If the x axis is divided into $n-1$ intervals, resulting into n knots, $4(n-1)$ parameters have to be determined for the interpolating cubic spline $(a_i, b_i, c_i, d_i, i = 1...n)$. The conditions of $S(x_i) = y_i$ are n and allow the determination of the n parameters a_i. The conditions of continuity at the inner

[1] We have introduced orthogonal functions $p_j(x)$ defined in an interval $[a, b]$, with the property

$$(p_j, p_k) = \int_a^b p_j(x) p_k(x) dx = \delta_{jk}$$

knots are $n-2$ for $S'(x)$ and $S''(x)$, providing $3n-2$ equations for the remaining $3n$ parameters. What remains to be determined are just the first and last knot. An usual, but not unique, choice is the "not-a-knot" condition

$$S''(x) \text{ continuous across } x_1, x_{n-1}. \tag{7.29}$$

The difference $|S(x)-f(x)|$ is bound by a quantity proportional to $(x_n - x_{n-1})^4$, where $x_n - x_{n-1}$ is the distance between neighbouring knots.

7.6 Regularisation

As mentioned before, the inverse problem of obtaining $f(x)$ can show an unsatisfactory solution, with oscillating behaviour and fluctuations much larger than any physically motivated expectations. Mathematically the fluctuations are caused by minor components of the solution which get a large weight in the unfolding. A measure of those fluctuations can be done considering the total curvature

$$r(x) = \int [f''(x)]^2 dx. \tag{7.30}$$

The regularisation term is chosen as $\tau \cdot r(x)$ and added to the negative likelihood logarithm

$$-log\,\mathcal{L} \rightarrow -log\,\mathcal{L} + \frac{1}{2}\tau \cdot r(x) \quad . \tag{7.31}$$

The parameter τ has to be balanced between two limit cases

$$\tau \quad \rightarrow 0 \quad \Rightarrow \text{no effect of regularisation} \tag{7.32}$$

$$\tau \quad \rightarrow \infty \quad \Rightarrow \text{large bias in the resulting function} \tag{7.33}$$

The reason why such a regularisation term is chosen, which is just one among different possible choices, is that the curvature of a cubic spline function has the expression of a quadratic form

$$\int [f''(x)]^2 dx = x^T \mathcal{C} x \tag{7.34}$$

with $\mathcal{C}$ being a symmetric matrix. After the introduction of the regularisation term, the problem reduces to find the minimum of

$$-log\,\mathcal{L} + \frac{1}{2}\tau \cdot r(x) \simeq x^T \nabla + \frac{1}{2} x^T H x + \frac{1}{2}\tau \cdot x^T \mathcal{C} x \tag{7.35}$$

$\mathcal{C}$ can be brought in diagonal form simultaneously with H. In the new basis, naming c_j the eigenvalues of $\mathcal{C}$, the regularised vector is

$$y_j^{\text{reg}} = \left(\frac{1}{1+\tau c_j} \right) y_j \quad . \tag{7.36}$$

The bias introduced by the regularisation can be kept small compared to the number of events by an appropriate choice of τ.

7.7 A Numerical Solution

In this thesis, we make use of the numerical algorithm $\mathcal{RUN}$ [76], implemented in FORTRAN, applied to reconstruct the neutrino energy spectrum. Our problem belongs to the category of cases in which the transition operator A is not known, and the true distribution is simulated with a Monte Carlo method. In words, we have available two samples: a simulated one in which both the true and the measured variables are known, and a real one, in which only the measured variable is known. The larger the amount of data available, the more precise the unfolding rule; additionally, this allows us to introduce the regularisation condition keeping the bias small enough not to influence the statistical accuracy of the result. Both samples, the simulated and the real data, are given in the form of an ASCII table. A steering file contains the options to be set by the user, namely

- XLIMITS: lower and upper limit of the interval where the unfolding is performed.
- XBINS: bin edges for the unfolded variable, defined between the two limits mentioned above.
- VARIABLE: name or number of the input variable, followed by the number of bins of its distribution. Up to three variables are accepted as unfolding inputs.
- NRDF: number of degrees of freedom, related to the strength of the regularisation. It is recommended to choose this parameter as the number of data points, which in our case is the number of bins.
- KNOTS: number of knots of the cubic spline interpolating functions. A reasonable choice is twice the number of the degrees of freedom.
- FXPOSITIVE: option that allows only positive values for the unfolded variable.
- SMOOTH: smoothness of the interpolating function of the Monte Carlo n-tuples.

The steering file is read out by a main script which performs the unfolding in three steps. First he true and measured variable are read in from the kernel file; with these two bits of information, the transition operator A can be created. Secondly, the table containing the measured variables is read in. It has to be pointed out that it is possible to consider weighted Monte Carlo events, in which case one of the columns of the kernel file will be reserved for the weight of each event. This is the case of this analysis, in which different weights are used to reproduce the different neutrino spectral shapes. The routine CALL UEVENT reads the event information from ASCII format and creates an n-tuple of the type

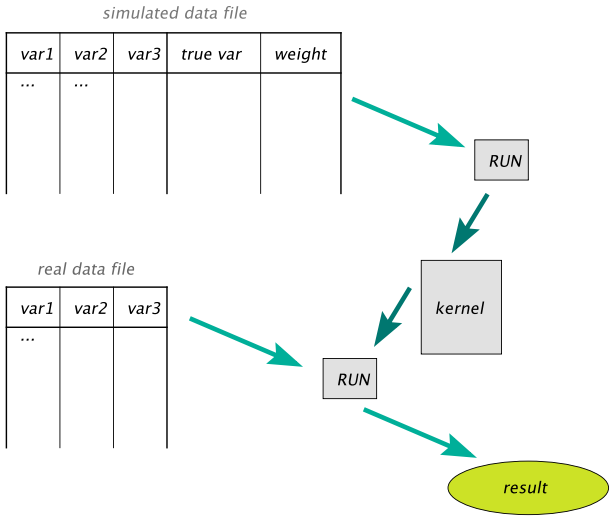

Figure 7.1: The RUN algorithm receives a simulated data file in ASCII format, as input, with the three variables that will be used for the unfolding and the true variable (with weight if required). With the simulated file, the kernel is built. When real data are processed, RUN calls the pre-built kernel to unfold and reconstruct the variable for data.

LABEL	NY	WT	X	Y(1)... Y(NY)

where LABEL is a string of four characters indicating the data type: data, Monte Carlo background, Monte Carlo signal. NY is an integer representing the number of y values. WT is the weight of the event, in the general case. X is the true variable. Y(1)... Y(NY) is an array containing measured or simulated data, according to the type. A likelihood function can be constructed at this point, having the expected and observed number of entries for each bin. Minimisation is performed in iterative steps. The results are regularised by a term containing the curvature of a cubic spline function, whose interpolating function parameters *knots* and *degrees of freedom* are chosen by the user.
The output is stored into a *data* and a *log* file. In the data file, a binned distribution (bin, value) is given for the unfolded variable. All the details about the processes, the minimisation procedure, the covariance matrix analysis and the regularisation parameter determination are stored in the log file.
Finally, the correlations between neighbouring bins are analysed and provided in the output, in the form of a χ^2 probability distribution. If the trend is almost constant, the correlations can be ignored, the data point can be considered with their diagonal errors only and the regularisation procedure has worked successfully.

Chapter 8

The Atmospheric Neutrino Flux

Atmospheric neutrinos are decay products of secondary particles that are created in cosmic ray interactions. Most of them originate from pion and kaon decays; minor contributions, of great interest for this analysis, are due to decays of charmed mesons and baryons ("prompt neutrinos"). In this chapter we compare the data taken with the AMANDA detector during the 2000-2003 period with simulated models of various spectral shapes. Neutrinos from heavy quark decays are expected to show a different energy dependence with respect to neutrinos from pion decays. A numerical unfolding algorithm is applied to reconstruct the neutrino energy spectrum. We aim to resolve the signal of prompt neutrinos from the background of conventional events and set an upper limit to the prompt flux. This investigation is motivated by the need to describe as precisely as possible the complete atmospheric spectrum, which is a background to all searches for celestial neutrinos extraterrestrial origin. Particular emphasis is given to the prompt contributions, as they become important in the high energy region.

8.1 Particles Produced by Cosmic Rays

Cosmic rays consist of protons and nuclei. The question of their origin is not yet resolved, however there have been recent observations of very high energy events which might be correlated with astrophysical objects, as nearby active galactic nuclei [81]. The acceleration mechanism that can produce particles at the highest observed energies (10^{20} eV) still needs to be understood. Those particles traverse the atmosphere and originate air showers, with of a broad series of secondary products. Neutrino-induced muons, which are the signal detected in AMANDA for this analysis, are produced in most cases for neutrino energies between 1 and 10^4 GeV [82]. In this energy range, the dominant primary particles are protons and α particles. Heavy nuclei start contributing

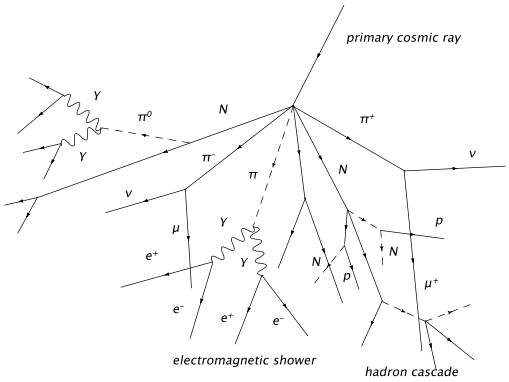

Figure 8.1: Left: Primary cosmic rays interact in the atmosphere to produce a large number of secondary particles.

around 10^5 GeV per nucleon [111]. Neutrinos originate in air showers as secondary decay products. The main channel for neutrino production in the atmosphere is the decay of charged pions

$$\pi^{\pm} \rightarrow \mu^{\pm} + \nu_{\mu}(\overline{\nu}_{\mu}) \rightarrow \overline{\nu}_{\mu}(\nu_{\mu}) + e^{\pm} + \nu_e(\overline{\nu}_e) + \nu_{\mu}(\overline{\nu}_{\mu}). \tag{8.1}$$

The charged pion has a lifetime of $\tau = 2,603 \times 10^{-8}$ s, and the relative branching ratio for its decay to neutrinos is $99,99\%$ [112]. As can be seen from expression (8.1), charged pions produce twice as many muon neutrinos to electron neutrinos. Considering that pions are one of the most abundant particles produced in the atmosphere, it follows that muon neutrinos are the predominant flavour. Other relevant reactions that lead to the production of neutrinos in the atmosphere are the decay of charged kaons ($\tau = 1,238 \times 10^{-8} s$) and the decay of the neutral kaon ($\tau = 5,18 \times 10^{-8}$ s)

$$\begin{aligned}
K^{\pm} &\rightarrow \mu^{\pm} + \nu_{\mu}(\overline{\nu}_{\mu}) \\
K^{\pm} &\rightarrow \pi^0 + e^{\pm} + \nu_e(\overline{\nu}_e) \\
K^{\pm} &\rightarrow \pi^0 + \mu^{\pm} + \nu_{\mu}(\overline{\nu}_{\mu}) \\
K^0_L &\rightarrow \pi^{\pm} + e^{\mp} + \overline{\nu}_e(\nu_e) \\
K^0_L &\rightarrow \pi^{\pm} + \mu^{\mp} + \overline{\nu}_{\mu}(\nu_{\mu})
\end{aligned} \tag{8.2}$$

The cosmic ray spectrum has been largely investigated with balloon experiments, satellites and ground arrays. In general, the flux of primary cosmic rays (number of particles per unit area per unit time) depends on the energy with a power law, described by the *spectral index* γ. For primary cosmic ray particles the spectral shape is governed by $\gamma = 2$ to $2,7$. The spectrum smoothens after the first interaction; as a consequence, the atmospheric neutrino flux is characterised by a spectral index going from $\gamma = 3,7$ at low energies (10 GeV) to $\gamma = 2,7$ at about 100 GeV. As shown in figure 8.2, there are additional

regions, the *knee* and the *ankle*, where the slope changes again. A suppression of events at energies above 10^{18} eV reflects the effect of the interaction of high energy particles with the cosmic microwave background, which is known as the GZK cutoff [83].

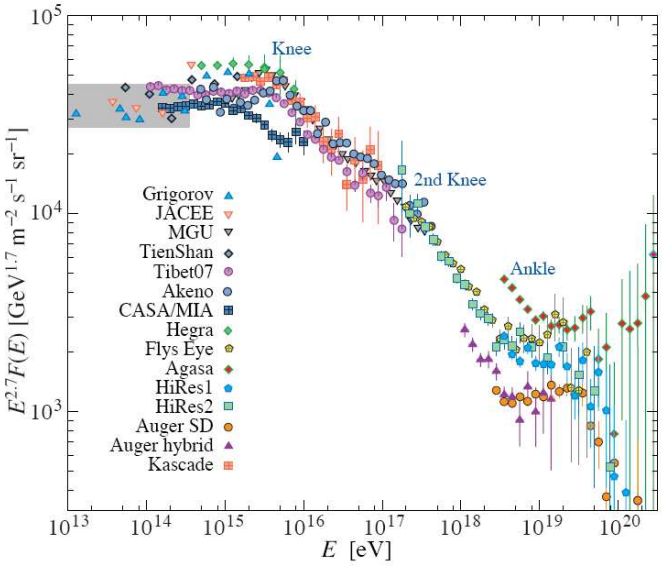

Figure 8.2: The primary cosmic ray spectrum [118]. The shape of this distribution is parameterised with a power law with exponent $\gamma = 2$ to 2.7. This fit is based on several observations by ground arrays and balloon experiments. The very high energy region, of great interest for astro-particle physics, still carries remarkable uncertainties. Observing particles in this region is unlikely, which justifies the construction of large arrays to detect them.

8.2 Conventional and Prompt Neutrino Flux

In the literature, the so called conventional neutrino flux includes contributions of the light quarks u, d and s. Processes of this type are decays of light hadrons (expressions (8.1) and (8.2)). The decays in flight of charged kaons and pions contribute to the atmospheric lepton flux up to $\mathcal{O}(10$ TeV). Above this threshold, the semileptonic decay of charmed particles becomes the dominant source of atmospheric leptons. The main contribution to the creation of prompt neutrinos is represented by the channels

$$\begin{aligned} D^+ &\rightarrow \overline{K^0} + l^+ + \nu_l \\ D^0 &\rightarrow K^- + l^+ + \nu_l \\ \Lambda_c &\rightarrow \Lambda_0 + l^+ + \nu_l. \end{aligned} \tag{8.3}$$

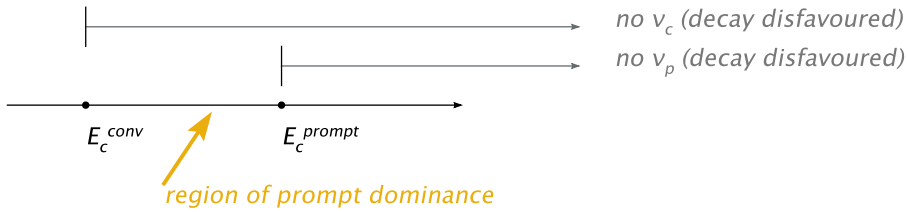

Figure 8.3: The region between the typical critical energy for a conventional source and that of a prompt source is dominated by contributions of prompt neutrinos. Most of neutrinos come from decay of secondary particles rather than from interaction processes; in the figure, ν_c and ν_p are respectively conventional and prompt.

Prompt neutrinos have a harder energy spectrum than the conventional ones, because of the short life time of their mother particle. The parameter establishing the preferred source of atmospheric neutrinos is the critical energy E_c of the parent particle, defined as the energy at which decay and interaction lengths are equal:

$$E_c = \frac{mc^2}{c\tau} h_0, \tag{8.4}$$

where h_0 is a constant whose value is determined from the isothermal atmosphere approximation [89], τ is the lifetime of the particle and m the mass. The critical energy is a constant for each particle type. Above E_c the particle interacts before decaying into a neutrino, with the interaction probability dependent on the atmospheric density as well as the propagation length. The values of the critical energy for some conventional and charmed particles are reported in table (8.1). It is immediately clear that values of E_c for particles belonging to the first group are higher; the energy region where interaction prevails over decay, suppressing the probability of neutrino production, begins later than for conventional parts. The conventional and prompt spectrum are compared in figure 8.5 for a simulated sample. We point out that the region of predominance of prompt neutrinos is almost at the edge of the visibility threshold of the AMANDA detector; the large instrumented volume of IceCube will definitely increase the sensitivity to such events. The actual failure to observe prompt neutrinos might impose constraints on the charm production cross sections at high energy. Such an investigation is also related to the determination of the gluon parton distribution function, as it has been shown that the spectral index of prompt neutrinos depends linearly on the slope of the gluon PDF at very small x, which is a region not accessible at colliders.

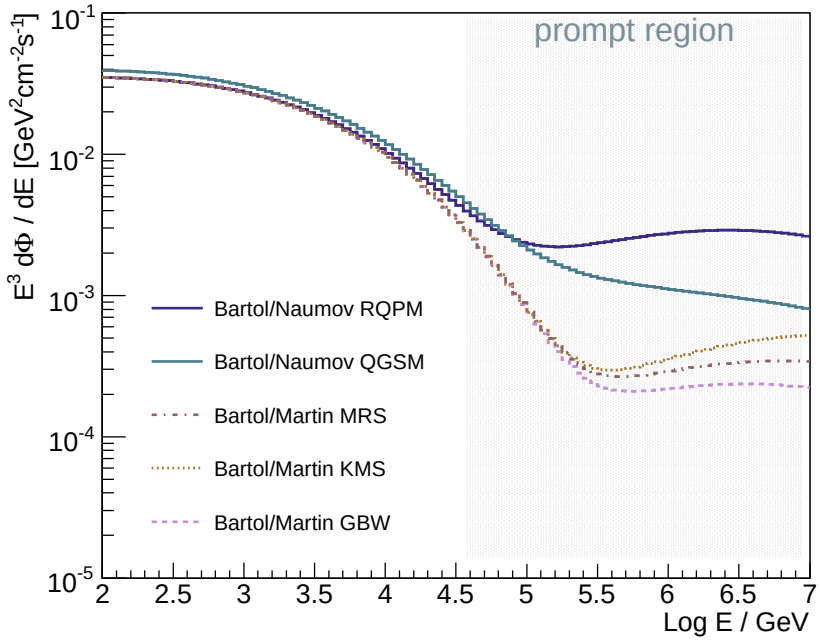

Figure 8.4: Conventional and prompt contributions to the neutrino energy spectrum. Prompt becomes dominant for $E > 10^5$ GeV.

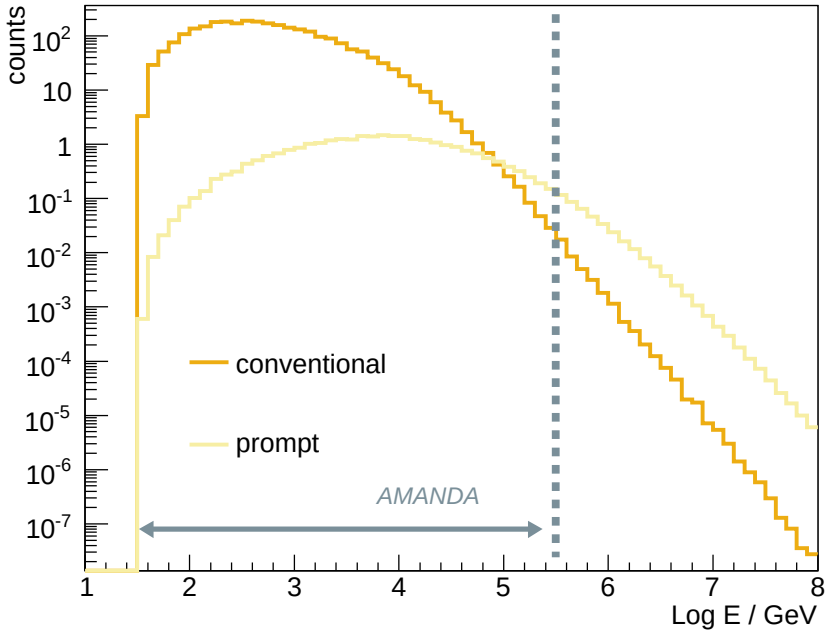

Figure 8.5: Comparison of conventional and prompt spectra. The AMANDA accessible region is indicated with an arrow. The lower threshold is due to the multiplicity trigger (see 2.5.3), requiring a minimal energy of around 100 GeV to fulfil the condition. The upper threshold is due to lack of statistics in the very high energy region. The latter makes it a challenging task to identify prompt events.

Particle	*Elementary components*	mc^2 (MeV)	E_c (GeV)	
D^+, D^-	$c\bar{d}, \bar{c}d$	1870	3.8×10^7	prompt sources
$D^0, \overline{D^0}$	$c\bar{u}, \bar{c}u$	1865	9.6×10^7	
D_s^+, D_s^-	$c\bar{s}, \bar{c}s$	1969	8.5×10^7	
Λ_c^+	udc	2285	2.4×10^8	
μ^+, μ^-		106	1.0	conventional sources
π^+, π^-	$u\bar{d}, \bar{u}d$	140	115	
K^+, K^-	$u\bar{s}, \bar{u}s$	494	855	
Λ_0	uds	1116	9.0×10^4	

Table 8.1: Values of the critical energy for some charmed and conventional neutrino sources [114].

8.3 Heavy Quark Production

To understand the prompt neutrino spectrum, the production of charmed hadrons in the atmosphere is investigated. Unlike up and down quarks, which are abundant in nature (cosmic rays are composed mostly of protons and nuclei), heavy quarks have their origin in scattering processes happening in the atmosphere. The collision of a cosmic ray particle on an atmospheric nucleus producing one or more charm quarks is a deep inelastic QCD process. The diagrams contributing to the inclusive charm production cross section, from a general hadronic initial state, are shown in figure 8.9. The scattering or annihilation can take place on either sea or valence components; with the exclusion of diagram (b), all the processes can lead to the production of a $c\,\bar{c}$ pair. The transition $p + N_{air} \rightarrow c(\bar{c}) + X$ is a process whose evaluation is affected by different uncertainties of theoretical nature:

- Parton distribution functions (PDFs) of the quarks and gluons in the proton/neutron (see section 1.9), which cannot be calculated in perturbative QCD, and must rely on fits to data and numerical extrapolation. Additional uncertainties appear because the data available at colliders need to be extended the energy region of interest for cosmic rays. This requires some prior assumptions on the behaviour of the PDFs as a function of x and Q^2 (see section 1.9).

- Fragmentation functions, describing meson and baryon production via hadronisation processes of the outcoming quarks (see section 8.4). Quarks in the final state first evolve in parton showers loosing energy, and then combine into hadronic final states, bound by confinement. Parton showers are simulated numerically based on QCD; at a certain energy threshold ($\sim$ 1 GeV), where quarks condensate in hadrons, the perturbative

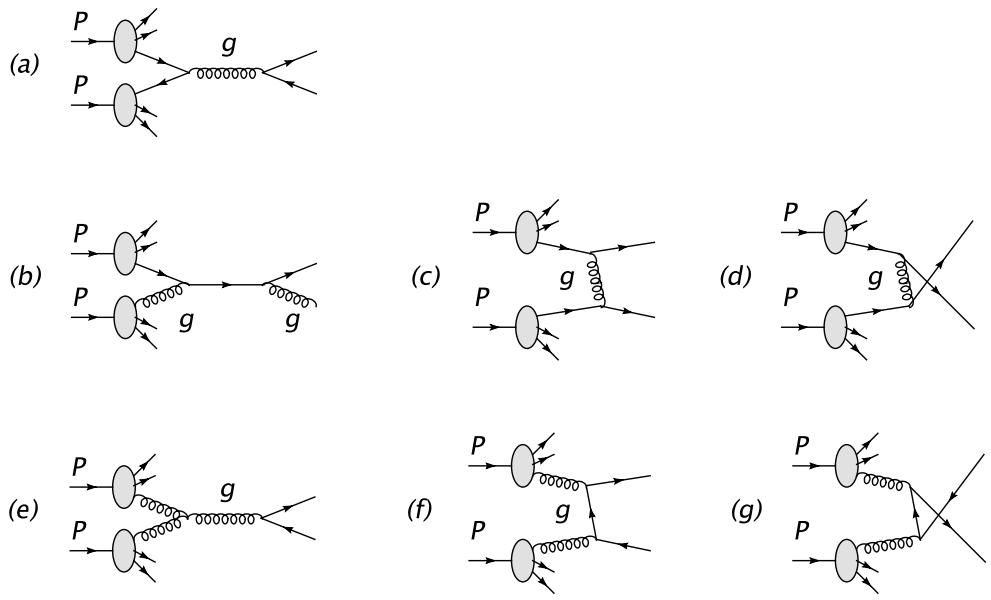

Figure 8.6: Channels leading to the production of charm quarks from cosmic rays. Diagram (a) describes the annihilation of valence or sea quarks to a gluon. Diagrams (b), (c), (d) represent scattering off a sea quark. Diagrams (e), (f), (g) are for scattering on a sea gluon.

approach is no longer valid.

- QCD cross section for the elementary process

$$p_1 + p_2 \to c\,(\,\bar{c}\,) + X$$

  where p_1, p_2 are two generic partons in the nucleon and X can be any quark or a gluon.

- Higher order corrections to the QCD process. This is a general issue to increase precision of any perturbative calculation. The diagrams in figure 8.9 are all at Born level; their number grows considerably at next-to-leading orders.

- Evaluation of the scale dependence of the process. When computing the elementary cross section with light quarks in the high energy regime, the quarks are assumed to be massless. This is not a valid approximation for charm quarks, where a mass term remains in the final cross section introducing a scale dependence.

Often in all what follows the main attention will focus on $c\bar{c}$ pairs, whilst a minor role is played by $b\bar{b}$. The contribution of bottom quark is suppressed until $Q^2 \gg m_t^2 \sim 3 \cdot 10^4\,\mathrm{GeV}^2$, as the dominant coupling is represented by

$b \to t$. Atmospheric flux has a strong dependence on gluon PDF at momentum fraction $x < 10^{-5}$. Charm pair production happens via scattering of a cosmic ray parton of momentum fraction x on an atmospheric nucleon, originating a lepton of energy E_l in the atmospheric reference frame. The lepton energy E_l is of the order of 0.1 E, where E is the energy of the incoming cosmic ray nucleon. In this kind of process, the parton momentum fraction involved is of the order of E^{-1} [110], hence, if a lepton of energy $E_l = 10^5$ GeV is produced, a parton with momentum $x < 10^{-5}$ takes part to the scattering process. For $x \ll 1$, the PDFs are described by the parameterisation

$$x f(x, Q^2) \sim A\, x^{-\lambda(Q^2)} \tag{8.5}$$

The gluon density grows as x descreases, reaching the order of quark density at $x \simeq 0.3$ and being strongly predominant at $x < 10^{-3}$. In perturbative QCD calculations applied to charm pairs production from cosmic rays interactions, the quark density is normally disregarded. For this reason, the predominant contribution to $\sigma(\text{hadron-hadron} \to c\bar{c})$ is apported by the diagrams in figure 8.7 Models predicting the flux of neutrinos from heavy quarks contributions

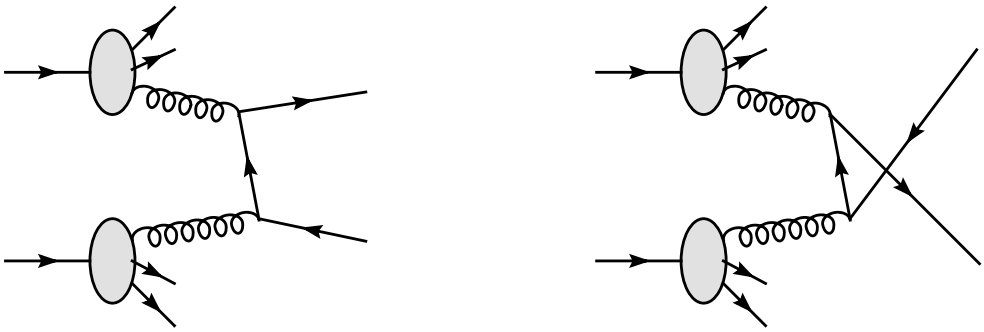

Figure 8.7: The two main contribution to $\sigma_{c\bar{c}}$. At $x \leq 10^{-5}$, the major contribution to the inclusive charm quark production cross section is given by the gluon PDFs.

differ by more than two orders of magnitude. The arbitrary choice of a way to extend the parton distribution functions at high energy is the reason of such discrepancies. Both phenomenologic and perturbative methods have to estrapolate input parameters in a region of (x, Q^2) where no data are available.

The cross section for charm production happening through the process of figure 8.7 can be factorised as

$$\frac{d\sigma}{dx}(pp \to c + X) = \int dx_1\, dx_2\, dz\, g(x_1, \mu^2) \frac{d\sigma_{gg \to c\bar{c}}}{dz}\, g(x_2, \mu^2)\, \delta(z x_1 - x) \tag{8.6}$$

where x is the scaling variable, approximated at this high energy regime as E_c/E, being E_c the charm quark energy, and E the proton energy. The functions g are the gluon PDFs referred to a momentum fraction x_1, x_2 for

the two partons. μ^2 is the energy scale. The gluon PDFs in the energy region $x < 10^{-5}$ can be obtained from the DGLAP evolution equation. At fix Q^2, for variable x, the gluon PDFs are dominated by logarithmic terms $\sim \alpha_s \ln(1/x)$.

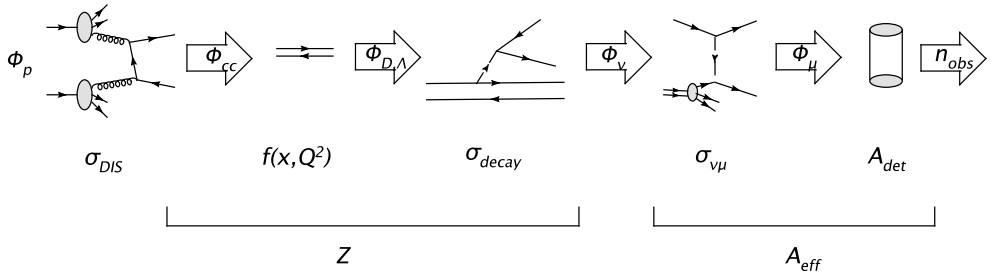

Figure 8.8: The different cross sections involved in the process of a prompt neutrino production and detection from cosmic rays. The incoming cosmic ray primaries with flux Φ_p participate to a DIS scattering process producing a $q\bar{q}$ pair (Φ_{cc}). Each quark hadronises through fragmentation and combines into secondary mesons or baryons (with flux $\Phi_{D,\Lambda}$). Consequently, this particle decays with a cross section σ_{decay} to prompt neutrinos, which are emitted with flux Φ_ν. A charged current scattering ($\sigma_{\mu\nu}$) originates a muon with flux Φ_μ. Last, this particle traverses the detector, which has a finite geometry A_{detector}. The resulting number of observed events is n_{obs}. The Z-moment (mentioned further in section 8.6.1) includes the probability of producing a secondary particle of type (i) with energy E_i, from a primary with energy E. The neutrino effective area of the detector has been evaluated on the basis of a simulation in section 6.5 and relates the number of observed events in the detector with the neutrino flux.

8.4 Fragmentation Functions

Fragmentation is the process through which quarks combine into an hadronic final state, with a fast recombination governed by confinement forces. It links the hard process of parton showers, which can be described in perturbative QCD, with a condensation in bound states. A specific function is given for each transition

$$q(\bar{q}) \rightarrow \text{h}. \tag{8.7}$$

The QCD potential at low energy, necessary to describe quark bound states, cannot be described in a perturbative framework; it must rely on numerical methods based on phenomenological observations. Heavy quarks show a different fragmentation behaviour with respect to u, d, s. In particular, charmed hadrons might result from the recombination of the produced quark with a

sea parton of the initial state [79]. Because of the charm quark mass, the $c\bar{c}$ pair is disfavoured respect to one signle charm production. The recombination process of one charm produced in the scattering (leading charm) with one sea charm happens inside a short time; consequently the spectrum of the charmed meson or baryon is similar to that of the charm quark before fragmentation. This last fact suggests to use charm production data from collider experiments [80] We refer for the topic of evaluation of the fragmentation function to specific works, as [79] and [80].

8.5 Decay of Charmed Hadrons

Prompt neutrinos are the decay product of a hadron containing heavy quarks. The lifetime of such heavy particles is short, of the order of $10^{-14} - 10^{-15}$ seconds. This means that the average path lengths vary from $\mathcal{O}(300)\,\mu$m for $D^{\pm}$ to $\mathcal{O}(100)\,\mu$m for Λ_c^+[114]. The decay rate information is included in the models, as will be mentioned in the following section. Prompt neutrinos carry a large fraction of their parent particle energy. In the case of prompt particles, no remarkable difference is observed in the ratio between vertical and horizontal events. In the short time which precedes the decay, a change in the atmospheric density cannot be appreciated. Zenith angle dependence is less peaked for prompt lepton fluxes.

As an order of magnitude, the inelastic interaction cross-sections for D and Λ decays can be approximated with the elastic values. Such approximation is valid up to $\mathcal{O}(10^4\,\text{TeV})$ and yields $\sigma(D - \text{Nucleus}) \sim 100$ mb and $\sigma(\Lambda - \text{Nucleus}) \sim 200$ mb, with $D = D^{\pm}, D^0, \overline{D^0}$ and $\Lambda = \Lambda_c^{\pm}$. The muon spectrum deriving from charmed hadron decay depends on the branching ratio $B(i \to \mu\nu X)$, the ratio E_{cr}/E with critical energy defined in expression 8.4, the cinematic of the process regulated by the mass of the charmed hadron involved and the secondary particle production spectrum [95].

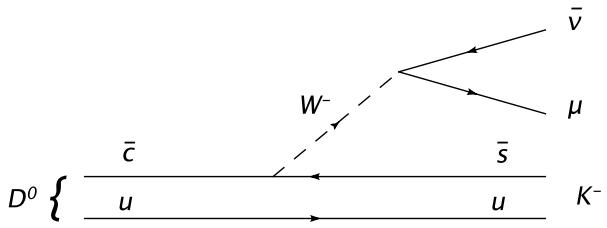

Figure 8.9: The decay of a charmed hadron is realised through a W exchange. The charm quark is converted into strange, and an highly energetic neutrino-lepton pair is emitted.

The neutrino effective area accounts for both the effects of detector acceptance and neutrino-muon cross-section. Convoluting the measured number of events with the effective area and the time analysed, we obtain the starting

neutrino flux Φ_ν. It would be interesting to proceed further back to the deep inelastic process $pN \to q\bar{q}$. The Z-momentum includes all information about the decay of the secondary particles to neutrinos. We refer to prompt neutrinos, as we aim to use the limit on their expected flux to constrain parameters of the deep inelastic process. The scattering of a cosmic ray proton on an atmosphere nucleus is a fix target process. The flux of incoming particles is known from the cosmic ray parameterisation. On the other side, the flux of outcoming particles Φ_{out} can be deduced by our observation convoluted with the effective area. This represents the number of prompt hadrons produced in the cosmic ray-air collision, after fragmentation. The transition probability depends also on the atmosphere density and on the length traveled by the incoming particle: those two parameters, together, can be summarised in the superficial density $\rho = 1/A^2$. The two fluxes are linked by the relation

$$\Phi_{\text{out}} = \Phi_{\text{in}} \cdot \sigma_{pN \to q\bar{q} \to \text{hadrons}} \cdot \rho \tag{8.8}$$

where Φ_{in} is the primary cosmic ray flux. Through this relation, a limit obtained on the neutrino flux at the detector could be translated into a limit on the QCD process, inclusive of all quantities which parameterise it. Of course this would imply a precise knowledge of the atmospheric density.

8.6 Calculation of the Neutrino Flux

Constructing a model which successfully reproduces the observed neutrino flux is quite a complicated issue for whose details we refer to the specific literature (see e.g. [114] and [95]). Here only the main steps of the calculation are summarised. The starting point is the primary cosmic ray spectrum at the outer edge of the atmosphere ($x = 0$), mainly composed of protons, and described by a power law

$$\Phi(E, x = 0) = N_0 E^{-\gamma}. \tag{8.9}$$

From the moment they enter the Earth's atmosphere, cosmic rays originate showers through interactions with air molecules, producing secondary particles. At the depth x, the nucleon flux is given by

$$\Phi(E, x) = N_0 \, E^{-\gamma} \, e^{-\frac{x}{\lambda}}, \tag{8.10}$$

with λ being the nucleonic attenuation length. A convolution of the spectrum of equation (8.10) with the production spectrum K_i of the secondary channel i yields

$$\Phi_i(E_i, x) = K_i(E_i, \gamma - 1) \int_0^x dy \, \left(\frac{y}{x}\right)^\eta \, e^{\left(-\frac{x-y}{\lambda_i} - \frac{y}{\lambda}\right)} \tag{8.11}$$

where λ_i are the interaction lengths of the particle i. The variable η is defined as

$$\eta = \frac{E_c}{E_i \, \cos\theta}. \tag{8.12}$$

As a third step, to obtain the flux of leptons originated by decays of secondary particles, the energy spectrum of the produced lepton is convoluted with the spectrum of the decaying parent particles

$$\Phi_{\text{lepton}}(E_{\text{lepton}}, x) = \int_0^x dz \int_{E_i^{\max}}^{E_i^{\min}} dE_i \left(\frac{df_{\text{lepton}}}{dE_{\text{lepton}}} \right) D_i(E_i, z), \tag{8.13}$$

where x, y, z are altitudes in the atmosphere, $df_{\text{lepton}}/dE_{\text{lepton}}$ is the energy distribution of the produced lepton, and $D_i(E_i, z)$ the spectrum of the decaying secondary particle of type i. This last quantity depends on the production spectrum, declination angle, critical energy of the secondary particle i, and its branching ratio for leptonic decays B_i:

$$D_i(E_i, z) = B_i \frac{E_c}{z \cos\theta \, E_i} \Phi_i(E_i, z). \tag{8.14}$$

Parameters still to be fixed by fits on experimental data are the primary cosmic ray spectrum normalisation N_0 and the slope γ, the nucleon attenuation length λ, the secondary particles interaction lengths λ_i, and the secondary production spectrum K_i.

8.6.1 A note about the Z-moment

As it will turn out to be of particular interest for this analysis, we will investigate the charm production spectrum in more details. To do so, we select the D-mesons $D^{\pm}$, D^0, $\bar{D}^0$, $D_s^{\pm}$ and the Λ_c^+ baryon as possible secondary particles. The production spectrum of charmed particles convoluted with the primary nucleon spectrum is

$$K_i(E_i) = \int_{E_i}^{\infty} dE \, \frac{N_0}{\lambda} \, E^{-\gamma} \, \frac{dW_i(E_i, E)}{dE_i}, \tag{8.15}$$

with $dW_i(E_i, E)/dE_i$ being the probability distribution of the secondary particle i to be created from a nucleus of energy E, calculated from the inclusive cross-section $\sigma(pN \to iX)$. Often in literature, the cross-section dependence is isolated in the Z-moment

$$Z_{Ni} = \int_0^1 dx_F \, \frac{dW_i}{dx_F} \, x_F^{\gamma}, \tag{8.16}$$

where the variable x_F is the fraction of energy of the nucleon going to the produced particle i

$$x_F = \frac{E_i}{E}. \tag{8.17}$$

The quantity $\frac{dW_i}{dx_F}$ in expression (8.16), contains the difference between prompt production models. In particular, the hadronic interaction model chosen in the calculation of the cross section $p + N \to c + X$ labels the different schemes (see section 8.9).

8.7 Flux Models

The aim of this and the following chapter is to reproduce the spectrum of atmospheric neutrinos, accounting for different models and convoluting them with the features of the AMANDA detector. The neutrino flux is introduced in our simulated data sample with the use of the C++ class `neutrinoflux` developed within the framework of the AMANDA Collaboration software [115]. The flux value has been used in the present work as a weight to the neutrino spectrum, by changing the standard weight parameter introduced in the original NUSIM Monte Carlo simulation. In our analysis we take the zenith dependence into account by referring to the zenith angle of the lepton track (see section 4.4.2); tables for the diffuse flux, integrated over zenith angle, are however also available.

8.7.1 Calculation Details

One-dimensional vs Three-dimensional Models

Early calculations of the neutrino flux were based on a 1-dimensional approximation. This means that the whole chain leading to neutrino production is adapted to a linear track, which is the direction of the primary cosmic ray particle at the first interaction vertex. This simplification reduces the computation time, as it limits the simulation to tracks pointing to the detector site. What is missed is the bending of charged secondaries (muons) caused by the geomagnetic field. This correction, which is included in the three-dimensional models, is of great importance to analyses focused on the arrival direction of neutrino-induced events, i.e. in oscillation searches. However, the effects of magnetic curvature only influence particles up to $\mathcal{O}$(GeV).

Interaction Model

The interaction vertex of a cosmic ray particle in the atmosphere is simulated and convoluted with the cosmic ray primary flux. The probability that two neutrinos from the same shower are detected is practically zero, due to the extremely low cross section for charged current scattering, which turns a neutrino into a visible lepton. For this reason only inclusive, single particle hadron production is considered. Typical input parameters for the interaction simulation are a proton as the incoming particle, and a light atmospheric nucleus as the target (beryllium, carbon or oxygen). The initial proton energy is shared between the different daughter particles of the shower. Whenever a meson (pion or kaon) is produced as a secondary particle, a neutrino originates from its decay. The atmospheric density affects this process for energies > 200 GeV in the case of pions, and > 600 GeV for kaons. Uncertainties on the hadron production have been evaluated on the basis of measurements at

accelerators.

Geomagnetic Effects

Geomagnetic effects influence the zenith angle distribution of low energy neutrinos below 1 GeV [92]. They result in a breaking of the up-down symmetry and lead to an azimuthal dependence of the neutrino fluxes called east-west effect. The development of a hadronic shower only depends on the zenith angle once the mass and energy of the originating primary particle is fixed. Cascades at large zenith angle develop in a less dense atmosphere, so that decays to neutrinos at large angles are enhanced. Apart from small effects due to the temperature, the development of a shower does not depend on the position of its impact point on the Earth's surface. This means that the production of secondary particles in the atmosphere is symmetric when replacing $\cos\theta \rightarrow -\cos\theta$ with θ being the zenith angle. The effects of the geomagnetic field modify the spectrum of cosmic rays as a function of zenith and azimuth. Low energy neutrinos ($E \leq 1$ GeV) carry the imprint of geomagnetic effects. The geomagnetic field prevents cosmic rays of low rigidity entering the atmosphere, providing a sort of barrier. This screening effect is lowest at the magnetic poles and highest at the equator. The nuclear component of cosmic rays is positively charged, and this introduces a dependence on the azimuth angle known as the East-West effect. Basically the neutrino flux is highest from the west direction.

8.8 Conventional Flux Models

The conventional flux is quite well understood, with uncertainties dominated by the primary cosmic ray flux and the hadron production models. Four models of conventional neutrino flux have been considered in this work. The difference observed between different spectra turn out not to be relevant for the sake of our analysis (a comparison of the energy distributions is shown in figure 8.10). Here we opt for the Bartol 2006 tables [84], often referred to as a solid, reliable model. This choice is also justified by the fact that the predictions of the Bartol model (as illustrated in figure 8.10) are the most conservative ones, in which the highest number of events at high energy is expected. This is the worst scenario when the aim is to identify the signal of prompt neutrinos, which should top the conventional contribution at the TeV region.

Bartol

The original Bartol model [85] consists of a one dimensional Monte Carlo simulation of the flux of neutrinos and antineutrinos of e and μ flavour pro-

duced by cosmic rays in the atmosphere; however, in this analysis we refer to the later extended three dimensional calculation [86]. A cosmic ray cascade is followed step-by-step and each channel leading to neutrino production is considered; charged pions contribute at low energies and charged kaons enter the game at $\simeq 10^3$ GeV. The composition of the primary cosmic rays is approximated with 80% in the form of free protons and 20% in that of of nucleons bound in nuclei. The primary flux is parameterised as a function of the energy with the "Bartol" fit (by Gaisser, Stanev, Honda and Lipari [85])

$$\phi(E_p) = a \left(E_p + b\, e^{c\sqrt{E_p}} \right)^{-(\gamma+1)}, \tag{8.18}$$

where E_p is the primary energy in GeV/nucleon, and γ the spectral index. The parameters a, b, c, γ are determined from different sets of measurements from balloons and spacecrafts. This parameterisation refers to a minimum point of the solar magnetic cycle; effects of solar modulations can be included to adapt the simulation to the current solar conditions. The authors make use of a non-isothermal atmosphere to convert altitude to depth in grams per squared centimetre, to include explicitly the effects of the geomagnetic cutoff and solar modulations (section 8.7.1) which are relevant for $E_\nu \leq 10$ GeV. Uncertainties on the absolute neutrino fluxes are estimated to be around 15%, are partly ascribed to the primary spectrum composition, as for instance the π^+/π^- ratio, which determines the $\nu/\overline{\nu}$ ratio, and the kaon/pion ratio, which influences the relative abundance of ν_e with respect to ν_μ.

Honda

The Honda model [87] is a three-dimensional calculation which uses DPMJET-III as the hadronic interaction model, with input information from cosmic ray data at balloon altitudes. The atmospheric model used in this calculation is the US-standard 1976 [88], with the Earth approximated as a sphere of radius $R = 6378,180$ km, and the IGRF model for description of the geomagnetic field [113] (improving upon the dipole model). Cosmic rays are simulated following their spectrum (see figure 8.2), tested to pass the geomagnetic barrier, and then propagated through the atmosphere. The primary cosmic ray flux is parameterised by the Bartol fit given in expression (8.18). Neutrinos produced in primary cosmic ray reactions have an energy $E \leq 100$ MeV, due to the rapid energy loss of cosmic radiation after entering the atmosphere. As many detectors are not sensitive at such a low threshold, these contributions are disregarded. The simulation includes existing neutrino detectors placed at their actual geographical location. This model has also been improved with a three-dimensional extension; the differences between the improved 3-dimensional model and the previous 1-dimensional one are the enhancement of low energy events at the horizon. However, there are no remarkable differences at the energies of interest for this work.

Fluka

The latest version of Fluka is described in [90]. It is a three-dimensional model built on an interaction and transport Monte Carlo which includes hadron-hadron, hadron-nucleus, electromagnetic and μ interactions, energy loss by ionization, and low energy neutron multigroup transport and interactions. The atmosphere model used in this simulation is a medium composed of a mixture of N, O and Ar arranged to the standard atmosphere model [88]. Differences due to the latitude are included in the systematics. The Bartol fit (equation 8.18) is used as the primary cosmic ray spectrum. The geomagnetic field is described with the IGRF model [113] (expansion of spherical harmonics). Geomagnetic effects are simulated to reproduce the primary cutoff and the particle bending during shower development. Modifications according to the effective potential corrections in the so called "force fields approximation" are introduced to modify the spectrum including the phase of the solar cycle, adapting the Bartol fit to the actual solar condition. Hadronic interactions are included by an effective QCD Lagrangian at low energy.

Lipari

The Lipari model is described in [91] and is the standard atmospheric flux model used in the AMANDA simulation. In the present work, we altered this value taken from the AMANDA simulation code NUSIM[53], and re-calculated the weight for atmospheric neutrinos according to different models. The Lipari prediction is based on the same production and transport Monte Carlo used in FLUKA. The primary cosmic ray flux is assumed to be uniform and isotropic, and its dependence on the primary energy per nucleon is obtained from the Bartol fit (expression 8.18). Primary particles have their starting point at about 100 kilometres of altitude in the atmosphere, which is modelled here as 51 concentric shells of increasing density. Results for ν_e and ν_μ are provided in [91] with a cosmic ray spectrum at solar minimum and no geomagnetic effects. Correction coefficients are provided to include the effects due to the epoch of solar cycle and the geomagnetic cutoff at the location of the specific detector.

8.9 Prompt Models

The prompt neutrino models investigated here belong to three major classes according to the hadronic interaction model used in the cross section evaluation. Two of them (QGSM, RQPM) are non-perturbative, phenomenological models obtained through numerical methods. Instead, the pQCD calculation is semi-analytical, and is based on NLO QCD. In the present work the simulation is performed, as for conventional models, using the C++ class `neutrinoflux`

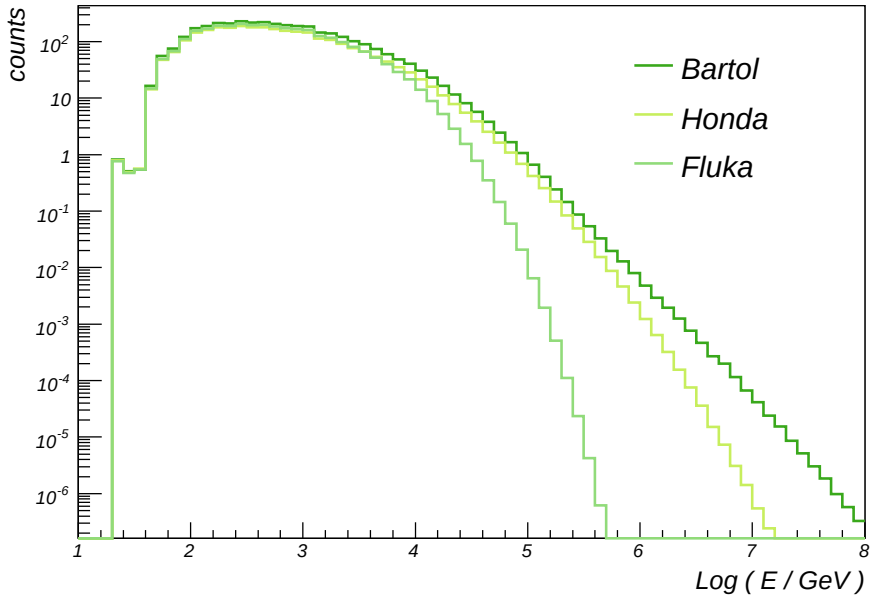

Figure 8.10: Distribution of the Monte Carlo true energy of a neutrino data sample, weighted with three different conventional models. The Bartol prediction (curve on the right) is the one adopted in this analysis for a description of the conventional neutrino background. This choice is motivated by the fact that the Bartol model represents a conservative situation, in which the identification of a prompt signal is the worst-case scenario.

[115]. The fundamental different approaches to the evaluation of the prompt flux are:

- QGSM: *Quark Gluon String Model*, based on a topological $1/n_f$ expansion of QCD diagrams for the elastic process, and is non-perturbative.
- RQPM: *Recombination Quark Parton Model*, phenomenological model with intrinsic charm. The incoming proton contains sea charm from gluon-gluon fusion; based on numerical code, and is non-perturbative.
- pQCD: *Perturbative QCD* at next-to leading order, integrated with PYTHIA, accounting for gluon PDFs only.

Naumov / Recombination Quark Parton Model

The first prompt model examined is the one-dimensional parameterisation described in [96]. Here the cosmic ray composition is approximated with five

types of nuclei (H, He, CNO, Ne-S and Fe). According to the atomic mass, different energy spectra are used for the different elements:

$$\frac{d\Phi}{dE} = \begin{cases} \Phi_A^{(1)} \varepsilon_A^{-\Gamma_A} \text{ for } E < W_A \\ \Phi_A^{(2)} \varepsilon_A^{-\gamma_A} \text{ for } E > W_A \end{cases} \tag{8.19}$$

where E is the energy per nucleon in GeV, A is the atomic mass, and the following relation holds

$$\Gamma_A = \sum_{k=0}^{3} \gamma_A^{(k)} \log^k \varepsilon_A. \tag{8.20}$$

The spectrum is required to be continuous with continuous first derivative at $E = W_A$. All the other parameters remaining are determined from fits to data. Balloon experiments such as BESS and JACEE [97] provide reliable measurements of the hydrogen and helium spectra. The other three classes are modelled assuming that

$$\frac{d\Phi_A}{dE} = c_A \frac{d\Phi_4}{dE} \qquad \text{(A=15, 27, 56 for CNO, Ne-S and Fe).} \tag{8.21}$$

The CORT code [98] is used for transport and nucleon-nucleus interactions. Accelerator data, which refer to protons, have been extended to air nuclei (N, O, Ar, C). A description of the nucleus-nucleus collisions can be achieved with the simplification of the superposition model. Here the collision of a cosmic ray nucleus of energy E_A and atomic number A against an air molecule is approximated as the sum of A independent collisions of nucleons, each with energy E_A/A. This simplification is justified when the energy of the incoming nucleus is much larger than the nucleon binding energy, hence each single nucleon interacts incoherently. In fact, the approximation fails in low energy regions, where the geomagnetic field affects particles according to their rigidity Z/A. In the perspective of describing prompt fluxes, however, the superposition model provides a reliable description. The atmosphere is simulated according to the Dorman isothermal model. Uncertainties in this calculation can be ascribed mainly to the input data providing the nucleus-nucleus cross-sections and the primary spectrum composition. In particular, corrections have been applied to match the relative π^+/π^- abundance to the data (a change of 5-9% in the ratio is observed). Moreover, simplifications have been introduced. Isotopes of the air nuclei have not been accounted, as their contribution to the spectrum contributes with minor changes. The channel $\pi + \text{air} \to \pi + X$ (meson regeneration) has been disregarded; at the energies considered, its contribution is small.

Quark Gluon String Model

The QGSM approach is an alternative to perturbative methods. It is based on an idea by 't Hooft [99], consisting of a theory with local gauge group $U(N)$,

for large N, so as to allow for a perturbative expansion is terms of $1/N$. The inclusive cross section for hadron production is written as a sum of several contributions, given by the interaction vertices contained in a Lagrangian with $U(N)$ invariance. The $1/N$ series is often called topological expansion, and is related to the Euler characteristic of the gauge manifold $2-2g$, with g being the genus[1]. The functional integral

$$Z = \int \mathcal{D}\Phi\, e^{iS[\Phi]}, \qquad \text{with } S = \int d^4x\, \mathcal{L}(x), \tag{8.22}$$

which originates the terms of the perturbative series, can be written in the $N \to \infty$ limit as

$$Z = N^{2-2g} \tag{8.23}$$

Within this approximation, it is possible to evaluate all interaction vertices, and consequently amplitudes of processes involving hadrons, in the low energy limit. In the limit $N \to \infty$, it has been shown that only a certain class of diagrams (i.e. planar diagrams) contribute to the amplitude, whilst the others can be neglected. The QCD potential between partons is approximated at low energies with a linear function of the distance $V = kr$, where k is a constant. Once parameterised the parton-parton potential, PDFs and fragmentation functions can be determined. Fragmentation functions of partons to charmed particles have then been evaluated in this formalism [100]. Parton distribution functions of the constituent quarks are approximated according to the Regge theory. The assumption made here is that the trajectories of $c\bar{c}$ are linear, as is the case for light quarks, which results in a steep longitudinal momentum distribution. The QGSM scheme for hadronic interactions is convoluted with Z-moments calculated numerically, to account for prompt secondary production. Its applicability to QCD, where $N = 3$, is valid in restricted cases. Additionally, the production of D_s is neglected.

Perturbative QCD

The pQCD calculation [101] is obtained with a semi-analytical method which merges next-to-leading order QCD with a Monte Carlo simulation and approximate cascade equations. The production of a charmed hadron of type j from a proton-air collision, occurs with with a probability described by the Z-moment (see 8.6.1)

$$Z_{pj} = 2f_j \int_0^1 \frac{dx_E}{x_E} \frac{\Phi_p(E/x_E)}{\Phi_p(E)} \frac{1}{\sigma_{p-\text{air}}(E)} \frac{d\sigma_{p+\text{air}\to c\bar{c}}(E/x_E)}{dx_E}, \tag{8.24}$$

where f_j is the fragmentation function for the hadron j, and $\sigma_{p-\text{air}}$ the total proton-air cross section. The factor of 2 accounts for both particle and antiparticle production. The following values are used for the charm mass m_c,

[1]The genus is the number of handles, or equivalently, the number of different classes of closed paths which are not continuously deformable into each other.

the factorisation scale M and the renormalisation scale μ:

$$\begin{aligned} m_c &= 1.3 \text{ GeV} \\ M &= 2\, m_c \\ \mu &= m_c. \end{aligned} \tag{8.25}$$

Parton distribution functions are taken either from the CTEQ3 fit, or from the MRSD fit. The prompt lepton flux is calculated at leading order in the matrix element (with the two-loop coupling constant $\alpha_s(\mu^2)$) and convoluted with next-to-leading order PDFs. The next-to-leading order to the matrix element is obtained by rescaling the leading order by a factor K determined from a Monte Carlo method [102]. Lepton fluxes are compared with the results from PYTHIA. The resulting flux is written in the parametric form

$$\log_{10}(E^3\, \Phi_l(E)) = -A + Bx_E + Cx_E^2 - Dx_E^3. \tag{8.26}$$

The prompt flux is isotropic. Because of the short lifetime of charmed hadrons, no substantial differences in the atmospheric density can influence the process. Horizontal and vertical events follow the same decay probability distribution. The main source of uncertainty is the x-dependence of the parton distribution functions. When comparing fluxes obtained with different sets of PDFs, the different predictions deviate at lepton energies around 10^8 GeV. The x range of importance for lepton flux calculations is 10^{-5}, which is well below the last data points provided by HERA. The gluon PDFs dominate, justifying the approximation neglecting the quark PDFs. This argument has been discussed in section (8.3).

8.10 The Model Rejection Factor Technique

The question of isolating a prompt signal belongs to the general problem of identifying one channel out of many, given only a measurement of their sum. Let us suppose we have a signal event in the presence of background. Both signal and background are described by models; let n_s be the expected number of signal events and n_b the expected number of background events. In the measurement n_o events are counted. The model rejection factor [116] is a tool to investigate whether we can exclude a model for the signal at a given confidence level.

The problem of resolving signal from background must rely on some statistical technique. Let us start by assuming that the events we measure belong to the background. If we count n_o events expecting n_b, the 90% confidence belt from the Feldman & Cousin tables provides an interval where the measured value should fall with a 90% probability

$$\mu_{90}(n_o, n_b) = [\cdot\,, \mu_{\max}]. \tag{8.27}$$

The upper limit is the upper edge $\mu_{\max}$ of the interval. This number represents the maximum value that we would observe at 90% confidence level, assuming that our model represents the variable we are measuring. We interpret an excess as the appearance of a signal, described by another model, with n_s expected events. The significance of an excess must be referred to the expected signal counts n_s, as this would give a measure of the possibility of this being the cause. On the other hand, the absence of excess would suggest that the signal is not observed. A model rejection factor is defined as

$$\mathrm{MRF} = \frac{\mu_{\max}}{n_s}. \tag{8.28}$$

A MRF value smaller than 1 implies that the measured counts are consistent with background, and the model for signal can be rejected at 90% confidence level. An upper limit on the flux of signal events can be established on the basis of our observations as

$$\Phi_{90} = \Phi \cdot \mathrm{MRF}. \tag{8.29}$$

The closer the model rejection factor is to 1, the more stringent is the limit that we are able to pose. The aim of resolving signal from background is achieved by placing an optimal threshold, such that background is maximally suppressed by keeping most of the signal. As evident from expression (8.29), the best limit is obtained for the smallest value of MRF. If we perform a measurement of the variable x, with its statistical distribution $f^{(obs)(x)}$ (or $f^{(obs)_i=f(x_i)}$ in case of a discrete case), and the expectation values are described by $f^{(b)}(x)$ for the background, and $f^{(s)}(x)$ for the signal, the partial number of expected events are

$$n = \int_0^{x_T} f(x)\, dx, \tag{8.30}$$

with x_T being the threshold value. $f(x)$ is either $f^{(obs)}(x)$, $f^{(b)}(x)$ or $f^{(s)}(x)$. For each x_T, we evaluate the model rejection factor $MRF(x)$. The minimum value indicates the optimal threshold for distinguishing signal from background. In the framework of a blind analysis, the search for an optimal threshold cannot be based on the observed number of events. The quantity μ_{90}, however, depends on n_o; to be independent of the observation, an average upper limit is defined as

$$\bar{\mu}_{90} = \sum_{n=0}^{\infty} \mu_{90}(n, n_b)\, w(n, n_b), \tag{8.31}$$

with the Poissonian distribution as the weighting function, stating the probability for each value n_b:

$$w(n, n_b) = \frac{(n_b)^n\, e^{-n_b}}{n!}. \tag{8.32}$$

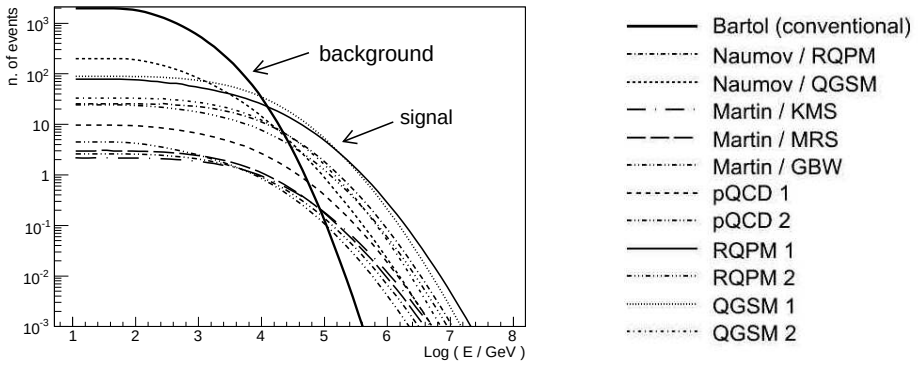

Figure 8.11: Signal and background distributions for various prompt neutrino models, as a function of energy, with background represented by the Bartol conventional model.

The model rejection factor is defined in an analogous way to expression (8.28), as the ratio between the upper limit and the number of expected signal events

$$\mathrm{MRF} = \frac{\bar{\mu}}{n_s} \tag{8.33}$$

from which a limit on the model can be set in the same way as in expression (8.29). In this analysis, we are looking for exclusion potential rather than discovery. The best limit is obtained with the minimum value for the model rejection factor, as a function of the unfolded neutrino energy. The reconstructed energy variable is a good indicator to distinguish between prompt and conventional contributions in the spectrum.
In this analysis we consider the Bartol flux model as the background description and eleven different possibilities for the prompt contributions, as illustrated in figure 8.11.
It is interesting to investigate the functional dependence of MRF on the variable E, to establish if we expect a non-trivial minimum. Since the MRF is defined as a ratio of two functions (8.28) the prime derivative is written as

$$MRF = \frac{f(E)}{g(E)} \Rightarrow MRF' = \frac{1}{g}\, f' - \frac{1}{g^2}\, g'\, f \tag{8.34}$$

The condition of extreme $MRF'(E^*) = 0$ is verified for:

$$MRF' = 0 \Rightarrow \frac{f'}{g'} = \frac{f}{g} \tag{8.35}$$

To find the value E^* for which relation (8.35) is satisfied, we have to make some assumptions on the way f and g depend on E. It is reasonable to describe the

distribution of signal and background events with an exponential law, generally expressed as

$$n_b \sim E^{-\gamma_1} \tag{8.36}$$
$$n_s \sim E^{-\gamma_2}, \tag{8.37}$$

with γ_1, $\gamma_2 \in R$. If n_b represents conventional neutrinos and n_s represents prompt, we can state that $\gamma_1 \simeq \gamma_2 + 1$. For the dependence of the upper limit μ we use the parameterised form

$$\mu \sim a_1 + a_2 \sqrt{n_b} + a_3 n_b + \mathcal{O}(n_b^2). \tag{8.38}$$

The parameters a_i are $\mathcal{O}(1)$. The condition (8.35) is verified when

$$\frac{-\frac{1}{2}\gamma_1 a_2 E^{-\frac{1}{2}\gamma_1 - 1}}{-\gamma_2 E^{-\gamma_2 - 1}} = \frac{a_1 + a_2 E^{-\frac{1}{2}\gamma_1}}{E^{-\gamma_2}}. \tag{8.39}$$

The remaining expression yields

$$E^* = \left(\frac{a_1}{\frac{\gamma_1 a_2}{2\gamma_2} - a_2} \right)^{\frac{2}{\gamma_1}} \tag{8.40}$$

with $\gamma_1 > \gamma_2$. This ensures the existence of an extremal for a finite value E^*, for the case in which signal and background are described by exponential laws. Substituting estimated values for a_1, a_2 and the indices γ, it is possible to show that such value lies inside the regime of interest, namely a non trivial minimum of the model rejection factor exist.

8.11 Unfolding of the Atmospheric Spectrum

Our search for a prompt neutrino signal is based on a reconstructed energy spectrum of AMANDA-II data measured over the four year period 2000-2003, for a total detector livetime of 807 days. As described in chapter 7, unfolding is a reconstruction technique based on information of a simulated data sample to reproduce variables which are cannot be directly measured.
As previously mentioned, neutrinos are not directly detected, but reconstructed from the track of a charged lepton, originating from a charged current scattering process in the ice. Additionally, the muon energy is itself a problematic variable to measure, and has to be reconstructed from some variables correlated to the energy. In short, we are here in the case of reconstructing our unknown variable through a set of quantities correlated with it, measured by a detector with finite acceptance and resolution: a classical problem of unfolding. Three variables showing a correlation with the neutrino energy are chosen by investigating their dependence on the true energy of a Monte Carlo

simulation. As mentioned in chapter 7, $\mathcal{RUN}$ allows the unfolding to be performed with up to three variables that can be used to construct the kernel. The first variable to be intuitively correlated with the energy is the number of hits which compose the event. The motivation for this is that highly energetic leptons emit a large number of Cherenkov photons, illuminating a large part of the detector. The second variable used is the energy estimator obtained with a likelihood function, based on the $P_{\text{hit}}P_{\text{no hit}}$ algorithm, as described in section 4.4.2. For the third variable we consider the zenith angle θ, which goes from 90° to 180° for tracks coming from the Northern hemisphere according to the AMANDA coordinate system. The dependence on the zenith angle is justified with the fact that the number of hit channels depends on the arrival direction of the track, because AMANDA has a cylindrical form with z dimension larger than x and y. The correlation with the Monte Carlo true energy is shown in figure 8.12.

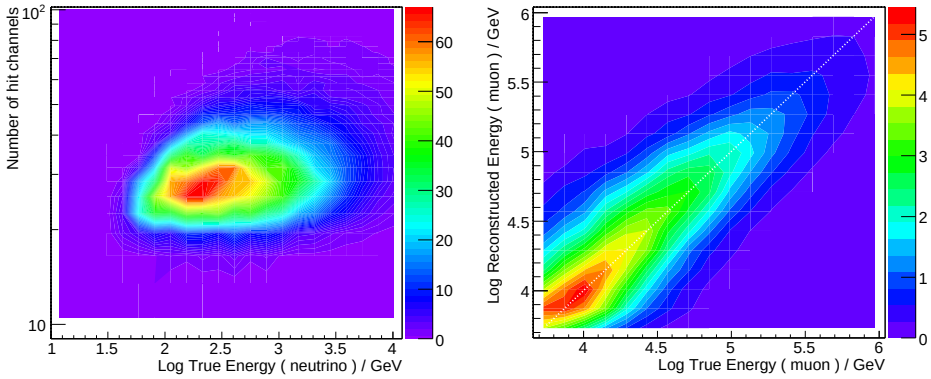

Figure 8.12: Correlation of the true energy of the Monte Carlo simulation with the number of channels (left), and the reconstructed energy (right). The energy estimator from the $P_{\text{hit}}P_{\text{no hit}}$ likelihood has been corrected with a polynomial function [74], to account for the tendency of under-estimating the energy at high values.

A remark must be made about weights. Each simulated event has a weight (namely the atmospheric weight) associated with it, which fits the original E^{-1} spectrum to the atmospheric prediction. This factor $w \in [0, 1]$ is associated with the energy distribution and rescales each entry according to the model chosen. $\mathcal{RUN}$ has a pre-built function taking the problem of weighted events into account. In this case, an additional column of the input and kernel files is filled with the event weights. This case can be generalised to any weight, which allows us to repeat the unfolding process with an E^{-2} spectrum, which is better suited to reconstruction, as its energy dependence is almost flat in the considered region.
The distribution has been regularised to provide a result free of unphysical

oscillations through the introduction of interpolating spline functions (see section 7.5), whose regularisation parameters *degrees of freedom* and *knots* have to be set by the user. As mentioned in chapter 7, a reasonable choice for the number of degrees of freedom is the number of data points. In our case, the input variable is distributed in 10 bins, meaning that we provide 10 data points for the unfolding rule. The result has been proved to remain stable under small variations of the binning, as well as the regularisation parameters. To evaluate the grade of precision for the unfolding process, the covariance matrix is provided as output. The distribution of χ^2 probabilities obtained with simulation is shown in figure 8.16; a flat distribution is the indicator of a successful reconstruction.

8.12 Results

8.12.1 Unfolding of Monoenergetic Bins

In order to check that the distribution reconstructed through the unfolding technique provides a reliable result, we prove that a general kernel can unfold a distribution localised in a fixed energy region. For this purpose we produced data samples containing events localised in a single energy bin; the true energy distribution is shown in figure 8.13 bin by bin. The unfolding process is repeated for each bin with regularisation parameters NRDF = 5, KNOTS = 12; we expect the unfolded points to distribute with Gaussian shape around the central value. The correlation between the mean value of the Gaussian $\langle E \rangle$ and the true values is shown in figure 8.14, with a linear fit interpolating the point. The best fit is given by

$$f(x) = ax + b \text{ with } a = 0.90 \pm 0.01 \text{ and } b = 0.466 \pm 0.07$$

An estimate of the detector energy resolution is obtained from the spread of the unfolded points around the central value. We report in figure 8.15 the value of the width σ of the Gaussian curve as a function of the true energy, with values between 0,3 and 0,4 in $\log E$.

8.12.2 Unfolding of the Energy Spectrum

First we unfolded a simulated sample, to compare it with the distribution of the true variable. The atmospheric flux is reproduced with a spectral index $\gamma = 3,7$ (see figure 8.17). This has been repeated for the case of a spectral shape $\Phi \propto \mathrm{E}^{-2}$ (see figure 8.18). The result is stable and reproduces the true distribution. The covariance histogram shown in figure 8.16 looks quite uniform, implying that the regularisation procedure was successful without introducing any bias. The result achieved with a Monte Carlo simulated sample allows us to find an optimal combination of the unfolding parameters degrees of freedom and knots. The values of these parameters are set by this

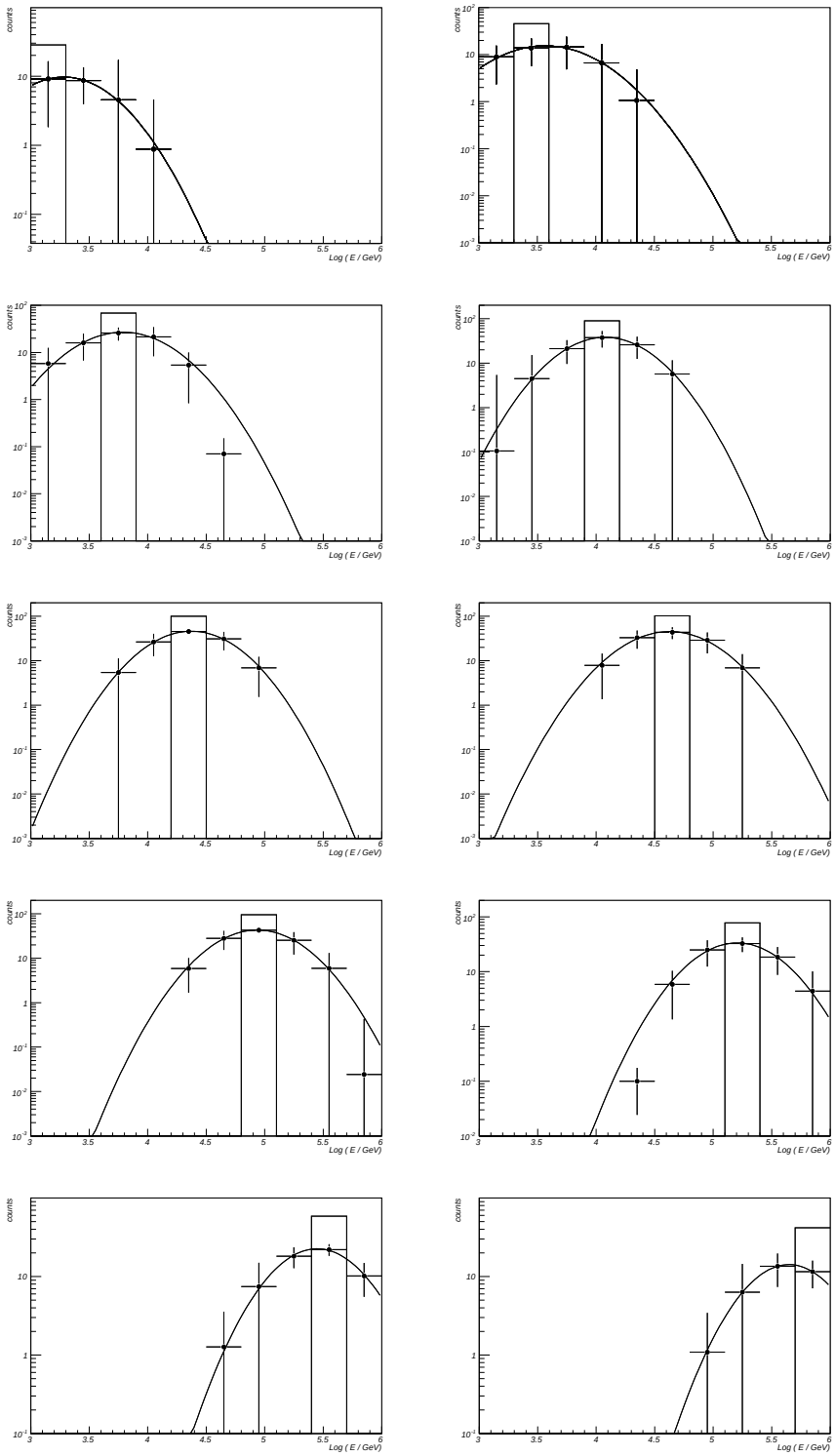

Figure 8.13: Data belonging to monoenergetic bins in the true energy distribution (histogram) with unfolded points. The points are Gaussian distributed around the central value. The width of the Gaussian gives a measure of the energy resolution (see figure 8.15)

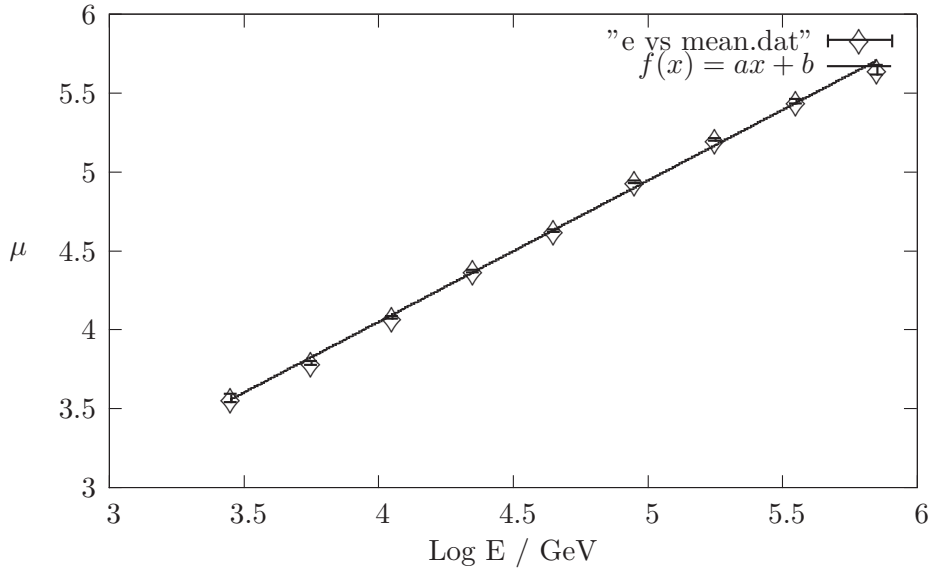

Figure 8.14: True versus reconstructed energy, obtained unfolding monoenergetic bins. The reconstructed value for each bin is represented by the mean value of the Gaussian curve interpolating the unfolded points, as shown in figure 8.13

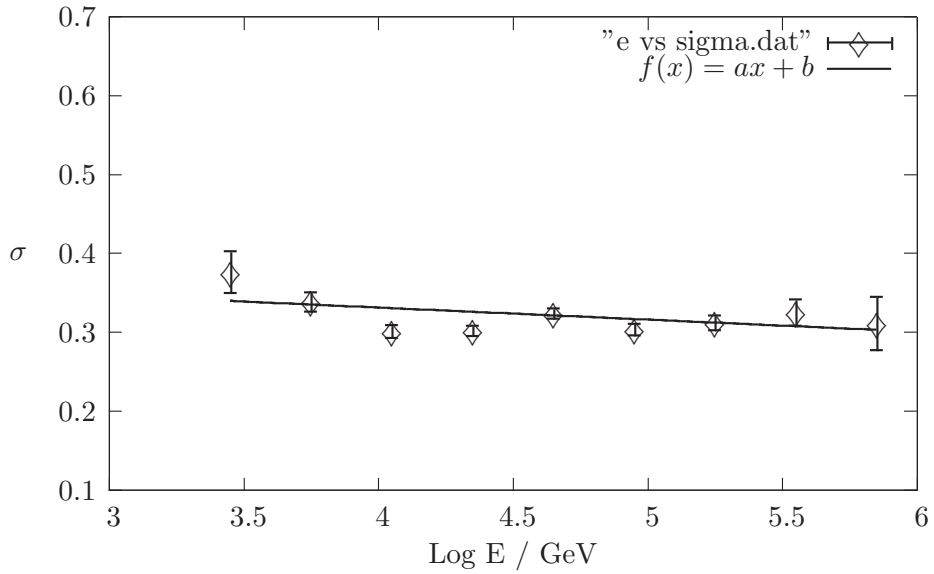

Figure 8.15: Detector resolution, obtained from the width of the Gaussian curve interpolating unfolded points (figure 8.13). The values lay between 0.3 and 0.4 in $\log E$

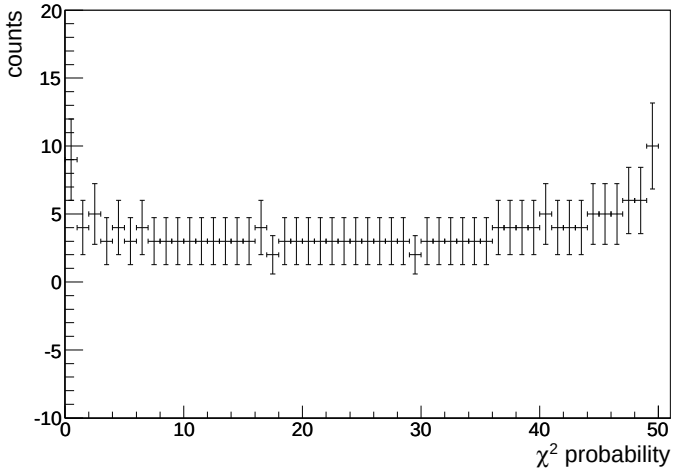

Figure 8.16: Probability distribution of an unfolding with 10 bins in energy. This histogram is automatically generated by $\mathcal{RUN}$ and allows for an estimate of the success of the unfolding procedure. A flat or almost flat distribution identifies a succesful regularisation process.

method. We apply the unfolding algorithm to the real data sample. To observe the blindness criteria of AMANDA analyses, a subset of data containing 20% of the total events is investigated. The unfolded distribution is reported in figures 8.19 and 8.21, together with the prediction from the Bartol conventional model (filled histogram), and three different charm production models added to the conventional one.

8.12.3 Test of Prompt Production Models: Results

The model rejection factor, defined in expression (8.28), has been evaluated for each of the prompt production models examined in order to set upper limits on the expected flux of prompt neutrinos. A selection threshold to disentangle a possible prompt signal from atmospheric background has been established on the basis of a Monte Carlo simulation, replacing the upper limit μ with the average upper limit $\bar{\mu}$, as defined in expression (8.31) and motivated in section 8.10. In this way, the choice of an optimal threshold does not depend on the number of observed events in the data n_o. The minimum value of the model rejection factor indicates the optimal energy region to separate signal from background. The model rejection factor obtained from simulation is shown in figure 8.20; it can be seen that the function has a minimum in the central region of the spectrum. In this figure we have included three models out of the many available, selecting the following criteria: an extreme prediction obtained with the QGSM model, a medium one from the Naumov/RQPM, and a moderate one from the pQCD formalism. These models are also represen-

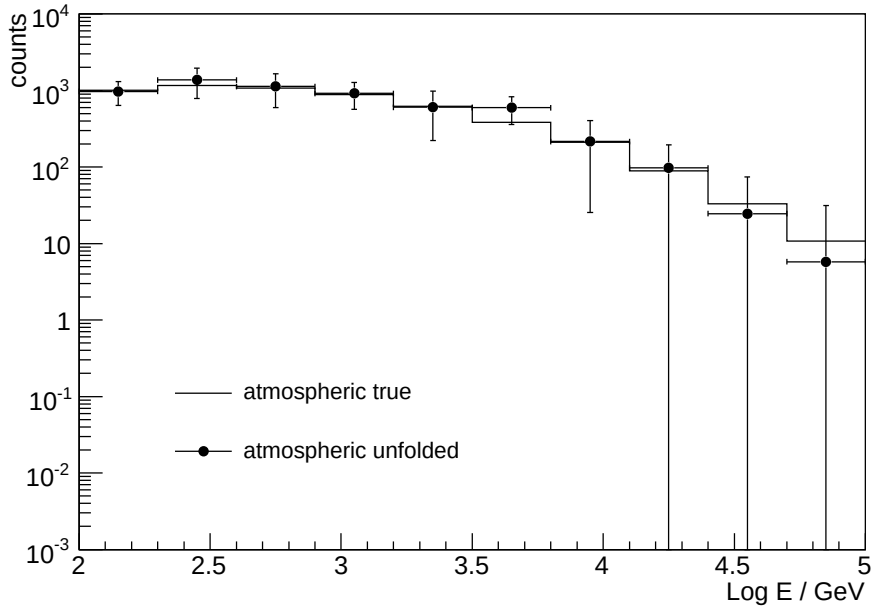

Figure 8.17: Simulated atmospheric spectrum unfolded with three variables. The points and lines represent the reconstructed values and the true distribution respectively.

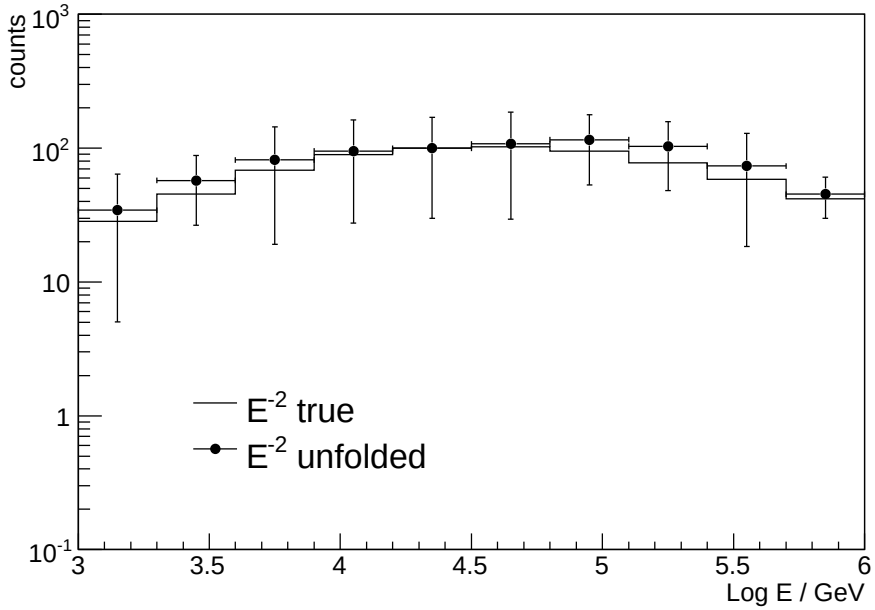

Figure 8.18: Simulated spectrum with E^{-2} dependence, unfolded with three variables. The points and lines represent the reconstructed values and the true distribution respectively.

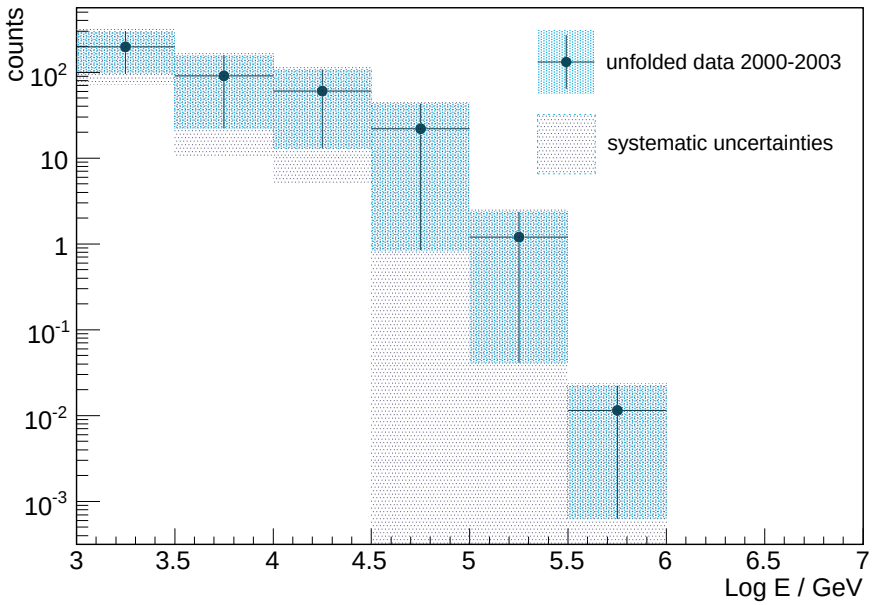

Figure 8.19: The unfolded energy spectrum obtained with the AMANDA-II data over a four year time period (2000-2003). The band represents the uncertainties on the unfolded points, as obtained from the unfolding algorithm

tative of three different hadron interactions models. After this step, we look at the reconstructed distribution of the real data obtained through unfolding. We expect the model rejection factor to have a minimum in the energy region where the signal-to-background ratio becomes optimal. The number of real data events is obtained as the integral of the curve starting from the critical energy

$$n_{\mathrm{obs}}(E > E_c) = \int_{E_c}^{\infty} f(E)\, dE \tag{8.41}$$

where f is the statistical distribution function of E. The values obtained are reported in table (8.22). Basing our criterium on the model rejection factor, we are able to state that the QGSM model seems to be disfavoured at 90% confidence level, but not yet accounted for systematic errors. On the basis of our observations, upper limits can be set on pQCD and Naumov / RQPM, which cannot be excluded as of yet. Those limits are obtained as:

$$\begin{aligned} \Phi_{90}^{\mathrm{pQCD}} &= 8.8 \cdot \Phi^{\mathrm{pQCD}} \\ \Phi_{90}^{\mathrm{Naumov/RQPM}} &= 2.2 \cdot \Phi^{\mathrm{Naumov/RQPM}} \end{aligned} \tag{8.42}$$

The upper limit obtained for the pQCD and Naumov/RQPM model is shown in figure 8.23. To convert the number of observed events into a flux, we use

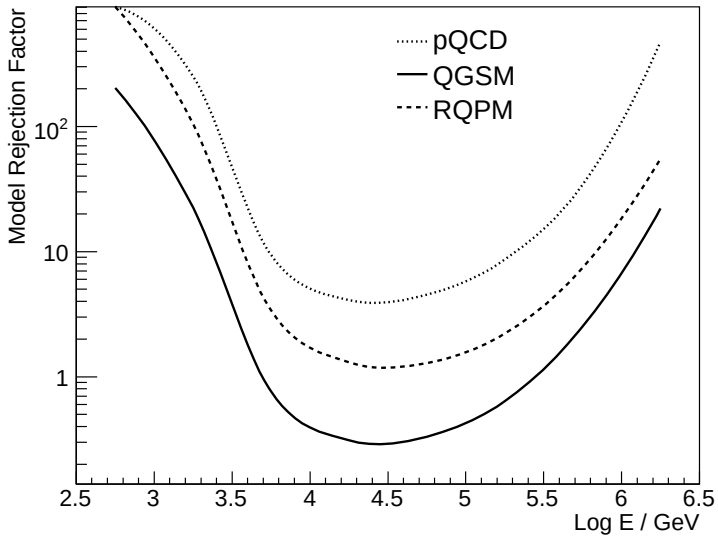

Figure 8.20: Model rejection factor obtained from three models accounting for prompt production. Background is provided by the Bartol conventional flux.

the relation

$$n_{\rm obs} = \int dE \, \frac{d\Phi_\nu}{dE} \, A_{\rm eff} \, t \tag{8.43}$$

This relation includes the effective area obtained in section 6.5, which is energy-dependent. Such an integral equation can be solved discretely as our input value is a binned distribution. The flux (differential in energy) is obtained as

$$\left(\frac{d\Phi_\nu}{dE} \right)_{(i)} = \frac{1}{\Delta E_i} \, n_i \, \frac{1}{A_{\rm eff}(E_i)}. \tag{8.44}$$

The unfolded spectrum, compared with an atmospheric model including prompt, is shown is figure 8.24.

8.13 Theoretical and Systematic Uncertainties

In the evaluation of the contribution of prompt neutrinos, it is fundamental to have a good understanding of the theoretical and systematics uncertainties affecting the measurement. Our current non-observation of prompt neutrinos is used to set an upper limit on the flux of such particles, that can be improved upon with a higher statistics of events allowing for rejection of those models lying near the exclusion threshold

The theoretical uncertainties affecting the calculation of the neutrino flux can be grouped in the following classes, one general group affecting the

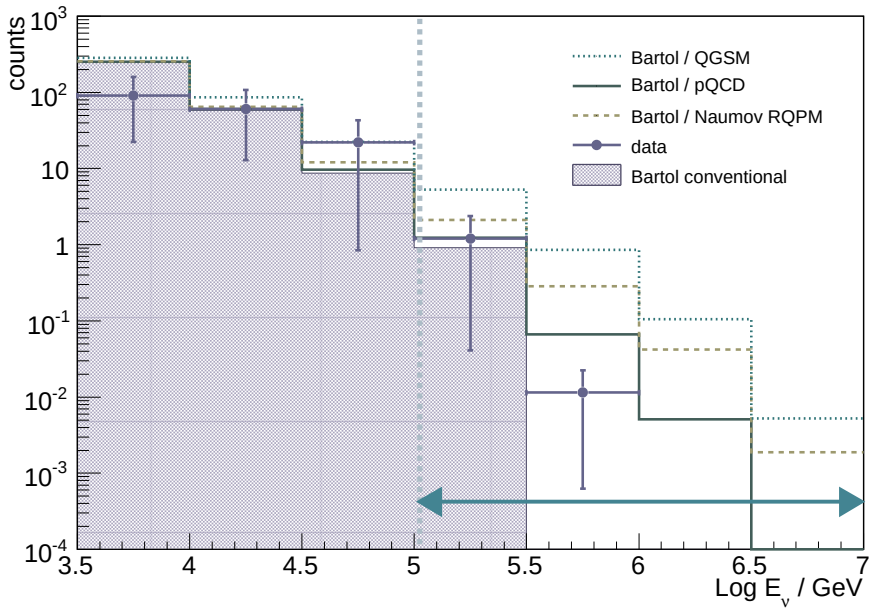

Figure 8.21: The unfolded energy spectrum obtained with the AMANDA-II data over a four year time period (2000-2003). Points represent the unfolded distribution. The filled histogram is the prediction based on the Bartol 2006 model. Three different prompt production models are shown with coloured lines: QGSM, Naumov/RQPM and pQCD

Model	Background events	Data events	Signal events	MRF
Bartol / QGSM	0.92	1.22	5.3	0.65
Bartol / pQCD	0.92	1.22	0.39	8.8
Bartol / Naumov RQPM	0.92	1.22	1.5	2.2

Figure 8.22: Model rejection factors obtained by the comparison of unfolded data with three different prompt production models. The value obtained for the Bartol / QGSM prediction is smaller than 1, allowing for the rejection of this model at 90% confidence level, based on the Feldman and Cousins tables. Upper limits can be set on the other models, with strength proportional to the value of the model rejection factor

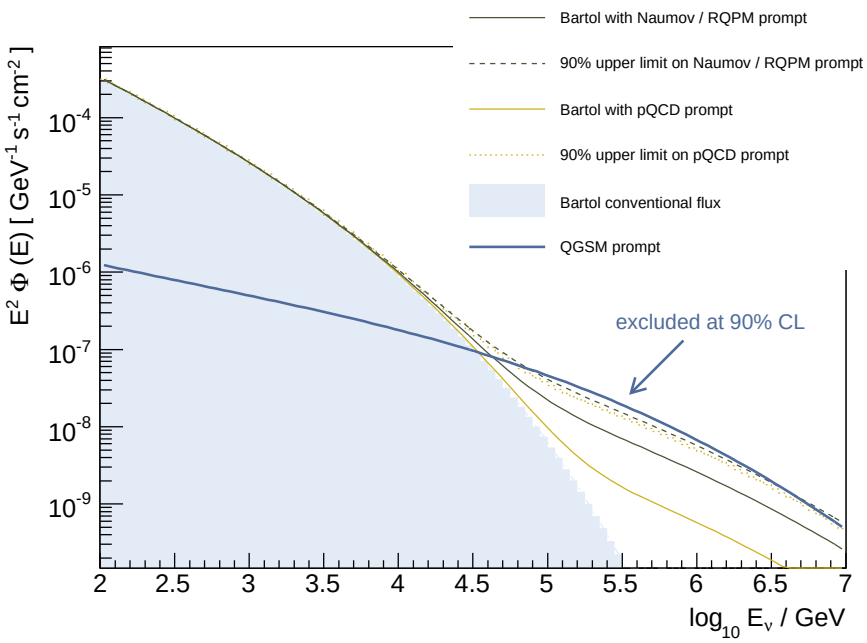

Figure 8.23: Upper limits at 90% confidence level obtained for the pQCD and Naumov/RQPM model. The dashed lines represent the AMANDA upper limits based on the events observed over a four year period; the continuous lines represent the expectations from the two flux models. The background of conventional neutrino contributions is simulated according to the Bartol prediction. Neither of the two model has been excluded on the basis of the current observation.

conventional flux calculation, and one second group regarding in particular the prompt models. Those last show a larger theoretical error, due to the many uncertainties in the evaluation of the deep inelastic QCD process leading to heavy quark production. In particular, uncertainties on the PDFs and fragmentation functions dominate.

As to systematics, they are basically of two types: those dependent on the detector itself and to the propagation medium in which the detector is embedded. We refer to a reference value for the latter, that has been estimated with a Monte Carlo simulation of the ice. In this thesis, the acceptance of the detector photomultiplier has been evaluated with a method based on the photon hit probability 4.4.2.

1. Uncertainties related to the conventional spectrum

Cosmic ray spectrum

Uncertainties in the cosmic ray spectrum depend both on the slope

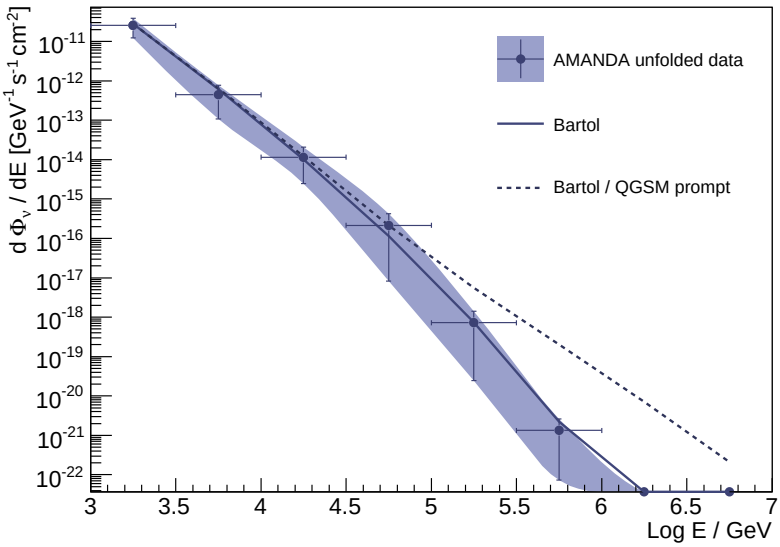

Figure 8.24: The unfolded atmospheric neutrino flux obtained with data taken over a four year time period (2000-2003). The energy distribution has been convoluted with the detector effective area and the total data taking time (807 days) to obtain the reconstructed flux. The points represent our measured data, with error band from the unfolding algorithm. The continuous line is the Bartol conventional flux prediction. The dashed line represents the Bartol conventional flux with addition of an extreme prompt production model (QGSM). Such model has been excluded at 90% C.L.

and the absolute normalisation; Ref. [82] reports an overall uncertainty going from 15% at lower energies, up to 30% at higher energies.

Atmospheric Model

A description of the atmosphere in its details in technically difficult to achieve; however, cross-checks have been done with different models. This source of error does not largely affect the neutrino flux calculation. Average values are used, as neutrinos detected at neutrino telescopes are produced with equal probability in the atmosphere around the Earth. The amount of uncertainty due to the atmospheric model should remain constrained to $\mathcal{O}(1\%)$.

Hadronic interaction model

This is probably a large source of uncertainties in the whole calculation. The fact that QCD is a non-perturbative theory at low energies makes it necessary to use some approximations in describing the quark potential in mesons and baryons. Neutrino flux models

make use of different numerical solutions. The Bartol calculation, used in this thesis for the conventional background description, is based on the TARGET code. The differences between various codes have been examined. Uncertainties ascribed to this source amount to $\mathcal{O}(10\%)$ for the conventional fluxes, going up to a maximum of 20% for high energies. Beside this, further assumption on the heavy quark production model are made for the prompt calculation. As to that, we summarise the main uncertainties into two groups: the PDFs and the fragmentation functions.

PDFs

Parton distribution functions are extrapolated at high Q^2 and low x from fit on experimental data. In a semi-perturbative framework, an assumption is made on the analytical form of the PDFs. In particular, the main contribution is represented by the gluon density, whilst quark PDFs can be neglected at small x. The DGLAP evolution equation is used to continue the functions in the region where no data are available. The uncertainties on PDFs depend on the energy of the process, and have been estimated between 2 and 3% [109].

Fragmentation functions

Heavy flavour production has been investigated at colliders. The function describing the transition of quarks to hadrons can be evaluated in different formalisms, according to the scheme chosen to describe parton potential. We mentioned in this thesis two numerical phenomenological approaches (RQPM and QGSM) and a semi-analytical one (pQCD). An overall estimate, including both PDFs and renormalisation and factorisation scales, give a fluctuation of the order of 20% [119].

2. **Systematic uncertainties related to the detector**

Acceptance of the optical modules

The detector acceptance has been estimated in chapter 6. We used a geometrical method based on the photon hit probability. Our data are compared with a varied efficiency Monte Carlo simulation to estrapolate the acceptance of the optical modules. The value obtained with this method is 95%, with respect to nominal acceptance. We estimate therefore a 5% systematic error ascribed to the loss in the detector acceptance.

Ice Model

The propagation medium must be correctly understood to interpret the detector response. A considerable effort has been made in the AMANDA collaboration to produce an optimal simulation of the

South Pole glacier optical properties. In particular, the presence of dust layers distorts unequivocally the measurement of a lepton track. The systematic uncertainties due to our description of the ice are estimated to 12% [117].

Detector Calibration

Changes in the status of the detector and of the data acquisition system can give contribution to the error on the measurement of a lepton track. An overall uncertainty of 5% has been estimated due to effects of geometrical variations and changes in the trigger[74].

Source of uncertainties	Estimate
Primary cosmic ray spectrum	15% to 30%
Atmospheric model	$\mathcal{O}(1)$%
Parton Distribution Functions	1% to 5%
Hadronic Interaction Model	10% to 20%
Fragmentation functions	$\mathcal{O}(10)$%
OM efficiency	5%
Ice Model	12%
Detector setting	5%

Table 8.2: Uncertainties affecting the neutrino flux calculation. The first group represents the theoretical errors and the second the systematic uncertainties on our measurements.

Considering the definition of the model rejection factor given in expression (8.28), it is reasonable to assume that the theoretical uncertainties of the model will simplify in the ratio. Our systematics are estimated to 14%, which we add as a shift to the error bars provided by the unfolding algorithm, as shown in figure 8.19.

The possibilities of constraining, through our upper limits on prompt neutrino fluxes, the QCD process for hadron production is strongly limited by theoretical uncertainties. Besides this, it is difficult to disentangle those effects due to the models for the primary cosmic ray and the atmosphere from the cross section parameterisation. The relation between the flux of cosmic ray particles and neutrino-induced leptons detected is given in expression (8.8). A precise knowledge of the properties of the atmosphere, as well as the Z-momenta for secondary creation, would allow to transfer the limit on observed neutrino flux on a limit on the PDF and fragmentation function parameterisation.

Conclusions

In this thesis we presented and discussed results achieved in the search for prompt neutrinos with the AMANDA-II neutrino detector. The search for prompt neutrinos is motivated by the enormous interest which raised about the possibility of detecting celestial neutrinos from extra-galactic regions. Such particles could be messengers from environments otherwise impossible to access. Consequently, it is important to have a good understanding of the complete atmospheric spectrum, as it forms the background to an astrophysical signal. The flux of neutrinos from heavy quark hadron decays becomes relevant at energies beyond 10^4 GeV, exceeding the expected flux of conventional particles. This enhancement in the high energy region creates an annoying background to all the searches for high energetic events of cosmic origin. The extremely low rate expected for cosmic neutrinos requires a very accurate description of the high energy atmospheric contributions from prompt particles. In this work, we use a simulated information of the spectra of prompt neutrinos to disentangle them from the conventional spectrum (i.e. from light quark). The simulated prompt spectra are based on several prompt production models, and have been convoluted with the AMANDA detector response to be compared with data. Our data consist of atmospheric neutrino events recorded by the AMANDA-II detector in the deep Antarctic ice. The detection principle, as well as the functioning of the data acquisition system, are described in chapter 2.

Neutrino-induced events have been reconstructed in several steps and accurately selected to ensure a maximal background suppression. Background is represented in our case both by physical events, i.e. leptons originating in cosmic ray showers, and by electronic artefacts of the detector. A pre-selection and reconstruction is performed in Zeuthen. The reconstruction algorithm which have been applied to the raw data are described in chapter 4. The same algorithms are applied to simulated data, obtained with a Monte Carlo method described in chapter 3. All filter conditions to obtain a clean sample of atmospheric neutrino events are described in the same chapter.

In chapter 5, the specific selection of data used for this analysis is presented. We chose some parameters of the neutrino tracks which allow for an identification of good events, and establish appropriate selection condition by matching our data with a Monte Carlo simulation. To preserve the AMANDA

blindness policy, we optimised our selection on a subsample containing 20% of the total data. After the final selection, our data consist of about $4 \cdot 10^3$ atmospheric neutrinos, recorded over 807 days of detector livetime. The track reconstruction has been achieved with a likelihood-based algorithm, built on the geometrical photon detection probability.

The energy spectrum of our data was then reconstructed with a numerical unfolding technique. The determination of neutrino energy is not straightforward in AMANDA; a good indicator for it lies in the number of photomultiplier composing each event, which can be used to feed a likelihood-based algorithm. However, a correction has to be done, as muon tracks traverse and exit the detector, part of the light can be deposited outside the instrumented volume, causing a tendency of underestimating values in the high energy region.

Unfolding seems to be a suitable technique to reconstruct the neutrino energy. In this work we use a FORTRAN numerical method [76] based on a Monte Carlo simulation. The reconstruction is based on three input variables correlated with the true neutrino energy: the number of hits, the energy estimator constructed with the photon detection likelihood (see section 4.4.2) and the declination angle of the track. The main oddity of the unfolding problem is that, form a mathematical point of view, it does not have a well defined a solution, although a numerical approach is possible. A regularisation term is introduced to ensure that the result is free from unphysical oscillations, typical of this kind of reconstructions. All those issues are described from a theoretical point of view in chapter 7.

In chapter 8, the results achieved with this work are presented. The neutrino energy spectrum has been unfolded and reconstructed. We performed some checks to verify the stability of our unfolded result. A convolution with the neutrino effective area allows for extrapolation of the measured flux of events. The atmospheric spectrum has been investigated, in order to isolate the main differences between prompt production schemes [96, 100, 101]. The resulting simulated energy spectrum is illustrated in this chapter for the different models considered. We altered the weighting parameter in the AMANDA simulation software NUSIM, to adjust the spectral shape according to the different models. All input information on which the models are based are described. The choice of set of parton distribution functions, as well as the fragmentation functions describing the hadronisation of the quark pair, is crucial to quantify the prompt neutrino flux. As collider data cannot provide any point in the region of interest (high Q^2 and small x), an extrapolation is needed. The different assumptions result in large differences in the prompt flux at energies beyond 10^5 GeV.

A comparison between the unfolded energy spectrum and different models including prompt contributions has been achieved. The model rejection factor technique has been used to evaluate the significance of an excess in the high energy region. The optimal threshold in energy to distinguish prompt

contributions from conventional background has been identified minimising the model rejection factor as a function of the energy. The minimum value gives the most stringent limit. For the description of conventional background, we rely on the Bartol 2006 tables, which represent in our case the conservative scenario, in which they show the highest prediction of conventional events in the high energy region with respect with other conventional models considered (Honda, Fluka, Lipari).

The prompt production schemes considered belong to the three main categories of RQPM (recombination quark parton model), QGSM (quark-gluon string model) and pQCD (perturbative QCD).

The model rejection factor technique allows for the exclusion of the QGSM model at 90% confidence level. Upper limits have been set on the expected flux predictions, based on our observation:

$$\begin{aligned} \Phi_{90}^{\mathrm{pQCD}} &= 8.8 \cdot \Phi^{\mathrm{pQCD}} \\ \Phi_{90}^{\mathrm{Naumov/RQPM}} &= 2.2 \cdot \Phi^{\mathrm{Naumov/RQPM}} \end{aligned}$$

Systematic and theoretical uncertainties have been considered. The acceptance of the AMANDA photomultipliers has been evaluated in chapter 6 with a method based on the geometrical photon detection probability, with comparison with a Monte Carlo simulation of varied efficiency respect to the nominal value. The uncertainties ascribed to the ice structure have been taken from a standard reference value used in AMANDA. Theoretical errors are the largest source of uncertainty in the evaluation of the prompt and conventional neutrino flux. In the evaluation of the model rejection factor, however, it is a reasonable assumption that the theoretical uncertainties cancel out. Theoretical errors are dominated by uncertainties on the parton distribution functions extrapolated at high Q^2 and low x.

There is a chance that the next generation of large neutrino telescopes will provide evidence of both prompt and extraterrestrial neutrinos. If this will not be the case, the large statistics collected will allow for more stringent limits on the flux of these events, and possible exclusion of other models.

An interesting extension of the results achieved is the extrapolation of the upper limit of the flux of prompt neutrinos to the deep inelastic cross section for $pN \to q\bar{q} \to$ hadrons. The energy region that can be reached by cosmic rays offers a unique opportunity to collect data where no information from colliders will be available in the near future.

Appendix A

Reconstruction Fits

Here the reconstruction fits on the Mainz data selection are listed. For likelihood-based algorithms, the fit seed is written in the last column.

LEVEL	NAME	SEED
L1		
FIT 0	Direct Walk	
FIT 1	Direct WIMP	
FIT 2	CFirst	
FIT 3	JAMS	
FIT 4	Pandel 1-fold	JAMS(3)
FIT 5	Cascade likelihood SPE	CFirst(2)
FIT 6	Cascade likelihood MPE	SPE(5)
L2		
FIT 7	Pandel 32-fold	
FIT 8	16-fold Pandel MPE likelihood	Pandel 1-fold(4)
FIT 9	16-folded Bayes likelihood	Pandel 1-fold(4)
FIT 10	16-fold Pandel Point Source likelihood	CFirst(2)
L3		
FIT 11	Paraboloid Pandel	32-Pandel(7)
FIT 12	64-folded Bayes likelihood	32-Pandel(7)
L4		
FIT 13	1-folded Pandel likelihood	64-Bayes(12)
FIT 14	PhitPnohit likelihood fit	32-Pandel(7)
FIT 15	Paraboloid fit	
L5		
FIT 16	32-fold Pandel likelihood	32-Pandel(7)
FIT 17	0- Pandel likelihood	32-Pandel(16)
FIT 18	0- Bayes likelihood	64-Bayes(12)
L6		
FIT 19	PhitPnohit likelihood fit	PhitPnohit(14)
FIT 20	Paraboloid fit	PhitPnohit(19)

Bibliography

[1] W. Pauli, "Dear radioactive ladies and gentlemen," Phys. Today **31N9** (1978) 27.

[2] F. Reines and C. L. Cowan, "The neutrino," Nature **178** (1956) 446.

[3] G. Danby, J. M. Gaillard, K. Goulianos, L. M. Lederman, N. B. Mistry, M. Schwartz and J. Steinberger, "Observation of high-energy neutrino reactions and the existence of two kinds of neutrinos," Phys. Rev. Lett. **9** (1962) 36.

[4] Leon Lederman & Dick Teresi "The God Particle", Houghton Mifflin Company, New York 1993

[5] T. D. Lee and C. N. Yang, "Question Of Parity Conservation In Weak Interactions," Phys. Rev. **104** (1956) 254.

[6] R. L. Garwin, L. M. Lederman and M. Weinrich, "Observations of the Failure of Conservation of Parity and Charge Conjugation in Meson Decays: The Magnetic Moment of the Free Muon," Phys. Rev. **105** (1957) 1415.

[7] C. S. Wu, E. Ambler, R. W. Hayward, D. D. Hoppes and R. P. Hudson, "EXPERIMENTAL TEST OF PARITY CONSERVATION IN BETA DECAY," Phys. Rev. **105** (1957) 1413.

[8] R. N. Mohapatra, Palash B. Pal "Massive Neutrinos in Physics and Astrophysics ", Third Edition, World Scientific Lecture Notes in Physics, Vol. 72

[9] Y. Fukuda *et al.* [Super-Kamiokande Collaboration], "Measurement of the flux and zenith-angle distribution of upward through-going muons by Super-Kamiokande," Phys. Rev. Lett. **82** (1999) 2644 [arXiv:hep-ex/9812014].

[10] K. Eguchi *et al.* [KamLAND Collaboration], "First results from KamLAND: Evidence for reactor anti-neutrino disappearance," Phys. Rev. Lett. **90** (2003) 021802 [arXiv:hep-ex/0212021].

[11] C. Kraus *et al.*, "Final results from phase II of the Mainz neutrino mass search in tritium beta decay," Eur. Phys. J. C **40** (2005) 447 [arXiv:hep-ex/0412056].

[12] S. M. Bilenky and B. Pontecorvo, "Discussion Of The Solar Neutrino Problem In The Light Of Reactor Neutrino Oscillation Experiments," Sov. J. Nucl. Phys. **43** (1986) 786 [Yad. Fiz. **43** (1986) 1225].

[13] K. Martens [Super-Kamiokande Collaboration], "The current status of the Super-Kamiokande experiment," *Prepared for The 25th INS International Symposium on Nuclear and Particle Physics with High-Intensity Proton Accelerators, Tokyo, Japan, 3-6 Dec 1996*

[14] J. Boger *et al.* [SNO Collaboration], "The Sudbury Neutrino Observatory," Nucl. Instrum. Meth. A **449** (2000) 172 [arXiv:nucl-ex/9910016].

[15] E. Aslanides *et al.* [ANTARES Collaboration], "A deep sea telescope for high energy neutrinos," arXiv:astro-ph/9907432.

[16] V. A. Balkanov *et al.* [BAIKAL Collaboration], "The Lake Baikal neutrino experiment," Nucl. Phys. Proc. Suppl. **87** (2000) 405 [arXiv:astro-ph/0001145].

[17] G. Riccobene [NEMO Collaboration], "First Results From The Nemo Test Site," J. Phys. Conf. Ser. **81** (2007) 012013.

[18] G. Aggouras *et al.* [NESTOR Collaboration], "Recent results from NESTOR," Nucl. Instrum. Meth. A **567** (2006) 452.

[19] F. Ardellier *et al.* [Double Chooz Collaboration], "Double Chooz: A search for the neutrino mixing angle theta(13)," arXiv:hep-ex/0606025.

[20] D. G. Michael *et al.* [MINOS Collaboration], "Observation of muon neutrino disappearance with the MINOS detectors and the NuMI neutrino beam," Phys. Rev. Lett. **97** (2006) 191801 [arXiv:hep-ex/0607088].

[21] C. Gustavino [OPERA Collaboration], "The OPERA experiment," J. Phys. Conf. Ser. **39** (2006) 326.

[22] P. F. Loverre [K2K and T2K Collaborations], "K2K and T2K," J. Phys. Conf. Ser. **39** (2006) 323.

[23] K. Hirata *et al.* [KAMIOKANDE-II Collaboration], "Observation Of A Neutrino Burst From The Supernova Sn 1987a," Phys. Rev. Lett. **58** (1987) 1490.

[24] :. F. Aharonian [HESS Collaboration], "Discovery of a VHE gamma-ray source coincident with the supernova remnant CTB 37A," arXiv:0803.0702 [astro-ph].

[25] A. Letessier-Selvon, X. Bertou, O. Deligny and C. Lachaud [Pierre Auger Collaboration], "Neutrino Sensitivity And Background Rejection Of The Auger Observatory," *Prepared for 27th International Cosmic Ray Conference (ICRC 2001), Hamburg, Germany, 7-15 Aug 2001*

[26] K. Hoffman [AURA Collaboration], "Aura: The Askaryan Underice Radio Array," J. Phys. Conf. Ser. **81** (2007) 012022.

[27] I. Kravchenko *et al.* [RICE Collaboration], "Performance and simulation of the RICE detector," Astropart. Phys. **19** (2003) 15 [arXiv:astro-ph/0112372].

[28] S. Boser *et al.*, "Feasibility of acoustic neutrino detection in ice: First results from the South Pole Acoustic Test Setup (SPATS)," arXiv:0708.2089 [astro-ph].

[29] B. A. Majorovits [GERDA Collaboration], "The GERDA neutrinoless double beta-decay experiment," AIP Conf. Proc. **942** (2007) 57.

[30] D. Y. Stewart [COBRA Collaboration], "The COBRA double-beta decay experiment," Nucl. Instrum. Meth. A **580** (2007) 342.

[31] H. V. Klapdor-Kleingrothaus [Heidelberg-Moscow Collaboration], "The Heidelberg-Moscow double beta decay experiment with enriched Ge-76: First results," Nucl. Phys. Proc. Suppl. **28A** (1992) 207.

[32] T. Totani and K. Sato, "Spectrum Of The Relic Neutrino Background From Past Supernovae And Cosmological Models," Astropart. Phys. **3** (1995) 367 [arXiv:astro-ph/9504015].

[33] N. Kaiser and G. Squires, "Mapping the dark matter with weak gravitational lensing," Astrophys. J. **404** (1993) 441.

[34] C. Amsler *et al.* [Particle Data Group], "Review of particle physics," Phys. Lett. B **667** (2008) 1.

[35] M. Beuthe, "Oscillations of neutrinos and mesons in quantum field theory," Phys. Rept. **375** (2003) 105 [arXiv:hep-ph/0109119].

[36] L. A. Anchordoqui, J. L. Feng, H. Goldberg and A. D. Shapere, "Black holes from cosmic rays: Probes of extra dimensions and new limits on TeV-scale gravity," Phys. Rev. D **65** (2002) 124027 [arXiv:hep-ph/0112247].

[37] D. Hooper, D. Morgan and E. Winstanley, "Lorentz and CPT invariance violation in high-energy neutrinos," Phys. Rev. D **72** (2005) 065009 [arXiv:hep-ph/0506091].

[38] N. E. Mavromatos, A. Meregaglia, A. Rubbia, A. Sakharov and S. Sarkar, "Quantum-Gravity Decoherence Effects in Neutrino Oscillations: Expected Constraints From CNGS and J-PARC," Phys. Rev. D **77** (2008) 053014 [arXiv:0801.0872 [hep-ph]].

[39] N. E. Mavromatos and S. Sarkar, "Probing Models Of Quantum Decoherence In Particle Physics And Cosmology," J. Phys. Conf. Ser. **67** (2007) 012011.

[40] N. E. Mavromatos, "CPT and Decoherence in Quantum Gravity," arXiv:0707.3422 [hep-ph].

[41] D. Morgan, E. Winstanley, J. Brunner and L. F. Thompson, "Probing Lorentz invariance violation in atmospheric neutrino oscillations with a neutrino telescope," arXiv:0705.1897 [astro-ph].

[42] M. G. Burton "Antarctic Astronomy: form Infrared to Millimter Wave", paper presented at the ASP meeting in Chicago on 'Astrophysics from Antarctica', 1997, Editors G. Novak & R. H. Landsberg

[43] Gentle courtesy of `http://www.its.caltech.edu/ atomic/snowcrystals/`

[44] K. Woschnagg [AMANDA Collaboration], "Optical properties of South Pole ice at depths from 140-meters to 2300-meters," *Prepared for 26th International Cosmic Ray Conference (ICRC 99), Salt Lake City, UT, 17-25 Aug 1999.*

[45] O. Tarasova, M. Kowalski and M. Walter [IceCube Collaboration], "Search for neutrino-induced cascades with AMANDA data taken in 2000-2004," *Prepared for 30th International Cosmic Ray Conference (ICRC 2007), Merida, Yucatan, Mexico, 3-11 Jul 2007.*

[46] Peter Steffen and Peter Niessen, (AMANDA internal document) `http://internal.icecube.wisc.edu/amanda/software/sieglinde/`

[47] H. T. Janka and E. Mueller, "Neutrino heating, convection, and the mechanism of Type-II supernova explosions," Astron. Astrophys. **306** (1996) 167.

[48] A. Karle [IceCube Collaboration], "IceCube: Construction status and performance results of the 22 string detector," *Prepared for 30th International Cosmic Ray Conference (ICRC 2007), Merida, Yucatan, Mexico, 3-11 Jul 2007*

[49] A. Achterberg *et al.* [AMANDA Collaboration], "Limits On The Muon Flux From Neutralino Annihilations At The Center Of The Earth With Amanda," Astropart. Phys. **26** (2006) 129.

[50] M. Ackermann *et al.* [AMANDA Collaboration], "Limits to the muon flux from neutralino annihilations in the sun with the AMANDA detector," Astropart. Phys. **24** (2006) 459 [arXiv:astro-ph/0508518].

[51] D. K. Aitken *et al.* "The Scientific Potential for Astronomy from the Antarctic Plateau" prepared by the Australian Working Group for Antarctic Astronomy, edited by Michael Burton

[52] A. Achterberg *et al.* [IceCube Collaboration], "First year performance of the IceCube neutrino telescope," Astropart. Phys. **26** (2006) 155 [arXiv:astro-ph/0604450].

[53] Hill, G. C. Experimental and Theoretical Aspects of High Energy Astrophysics. PhD thesis, University of Adelaide, Adelaide, Australia, 1996. http://amanda.physics.wisc.edu/software/nusim/.

[54] D. Chirkin and W. Rhode, "Muon Monte Carlo: A high-precision tool for muon propagation through matter," arXiv:hep-ph/0407075.

[55] P. Miocinovic, "Muon energy reconstruction in the Antarctic Muon and Neutrino Detector Array (AMANDA),"

[56] A. Karle, "Monte Carlo simulation of photon transport and detection in deep ice: Muons and cascades," *Prepared for International Workshop on Simulations and Analysis Methods for Large Neutrino Telescopes, Zeuthen, Germany, 6-9 Jul 1998*

[57] "Evidence for insufficient absorption in the AMANDA Monte Carlo" Gary Hill, Albrecht Karle and Paolo Desiati, Kurt Woschnagg (AMANDA internal)

[58] Ackermann M., et al. (2006), Optical properties of deep glacial ice at the South Pole, J. Geophys. Res., 111, D13203,doi:10.1029/2005JD006687.

[59] S. Hundertmark, "AMASIM neutrino detector simulation program," *Prepared for International Workshop on Simulations and Analysis Methods for Large Neutrino Telescopes, Zeuthen, Germany, 6-9 Jul 1998*

[60] D. Heck, "The air shower simulation program CORSIKA," *Prepared for International Workshop on Simulations and Analysis Methods for Large Neutrino Telescopes, Zeuthen, Germany, 6-9 Jul 1998*

[61] P. Steffen, "Direct-Walk II (Improved Version of Direct Walk)", DESY Zeuthen February 12, 2002 (AMANDA Internal Report)

[62] P. Steffen, "Pattern recognition in AMANDA," *Prepared for 2nd Workshop on Methodical Aspects of Underwater/Ice Neutrino Telescopes, Hamburg, Germany, 15-16 Aug 2001*

[63] A. C. Pohl, "A statistical tool for finding non-particle events from the AMANDA neutrino telescope,"

[64] D. Pandel, "Bestimmung von Wasser- und Detektorparametern und Rekonstruktion von Myonen bis 100 TeV mit dem Bajkal-Neutrinoteleskop NT-72", Diploma Thesis, Humboldt-Universität Berlin, 1996.

[65] J. Ahrens *et al.* [AMANDA Collaboration], "Muon track reconstruction and data selection techniques in AMANDA," Nucl. Instrum. Meth. A **524** (2004) 169 [arXiv:astro-ph/0407044].

[66] M. Ribordy, "Reconstruction of composite events in neutrino telescopes," Nucl. Instrum. Meth. A **574** (2007) 137 [arXiv:astro-ph/0611604].

[67] T. Neunhoffer, "Estimating the angular resolution of tracks in neutrino telescopes based on a likelihood analysis," Astropart. Phys. **25** (2006) 220 [arXiv:astro-ph/0403367].

[68] G. C. Hill, S. Hundertmark, M. Kowlski, P. Miocinovic, T. Neunhöffer, P. Niessen, P. Steffen, O.Streicher, C.Wiebusch, "The SiEGMuND software package" (software written for the AMANDA collaboration) `http://internal.icecube.wisc.edu/amanda/software/siegmund/`

[69] T. Ullrich, Z. Xu "Treatment of Errors in Efficiency Calculations," arXiv:physics/0701199v1.

[70] T. DeYoung and G. C. Hill [AMANDA Collaboration], "Application of Bayes' theorem to muon track reconstruction in AMANDA," *Prepared for Conference on Advanced Statistical Techniques in Particle Physics, Durham, England, 18-22 Mar 2002*

[71] R. Franke, R. Lauer, E. Bernardini and M. Ackermann [IceCube Collaboration], "Point source analysis for cosmic neutrinos beyond PeV energies with AMANDA and IceCube," *Prepared for 30th International Cosmic Ray Conference (ICRC 2007), Merida, Yucatan, Mexico, 3-11 Jul 2007*

[72] J. Braun, A. Karle and T. Montaruli [IceCube Collaboration], "Neutrino point source search strategies for AMANDA-II and results from 2005," *Prepared for 30th International Cosmic Ray Conference (ICRC 2007), Merida, Yucatan, Mexico, 3-11 Jul 2007*

[73] M. Ackermann, "Searches for signals from cosmic point-like sources of high energy neutrinos in 5 years of AMANDA-II data,"

[74] J. Ahrens, *"Überprüfung der Genauigkeit der Relativitätstheorie mit atmosphärischen Myonneutrinos aus den AMANDA-daten der Jahre 2000 bis 2003"*, PhD Thesis, Universität Mainz, Mainz, Germany, 2007.

[75] A. Hocker and V. Kartvelishvili, "SVD Approach to Data Unfolding," Nucl. Instrum. Meth. A **372** (1996) 469 [arXiv:hep-ph/9509307].

[76] V. Blobel, "An unfolding method for high energy physics experiments," arXiv:hep-ex/0208022.

[77] J. Kwiecinski, A. D. Martin and A. M. Stasto, "A unified BFKL and GLAP description of F2 data," Phys. Rev. D **56** (1997) 3991 [arXiv:hep-ph/9703445].

[78] K. J. Golec-Biernat and M. Wusthoff, "Saturation in diffractive deep inelastic scattering," Phys. Rev. D **60** (1999) 114023 [arXiv:hep-ph/9903358].

[79] V. Cerny, P. Lichard and J. Pisut, "Charmed Quark Fragmentation Functions In A Monte Carlo Quark Recombination Model," Acta Phys. Polon. B **10** (1979) 779.

[80] U. Husemann [HERA-B Collaboration], "Charm and beauty production at HERA-B," AIP Conf. Proc. **792** (2005) 899 [arXiv:hep-ex/0506071].

[81] J. Abraham *et al.* [Pierre Auger Collaboration], "Correlation of the highest energy cosmic rays with nearby extragalactic objects," Science **318** (2007) 938 [arXiv:0711.2256 [astro-ph]].

[82] V. Agrawal, T. K. Gaisser, P. Lipari and T. Stanev, "Atmospheric neutrino flux above 1 GeV," Phys. Rev. D **53** (1996) 1314 [arXiv:hep-ph/9509423].

[83] G. T. Zatsepin and V. A. Kuzmin, "Upper limit of the spectrum of cosmic rays," JETP Lett. **4** (1966) 78 [Pisma Zh. Eksp. Teor. Fiz. **4** (1966) 114].

[84] G. D. Barr, T. K. Gaisser, S. Robbins and T. Stanev, "Uncertainties in atmospheric neutrino fluxes," Phys. Rev. D **74** (2006) 094009 [arXiv:astro-ph/0611266].

[85] G. Barr, T. K. Gaisser and T. Stanev, "FLUX OF ATMOSPHERIC NEUTRINOS," Phys. Rev. D **39** (1989) 3532.

[86] G. D. Barr, T. K. Gaisser, P. Lipari, S. Robbins and T. Stanev, "A three-dimensional calculation of atmospheric neutrinos," Phys. Rev. D **70** (2004) 023006 [arXiv:astro-ph/0403630].

[87] M. Honda, T. Kajita, K. Kasahara and S. Midorikawa, "Calculation of the flux of atmospheric neutrinos," Phys. Rev. D **52** (1995) 4985 [arXiv:hep-ph/9503439].

[88] U.S Standard Atmosphere, 1976, U.S Government Printing Office, Washington, D.C., 1976.

[89] Atmospheric models provided by NASA repositoy at
`http://modelweb.gsfc.nasa.gov/atmos/atmos_index.html`

[90] G. Battistoni, A. Ferrari, T. Montaruli and P. R. Sala, "The FLUKA atmospheric neutrino flux calculation," Astropart. Phys. **19** (2003) 269 [Erratum-ibid. **19** (2003) 291] [arXiv:hep-ph/0207035].

[91] G. Battistoni, A. Ferrari, P. Lipari, T. Montaruli, P. R. Sala and T. Rancati, "A 3-dimensional calculation of atmospheric neutrino flux," Astropart. Phys. **12** (2000) 315 [arXiv:hep-ph/9907408].

[92] P. Lipari, T. Stanev and T. K. Gaisser, "Geomagnetic effects on atmospheric neutrinos," Phys. Rev. D **58** (1998) 073003 [arXiv:astro-ph/9803093].

[93] T. S. Sinegovskaya and S. I. Sinegovsky, "Prompt muon contribution to the flux underwater," Phys. Rev. D **63** (2001) 096004 [arXiv:hep-ph/0007234].

[94] A. Misaki, T. S. Sinegovskaya, S. I. Sinegovsky and N. Takahashi, "Atmospheric muon fluxes underwater as a tool to probe the small-x gluon distribution," arXiv:hep-ph/0106051.

[95] E. V. Bugaev, A. Misaki, V. A. Naumov, T. S. Sinegovskaya, S. I. Sinegovsky and N. Takahashi, "Atmospheric muon flux at sea level, underground and underwater," Phys. Rev. D **58** (1998) 054001 [arXiv:hep-ph/9803488].

[96] G. Fiorentini, V. A. Naumov and F. L. Villante, "Atmospheric neutrino flux supported by recent muon experiments," Phys. Lett. B **510** (2001) 173 [arXiv:hep-ph/0103322].

[97] B. Wiebel-Sooth, P. L. Biermann and H. Meyer, "Cosmic Rays VII. Individual element spectra: prediction and data," arXiv:astro-ph/9709253.

[98] E. V. Bugaev and V. A. Naumov, "ON THE INTERPRETATION OF THE KAMIOKANDE NEUTRINO EXPERIMENT," Phys. Lett. B **232** (1989) 391.

[99] G. 't Hooft, "A Two-Dimensional Model For Mesons," Nucl. Phys. B **75** (1974) 461.

[100] A. B. Kaidalov and O. I. Piskunova, "PRODUCTION OF CHARMED PARTICLES IN THE QUARK - GLUON STRING MODEL," Sov. J. Nucl. Phys. **43** (1986) 994 [Yad. Fiz. **43** (1986) 1545].

[101] L. Pasquali, M. H. Reno and I. Sarcevic, "Neutrinos and muons from atmospheric charm," arXiv:hep-ph/9905389.

[102]

[102] P. Nason, M. Mangano and G. Ridolfi, "New theoretical results in heavy quark hadroproduction," Nucl. Phys. Proc. Suppl. **27** (1992) 29.

[103] T. Wibig, "High-energy interactions around the 'knee'," J. Phys. G **27** (2001) 1633.

[104] A. B. Kaidalov, "High-energy hadronic interactions (20 years of the quark gluon strings model)," Phys. Atom. Nucl. **66** (2003) 1994.

[105] N. S. Amelin, E. F. Staubo, L. P. Csernai, V. D. Toneev, K. K. Gudima and D. Strottman, "Transverse flow and collectivity in ultrarelativistic heavy ion collisions," Phys. Rev. Lett. **67** (1991) 1523.

[106] D. Decamp *et al.* [ALEPH Collaboration], "A PRECISE DETERMINATION OF THE NUMBER OF FAMILIES WITH LIGHT NEUTRINOS AND OF THE Z BOSON PARTIAL WIDTHS," Phys. Lett. B **235** (1990) 399.

[107] J. Breitweg *et al.* [ZEUS Collaboration], "Measurement of the proton structure function F2 at very low Q**2 at HERA," Phys. Lett. B **487** (2000) 53 [arXiv:hep-ex/0005018].

[108] E. L. Berger, M. M. Block, D. W. McKay and C. I. Tan, "Ultra-high energy neutrino scattering on an isoscalar nucleon," arXiv:0708.1960 [hep-ph].

[109] A. Cooper-Sarkar and S. Sarkar, "Predictions for high energy neutrino cross-sections from the ZEUS global PDF fits," JHEP **0801** (2008) 075 [arXiv:0710.5303 [hep-ph]].

[110] G. Gelmini, P. Gondolo and G. Varieschi, "Prompt atmospheric neutrinos and muons: Dependence on the gluon distribution function," Phys. Rev. D **61** (2000) 056011 [arXiv:hep-ph/9905377].

[111] "Cosmic Rays and Particle Physics" by Thomas K. Gaisser, Cambridge University Press, 1991

[112] W.-M.Yao et al. (Particle Data Group), J. Phys. G 33, 1 (2006) and 2007 partial update for the 2008 edition

[113] "International Geomagnetic Reference Field" information available at `http://swdcwww.kugi.kyoto-u.ac.jp/index.html`

[114] C. G. S. Costa, "The prompt lepton cookbook," Astropart. Phys. **16** (2001) 193 [arXiv:hep-ph/0010306].

[115] T. Montaruli, C. Lewis, J. C. Diaz-Velez, A. Tamburro "The NeutrinoFlux C++ class: a service for fluxes for weighting" http://www.icecube.wisc.edu/tmontaruli/neutrinoflux/

[116] G. C. Hill and K. Rawlins, "Unbiased cut selection for optimal upper limits in neutrino detectors: The model rejection potential technique," Astropart. Phys. **19**, 393 (2003) [arXiv:astro-ph/0209350].

[117] M. P. Kowalski, "Search for neutrino induced cascades with the AMANDA-II detector,"

[118] J. W. Cronin, S. P. Swordy and T. K. Gaisser, "Cosmic rays at the energy frontier," Sci. Am. **276** (1997) 32.

[119] M. Cacciari, M. Greco, S. Rolli and A. Tanzini, "Charmed mesons fragmentation functions," Phys. Rev. D **55** (1997) 2736 [arXiv:hep-ph/9608213].